Karlsruhe Institute of Technology

Automated NLO Calculations with Massive Quarks in Herwig++

Automatisierte NLO-Rechnungen mit massiven Quarks in Herwig++

Master Thesis

by

Daniel Rauch

at the
Department of Physics
Institute for Theoretical Physics

Reviewer:	PD Dr. Stefan Gieseke
Second reviewer:	Prof. Dr. Ulrich Husemann
External advisor:	Dr. Simon Plätzer (IPPP, Durham)

Duration: 12th December 2013 – 12th December 2014

Ich versichere, dass ich diese Arbeit selbstständig verfasst und keine anderen als die angegebenen Hilfsmittel verwendet habe.

Daniel Rauch
Karlsruhe, den 12. Dezember 2014

Als Masterarbeit anerkannt.

PD Dr. Stefan Gieseke
Karlsruhe, den 12. Dezember 2014

Acknowledgment

First of all I would like to thank my advisor Dr. Stefan Gieseke who offered me the opportunity to work on the very interesting topics of this thesis. I am very grateful for his guidance during this work as well as his support in every respect.

Many thanks also go to Prof. Dr. Ulrich Husemann who kindly agreed to be the second reviewer.

It has been a pleasure for me to participate in the development of Herwig++. Most notably I would like to thank the Karlsruhe section consisting of Johannes Bellm, Dr. Stefan Gieseke, Dr. Frasher Loshaj and Dr. Christian Reuschle as well as the former group members Nadine Fischer and Dr. Christian Röhr. A very special thanks goes to Dr. Simon Plätzer from IPPP, Durham who always found the time to discuss the many questions I had.

This thesis would not have been possible without access to high-performance computing resources. Therefore I would first and foremost like to express my gratitude to the ITP admins Johannes Bellm and Robin Roth for their help and their continuous efforts to keep the ITP computing infrastructure up and running. Parts of this work was performed on the computational resource bwUniCluster funded by the Ministry of Science, Research and Arts and the Universities of the State of Baden-Württemberg, Germany, within the framework program bwHPC. I am particularly grateful to Dr. Robert Barthel and Hartmut Häfner of the Steinbuch Centre for Computing (SCC) for their support.

I very much enjoyed the year it took to complete this thesis. Apart from the topic itself this is also due to the very good atmosphere at the institute for which I would like to thank my present and former office colleagues Nadine Fischer, Agilo Kern, Carla Krauss, Max Löschner, Robin Lorenz, Robin Roth and Alexander Wlotzka as well as all other members of the ITP.

Furthermore, I am very grateful to Johannes Bellm, Robin Lorenz, Dr. Christian Reuschle and Robin Roth who were kind enough to proofread drafts of this thesis.

Finally, I owe my deepest gratitude to my family who gave me the opportunity of pursuing my studies and supported me in all these years and to Shahrzad for her calm and reassuring support, love and patience.

Contents

Chapter 1

Introduction

Processes involving top quarks are interesting and important in many different ways. The top quark is the heaviest particle in the standard model and therefore has the largest coupling to the Higgs boson which makes it important for many studies of the Higgs and its properties. Top quarks and associated jets also play a prominent role in the backgrounds of Higgs analyses and searches for new physics. For these reasons it is desirable to have at one's disposal precise calculations for processes involving top quarks.

Monte Carlo simulations play a very important role in high energy particle physics. They provide the means to generate theoretical predictions that can be compared to experimental data and thus allow us to test our understanding of the fundamental particles and their interactions. The increasing availability of programs for the generation of next-to-leading order (NLO) matrix elements has led to many activities and efforts in recent years in the context of Monte Carlo event generators. The two most important aspects in this regard are the automation of NLO calculations and the combination of NLO matrix elements and parton showers. Both topics are studied in this thesis.

The automation of calculations at next-to-leading order in quantum chromodynamics (QCD) requires the treatment of infrared (IR) singularities that manifest themselves in the virtual and real-emission contributions to the cross section and cancel against each other order by order in perturbation theory. In analytical calculations this cancellation can be achieved and seen directly when regularization techniques such as dimensional regularization are used. However, it is not possible to carry out numerical calculations as e.g. Monte Carlo simulations at NLO without further efforts for the treatment of these divergences. To overcome these difficulties several methods were conceived which allow for a process-independent regularization of the IR singularities in numerical calculations. One of them is the subtraction algorithm by Catani and Seymour which was first given for the case of massless partons [1, 2] and later extended to also cover massive partons.

The Catani-Seymour algorithm for the subtraction of infrared singularities is used in the general-purpose event generator Herwig++ for the automated calculation of NLO QCD corrections for processes with massless partons. A preliminary implementation of the

algorithm for massive partons was done by Martin Stoll [3] and validated for the process $e^+e^- \to b\bar{b}$. This case, however, only includes a certain subset of all terms that are part of the full algorithm. The goal of this thesis therefore is to put the implementation for the case of massive partons in hadron-hadron collisions into operation for the first time in Herwig++, expand it to also cover top quarks and validate it. In contrast to the case of lepton-lepton collisions, the application to quark pair production in hadron-hadron collisions involves almost all terms of the algorithm and therefore provides the first extensive validation of the implementation. The extension and validation done in the course of this thesis for the first time encompasses processes with massive partons that occur at the Large Hadron Collider (LHC) which will presumably be restarted at an increased center-of-mass energy of 13 TeV in spring 2015.

While fixed-order calculations are suited to provide predictions for inclusive and infrared-safe quantities such as total inclusive cross sections and certain differential observables that probe well-separated final states it is necessary to advance to all-order resummations if more exclusive quantities and regions close to the IR limits are to be described. In general-purpose Monte Carlo programs exclusive events are generated using parton showers on top of the hard process generation based on matrix elements. Given this complementary nature of both approaches increased efforts have been made in the last decade to combine parton showers with the increased accuracy of NLO matrix elements. These activities can be divided into two principal classes: The combination of NLO matrix elements for a single process with parton showers is called *matching* whereas in *merging* matrix elements for different particle multiplicities are combined and a parton shower is added on top. The principal goal of the methods developed in this context is to avoid *double-counting* of contributions. In the case of matched calculations this double-counting occurs between the real-emission matrix elements and the parton shower acting on the Born contribution.

Having at hand an algorithm for the subtraction of IR singularities for massive partons in fixed-order NLO calculations, in a second part of this thesis the existing matching of the angular-ordered parton shower in Herwig++ is validated for the process $pp \to t\bar{t}$.

Numerical calculations at NLO and the use of parton showers increase the computing time necessary to achieve a desired level of statistical uncertainty. This makes the use of single Monte Carlo runs tedious or even utterly impractical. To overcome this limitation, multiple independent Monte Carlo jobs can be run in parallel on computing clusters. In this thesis, formulas for the stable combination of total and differential cross sections from a number of arbitrarily-composed Monte Carlo jobs are derived and implemented into a new tool called Herwig-Parallel that serves to organize and control the event generation and the subsequent combination of the results. Given access to suitable computing resources, this allows for the generation of significant amounts of statistics in acceptable time scales and if necessary a scaling of the computational efforts for increasingly complex calculations.

Chapter 2 of this thesis deals with fixed-order calculations. After a review of the general structure of NLO calculations the idea behind the subtraction methods for the treatment of IR singularities is presented. Thereafter, the Catani-Seymour algorithms for the case of massless as well as massive partons are discussed. In chapter 3 the approximation that underlies parton showers and the construction of a parton shower algorithm are outlined. This is followed by an introduction into the matching of NLO cross sections and parton showers. The Monte Carlo method is reviewed in chapter 4 where at first the Monte Carlo integration for the calculation of total and differential cross sections is treated. Subsequently, formulas for the combination of parallel Monte Carlo runs are derived. In chapter 5 after some general remarks about general-purpose event generators the tools and

programs used in this thesis are described. The implementation of the Catani-Seymour algorithm in Herwig++ is treated in chapter 6. The validation results for the combination of multiple Monte Carlo runs and both the fixed-order calculation as well as the matching to the angular-order qtilde shower are presented in chapter 7. Finally, in chapter 8 the results of this work are summarized and an outlook is given.

Chapter 2

Fixed-Order NLO QCD Calculations

On many occasions leading order (LO) calculations are not sufficient for quantitative predictions in quantum chromodynamics (QCD) due to large K-factors or shapes of distributions being modified by higher-order corrections. Also, the theoretical uncertainties, which can be estimated from scale variations, are typically rather large. For these reasons it is desirable to advance to next-to-leading order (NLO) accuracy. In section 2.1 of this chapter the general structure of NLO QCD calculations at fixed order in perturbation theory is reviewed. The subtraction framework for the treatment of infrared (IR) divergences is introduced in section 2.2. Section 2.3 deals with hadron-hadron collisions and finally, the Catani-Seymour subtraction algorithms for massless and massive partons are presented in section 2.4. For an introduction or review of the fundamentals and phenomenological properties of QCD the reader is referred to [4] and other textbooks. Likewise, the details and technicalities of renormalization are not the focus of this thesis but can be looked up in a number of reviews and books such as e.g. [5, 6].

2.1. NLO Cross Sections in QCD

Suppressing for a moment additional sums and factors that arise if hadrons are involved in the collisions, the total inclusive cross section for producing a certain final state F to all orders in perturbation theory is given by

$$\sigma = \sum_{k=0}^{\infty} \int_{m+k} \mathrm{d}\Phi_{m+k} \left| \sum_{l=0}^{\infty} \mathcal{M}^{(l)}_{m+k}(\Phi_{m+k}) \right|^2 \tag{2.1}$$

with

$$\mathrm{d}\Phi_{m+k} = \mathcal{SF} \prod_{f=0}^{m+k} \frac{\mathrm{d}^3\vec{p}_f}{(2\pi)^3} \frac{1}{2E_f} \ , \tag{2.2}$$

where

- m describes the number of particles in the final state F,
- k denotes the number of additional real emissions,
- l is the number of loops,
- $\mathcal{S}$ describes the symmetry factor that appears for groups of identical final-state particles
- $\mathcal{F}$ represents the flux factor and
- $\mathcal{M}^{(l)}_{m+k} = \mathcal{M}^{(l)}_{m+k}(\Phi_{m+k})$ is the scattering amplitude corresponding to the sum of the Feynman diagrams with l loops and $m+k$ final-state particles.

Note that the inclusive cross section describes the production of the final state F+*anything*, i.e. all further possible real emissions are unresolved.

The prediction for an observable O is given by

$$O = \sum_{k=0}^{\infty} \int_{m+k} \mathrm{d}\Phi_{m+k} \left| \sum_{l=0}^{\infty} \mathcal{M}^{(l)}_{m+k} \right|^2 O(\Phi_{m+k}) \ . \tag{2.3}$$

If this observable O is chosen to be the differential distribution of some quantity o a δ-distribution is inserted which inhibits the integration over that slice of the phase space that corresponds to a certain value of this quantity, i.e. $O(\Phi_{m+k}) = \delta(o - o(\Phi_{m+k}))$ and thus

$$O = \frac{\mathrm{d}\sigma}{\mathrm{d}o} = \sum_{k=0}^{\infty} \int_{m+k} \mathrm{d}\Phi_{m+k} \left| \sum_{l=0}^{\infty} \mathcal{M}^{(l)}_{m+k} \right|^2 \delta(o - o(\Phi_{m+k})) \ . \tag{2.4}$$

This general formulation is chosen in order to accommodate the application of e.g. cuts or jet algorithms in the same notation later on.

Encoded in equations 2.1 and 2.3 is the structure of perturbation theory, in which observables are calculated as a power series in the coupling constant, in the hope that truncating it at a certain order will approximate the exact solution. In the case of QCD, this coupling constant is denoted by α_s. The lowest possible order in this expansion that is capable of producing the desired final state F is called *Born-level* or *leading order* contribution and hereafter symbolically written as α_s^F. The next higher order α_s^{F+1} in the perturbation expansion is consequently called *next-to-leading order* (NLO). Writing explicitly the terms with no more than one additional loop or leg in 2.1 gives

$$\sigma = \int_m \mathrm{d}\Phi_m \left| \mathcal{M}^{(0)}_{m+0} + \mathcal{M}^{(1)}_{m+0} + \ldots \right|^2 + \int_{m+1} \mathrm{d}\Phi_{m+1} \left| \mathcal{M}^{(0)}_{m+1} + \ldots \right|^2 + \ldots \tag{2.5}$$

where the dots indicate higher orders. It is important to recall that on the level of the scattering amplitudes one additional real emission gives another vertex factor proportional to $g_s \propto \sqrt{\alpha_s}$ while an additional loop results in a factor proportional to $g_s^2 \propto \alpha_s$ with α_s and g_s being related as usually by

$$\alpha_s = \frac{g_s^2}{4\pi} \ . \tag{2.6}$$

Therefore, the terms given explicitly in equation 2.5 are more than sufficient for NLO accuracy. Rewriting this expansion yields

$$\sigma = \int_m \mathrm{d}\Phi_m \Bigg(\underbrace{\left| \mathcal{M}^{(0)}_{m+0} \right|^2}_{\mathcal{O}(\alpha_s^F)} + 2\,\mathrm{Re}\, \Big(\underbrace{\mathcal{M}^{(0)}_{m+0}{}^{\dagger} \mathcal{M}^{(1)}_{m+0}}_{\mathcal{O}(\alpha_s^{F+1})} \Big) \Bigg) + \int_{m+1} \mathrm{d}\Phi_{m+1} \underbrace{\left| \mathcal{M}^{(0)}_{m+1} \right|^2}_{\mathcal{O}(\alpha_s^{F+1})} + \mathcal{O}\left(\alpha_s^{F+2}\right) \ . \tag{2.7}$$

In a condensed notation the fixed-order NLO cross section can be written as

$$\sigma_{\mathrm{NLO}} = \int_m \mathrm{d}\sigma_B + \int_m \mathrm{d}\sigma_V + \int_{m+1} \mathrm{d}\sigma_R \tag{2.8}$$

with

- the Born contribution

$$\mathrm{d}\sigma_B = \mathcal{B}\left(\Phi_m\right) \mathrm{d}\Phi_m = \left|\mathcal{M}^{(0)}_{m+0}\right|^2 \mathrm{d}\Phi_m \ , \tag{2.9}$$

- and the virtual contribution

$$\mathrm{d}\sigma_V = \mathcal{V}\left(\Phi_m\right) \mathrm{d}\Phi_m = 2 \ \mathrm{Re}\left(\mathcal{M}^{(0)\ \dagger}_{m+0} \mathcal{M}^{(1)}_{m+0}\right) \mathrm{d}\Phi_m \tag{2.10}$$

- the real-emission contribution

$$\mathrm{d}\sigma_R = \mathcal{R}\left(\Phi_{m+1}\right) \mathrm{d}\Phi_{m+1} = \left|\mathcal{M}^{(0)}_{m+1}\right|^2 \mathrm{d}\Phi_{m+1} \ . \tag{2.11}$$

While the Born cross section $\int_m \mathrm{d}\sigma_B$ is finite - either by itself or by virtue of cuts imposed on the final state, e.g. in order to enforce isolation of particles - and can in principle be integrated in a straight-forward manner either numerically or at least in some cases analytically, the real-emission and virtual contributions require additional treatment.

The virtual contribution to the NLO cross section contains *ultra-violet* (UV) divergences stemming from integrations over upwardly unbounded loop momenta. These divergences can be parametrized using different *regularization schemes*. Commonly used nowadays are different versions of *dimensional regularization* which are gauge- and Lorentz-invariant and where the integration is carried out in $d = 4-2\epsilon$ dimensions. Afterwards, the parametrized singularities which in dimensional regularization manifest themselves as poles in $1/\epsilon$ can be absorbed into physically meaningful redefinitions of the parameters that appear in the Lagrangian. This procedure is known as *renormalization*. It results in UV-finite cross sections but has the additional effect that initially constant parameters become dependent on certain kinematic scales that have to be introduced when applying the *renormalization conditions*. The latter encode the imposition of experimentally measured or otherwise motivated values for the parameters at specific kinematic points. Possibly the most prominent examples for this phenomenon are the *running couplings* of the electromagnetic or the strong forces that depend on the energy scale of the interactions.

After getting rid of these UV divergences, the virtual as well as the real-emission contributions still exhibit another class of singularities, the *infrared* (IR) divergences which arise from propagators going on-shell if the attached outgoing particles are collinear or soft. However, experimentally measured cross sections are always finite and indeed the KLN theorem found by Kinoshita, Lee and Nauenberg [7, 8] guarantees that the IR divergences from the virtual and the real-emission parts of the cross section cancel against each other for each order in perturbation theory if sufficiently inclusive and infrared-safe observables are considered. A formal definition of infrared safety will be given later on but it basically means that the observable does not depend on the actual number of additional soft and collinear partons that are created.

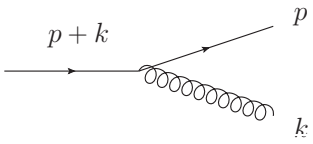

Figure 2.1.: Diagram for the emission of a gluon with momentum k by a quark with momentum $p + k$.

In order to motivate the appearance of infrared divergences consider the emission of a gluon off a quark with mass m as depicted in figure 2.1. The quark propagator before the splitting is given by

$$\frac{\not{p} + \not{k} + m}{(p+k)^2 - m^2} \tag{2.12}$$

which when imposing on-shell conditions $p^2 = m^2$ and $k^2 = 0$ on the outgoing quark and gluon simplifies to

$$\frac{\not{p} + \not{k} + m}{2E_k \left(E_p - |\vec{p}| \cos\theta\right)} \ , \tag{2.13}$$

where θ denotes the angle between the quark after the splitting and the gluon. From this form it can be seen that a singularity arises if the emitted gluon becomes soft, i.e. $E_k \to 0$. If the quark is massless the propagator reads

$$\frac{\not{p} + \not{k}}{2E_k E_p \left(1 - \cos\theta\right)} \tag{2.14}$$

and the additional singularities for a soft quark and for a collinear configuration of the quark and the gluon becomes visible. But also for a massive quark the propagator can become large resulting in an enhanced cross section.

In QCD the singularities and enhancements arising from the kinematics are amplified by the running of the coupling constant $\alpha_s(Q^2)$ which increases towards smaller scales Q^2. As a result of both effects, the final-state particles produced in QCD processes are always accompanied by additional, mainly soft and collinear quarks and gluons that form *jets*. This of course raises the question how this can be treated in theoretical calculations. While one part of the answer lies in the introduction of parton showers which are described in the next chapter there is also something that can be done in the context of fixed-order calculations. The key point lies in the *inclusive* character of the cross sections described in this chapter which means that only the hard process as encoded in the considered Feynman diagrams is specified. No further splittings or emissions are considered, so any or none of them may occur - with the sum of all possibilities giving unity in total.

No physical device can resolve arbitrarily soft or collinear particles. Yet it is exactly these kinematically degenerate configurations that give rise to the aforementioned singularities and enhancements. Thus, in calculations of jet observables it is necessary to specify some sort of resolution criterion that determines which partons are resolved and which ones are not. Thereby it is ensured that the corresponding cross sections are well-defined even in the presence of an arbitrary number of soft and/or collinear splittings. This behavior of observables is called *infrared safety*. In mathematical notation this can be expressed by means of *jet functions* $F_J^{(m)}(p_1, \ldots, p_m)$ that can be included in the observable O and satisfy

$$F_J^{(m+1)}(\ldots, p_i, \ldots, p_{j-1}, p_j, p_{j+1}, \ldots) \to F_J^{(m)}(\ldots, p_i, \ldots, p_{j-1}, p_{j+1}, \ldots) \tag{2.15}$$

if the parton j becomes soft and

$$F_J^{(m+1)}(p_1,\ldots,p_i,\ldots,p_j,\ldots,p_{m+1}) \to F_J^{(m)}(p_1,\ldots,p_{ij},\ldots,p_{m+1}) \tag{2.16}$$

if partons i and j become collinear with $p_{ij} = p_i + p_j$. Thus, the fixed-order NLO cross section is given by

$$\begin{aligned}\sigma_{\mathrm{NLO}} &= \int_m \left[\mathcal{B}(\Phi_m) + \mathcal{V}(\Phi_m)\right] F_J^{(m)}(\Phi_m)\mathrm{d}\Phi_m \\ &+ \int_{m+1} \mathcal{R}(\Phi_{m+1}) F_J^{(m+1)}(\Phi_{m+1})\mathrm{d}\Phi_{m+1}\ ,\end{aligned} \tag{2.17}$$

where the above definition of infrared safety ensures the finiteness of the total cross section. In numerical calculations or experimental analyses the role of the jet functions is played by jet clustering algorithms such as the kt, anti-kt or Cambridge/Aachen algorithms which are commonly used nowadays (see section 2.2 of [9]).

2.2. The Subtraction Method for the Calculation of Jet Cross Sections

Even though the singularities from the real-emission and the virtual contributions to the cross section cancel against each other order by order in perturbation theory this way of computing the cross section is not suited for implementation in numerical programs. This is due to the fact that both contributions are separately divergent and reside in different phase spaces that have to be integrated independently of each other. Thus, a prescription for the numerical regularization of the IR divergences is needed. But even with finite values special attention has to be paid to the stability of the algorithm since the subtraction of numbers that are much larger than the typical values for the respective calculations can result in instabilities and thus introduce convergence problems. There are two main classes of procedures for the regularization of IR singularities, the *phase space slicing* method and the *subtraction* method, the principles and differences of which are sketched in [10]. In this section the general idea behind the subtraction methods will be presented.

As already suggested by the name, the different versions of the subtraction method subtract an auxiliary cross section $\mathrm{d}\sigma_A = \mathcal{A}\left(\Phi_{m+1}\right)\mathrm{d}\Phi_{m+1}$ from the real-emission contribution for each phase space point and add it back again to the virtual contribution in order to preserve the total cross section.

$$\begin{aligned}\sigma_{\mathrm{NLO}} &= \int_m \mathcal{B}\left(\Phi_m\right) F_J^{(m)}(\Phi_m)\mathrm{d}\Phi_m \\ &+ \int_{m+1} \mathcal{R}\left(\Phi_{m+1}\right) F_J^{(m+1)}(\Phi_{m+1})\mathrm{d}\Phi_{m+1} - \int_{m+1} \mathcal{A}\left(\Phi_{m+1}\right) F_J^{(m)}(\Phi_m)\mathrm{d}\Phi_{m+1} \\ &+ \int_m \mathcal{V}\left(\Phi_m\right) F_J^{(m)}(\Phi_m)\mathrm{d}\Phi_m + \int_{m+1} \mathcal{A}\left(\Phi_{m+1}\right) F_J^{(m)}(\Phi_m)\mathrm{d}\Phi_{m+1}\end{aligned} \tag{2.18}$$

The auxiliary cross section $\mathrm{d}\sigma_A$ is constructed in such a way that it has the same infrared-singular behavior as the real-emission contribution. Since the singularities and enhancements that are to be controlled occur exactly in the phase space region where - thanks to their infrared safety - the jet functions $F_J^{(m+1)}$ and $F_J^{(m)}$ coincide, the pointwise cancellation between the real-emission part and the auxiliary cross section is not impaired

and the second line of equation (2.18) is finite by construction and can be integrated in a numerically stable way in $d = 4$ dimensions. The finiteness of the third line in equation (2.18) is guaranteed by the KLN theorem. When dimensional regularization is used in the virtual part of the cross section the IR singularities are exposed as poles in $1/\epsilon$ and $1/\epsilon^2$. Given a factorized phase space $\mathrm{d}\Phi_{m+1} = \mathrm{d}\Phi_m \mathrm{d}\Phi_{\mathrm{add}}$, the auxiliary cross section can be integrated over the one-particle emission phase space, thus reproducing and canceling the poles from the virtual contribution, i.e.

$$\begin{aligned}
\sigma_{\mathrm{NLO}} &= \int_m \mathcal{B}\left(\Phi_m\right) F_J^{(m)}(\Phi_m)\mathrm{d}\Phi_m \\
&+ \int_{m+1} \left[\mathcal{R}\left(\Phi_{m+1}\right)_{\epsilon=0} F_J^{(m+1)}(\Phi_{m+1}) - \mathcal{A}\left(\Phi_{m+1}\right)_{\epsilon=0} F_J^{(m)}(\Phi_m)\right] \mathrm{d}\Phi_{m+1} \\
&+ \int_m \left[\mathcal{V}\left(\Phi_m\right) + \int_1 \mathcal{A}\left(\Phi_{m+1}\right) \mathrm{d}\Phi_{\mathrm{add}}\right]_{\epsilon=0} F_J^{(m)}(\Phi_m)\mathrm{d}\Phi_m
\end{aligned} \tag{2.19}$$

Note that the integral over the additional one-particle phase space, denoted here symbolically by $\int_1 d\Phi_{\mathrm{add}}$ has to be carried out in d dimensions leading to the ϵ-poles and the desired cancellation. With a completely factorized auxiliary term it would be possible to do this integral once and for all analytically and leave the remaining Born phase space integration to the Monte Carlo event generator. Indeed, such a prescription for constructing the subtraction terms was found by Catani and Seymour, first for massless partons [1, 2] and later also for massive partons [11]. More specifically, the auxiliary cross section is formulated as

$$\mathcal{A}\left(\Phi_{m+1}\right) \mathrm{d}\Phi_{m+1} = \sum_{\mathrm{dipoles}} \mathcal{B}(\tilde{\Phi}_m(\Phi_{m+1})) \otimes V_{\mathrm{dipole}}\left(\Phi_{m+1}\right) \mathrm{d}\Phi_{m+1} \tag{2.20}$$

where $\mathcal{B}(\tilde{\Phi}_m(\Phi_{m+1}))$ denotes the Born cross section evaluated at a phase space point obtained by projecting the $m+1$-particle phase space configuration onto a corresponding m-particle configuration and V_{dipole} represents some universal, i.e. process-independent factors that only depend on the kinematics of the splitting leading to the real emission. $\otimes$ denotes spin and color correlations between all particles. Given a parametrization of the splitting kinematics that provides the desired phase space factorization

$$\mathrm{d}\Phi_{m+1} = \mathrm{d}\tilde{\Phi}_m(\Phi_{m+1})\mathrm{d}\Phi_{\mathrm{add}}(\Phi_{m+1}) \tag{2.21}$$

this can be rewritten as

$$\mathcal{A}\left(\Phi_{m+1}\right) \mathrm{d}\Phi_{m+1} = \mathcal{B}(\tilde{\Phi}_m)\mathrm{d}\tilde{\Phi}_m \otimes \sum_{\mathrm{dipoles}} V_{\mathrm{dipole}}\left(\Phi_{\mathrm{add}}\right) \mathrm{d}\Phi_{\mathrm{add}} \ . \tag{2.22}$$

By defining the *insertion operator*

$$\boldsymbol{I} = \sum_{\mathrm{dipoles}} \int_1 V_{\mathrm{dipole}}\left(\Phi_{\mathrm{add}}\right) d\Phi_{\mathrm{add}} \tag{2.23}$$

the total NLO cross section can now be written as

$$\begin{aligned}
\sigma_{\mathrm{NLO}} &= \int_m \mathcal{B}\left(\Phi_m\right) F_J^{(m)}(\Phi_m)\mathrm{d}\Phi_m \\
&+ \int_{m+1} \left[\mathcal{R}\left(\Phi_{m+1}\right)_{\epsilon=0} F_J^{(m+1)}(\Phi_m) - \mathcal{A}\left(\Phi_{m+1}\right)_{\epsilon=0} F_J^{(m)}(\Phi_m)\right] \mathrm{d}\Phi_{m+1} \\
&+ \int_m \left[\mathcal{V}\left(\Phi_m\right) + \mathcal{B}\left(\Phi_m\right) \otimes \boldsymbol{I}\right]_{\epsilon=0} F_J^{(m)}(\Phi_m)\mathrm{d}\Phi_m \ .
\end{aligned} \tag{2.24}$$

2.3. NLO QCD Cross Sections for Hadron Collisions

At leading order the cross section for the collision of a hadron A with momentum P_A and a hadron B with momentum P_B is given by the expression

$$\sigma_{\mathrm{LO}} = \sum_{a,b} \int_0^1 \mathrm{d}\eta_a \int_0^1 \mathrm{d}\eta_b \; f_{a/A}^{(\mathrm{LO})}(\eta_a, \mu_F^2) f_{b/B}^{(\mathrm{LO})}(\eta_b, \mu_F^2) \; \sigma_{ab}^{(\mathrm{LO})}(p_a, p_b) \tag{2.25}$$

where $f_{i/I}^{(\mathrm{LO})}(\eta, \mu_F)$ denotes the leading order *parton distribution function* (*pdf*) for the parton i with a momentum fraction η_i at a factorization scale μ_F. At leading order this can be interpreted as the probability density for extracting the parton i from the hadron I with the given momentum fraction η_i. $\sigma_{ab}^{(\mathrm{LO})}$ represents the parton-level cross section with the incoming parton momenta $p_a = \eta_a P_A$ and $p_b = \eta_b P_B$. For a detailed review of the factorization theorems that allow for this separation of the hard interaction and the low energy behavior as encoded by the pdfs the reader is referred to [12].

A few more comments are necessary regarding the treatment of identified hadrons at next-to-leading order. This comprises hadrons involved in the initial state as is the case for lepton-hadron or hadron-hadron collisions as well as observables depending on hadronic final-state momenta. The latter implies the use of *fragmentation functions* which specify the probability for an outgoing parton with a certain momentum to produce a hadron of the desired type and momentum. However, in the context of Monte Carlo event generators this role can be played by showers and subsequent hadronization models that produce all possible hadronic final states. This procedure averts the special treatment of identified final-state partons and thus, only the first case with initial-state partons is relevant in this context.

Once initial-state partons that are extracted from incoming hadrons are involved additional divergences arise in the real-emission contribution $\int_{m+1} \mathrm{d}\sigma_R$ to the NLO cross section that are not canceled any more by the virtual contributions $\int_m \mathrm{d}\sigma_V$ [2]. This is due to the fact that the contributions corresponding to infrared initial-state configurations are absorbed into the evolution of the parton distribution functions if they are below the factorization scale. In order to retain the cancellation of all singularities as guaranteed by the KLN theorem, the *collinear counterterm* $\mathrm{d}\sigma_C$ has to be added. Thus, the NLO cross section for hadron-hadron collisions is given by the expression

$$\begin{aligned} \sigma_{\mathrm{NLO}} = \sum_{a,b} \int_0^1 \mathrm{d}\eta_a \int_0^1 \mathrm{d}\eta_b \; f_{a/A}^{(\mathrm{NLO})}(\eta_a, \mu_F^2) f_{b/B}^{(\mathrm{NLO})}(\eta_b, \mu_F^2) \\ \times \left[\int_m \mathrm{d}\sigma_{ab}^B(p_a, p_b) + \int_m \mathrm{d}\sigma_{ab}^V(p_a, p_b) + \int_{m+1} \mathrm{d}\sigma_{ab}^R(p_a, p_b) + \int_m \mathrm{d}\sigma_{ab}^C(p_a, p_b, \mu_F) \right] \end{aligned} \tag{2.26}$$

The collinear counterterm takes the form

$$\mathrm{d}\sigma_C(p) = \int_0^1 \mathrm{d}x \Gamma(x) \mathrm{d}\sigma_B(xp) \tag{2.27}$$

for the case of lepton-hadron collisions and

$$\mathrm{d}\sigma_C(p_a, p_b) = \int_0^1 \mathrm{d}x_a \Gamma(x_a) \mathrm{d}\sigma_B(x_a p_a, p_b) + \int_0^1 \mathrm{d}x_b \Gamma(x_b) \mathrm{d}\sigma_B(p_a, x_b p_b) \tag{2.28}$$

in the case of two incoming hadrons. The function $\Gamma(x)$ was only written symbolically to describe the structure of the collinear counterterm for the cases of one and two colliding

hadrons and therefore is not given explicitly. In either case the collinear counterterm is singular in the limit $\epsilon \to 0$ and cancels the remaining divergences such that

$$\int_m \mathrm{d}\sigma_V + \int_{m+1} \mathrm{d}\sigma_R + \int_m \mathrm{d}\sigma_C \tag{2.29}$$

is finite. Due to the analytical cancellation of singularities this formulation is not suited for implementation in a Monte Carlo program so that an extension of the subtraction method is required. Indeed additional terms can be added to the auxiliary cross section $\mathrm{d}\sigma_A$ such that it again pointwisely mimics the singular behavior of the real-emission contribution $\mathrm{d}\sigma_R$. Thus, the difference $\mathrm{d}\sigma_R - \mathrm{d}\sigma_A$ is once more finite by construction and can safely be integrated numerically in four dimensions. Again, the additional subtraction terms have to be added back to preserve the total cross section and this is possible since just as before since they can be constructed in a factorized and sufficiently simple form to allow for analytical integration. The complete resulting m-parton contribution is therefore given by

$$\int_m \left(\mathrm{d}\sigma_B + \mathrm{d}\sigma_V + \int_1 \mathrm{d}\sigma_A + \mathrm{d}\sigma_C \right) . \tag{2.30}$$

The contributions $\mathrm{d}\sigma_A$ and $\mathrm{d}\sigma_C$ contain both singular and finite parts. The insertion operator $\boldsymbol{I}$ that was already present in the case of non-hadronic initial states can be generalized to absorb the divergent parts from $\int_1 \mathrm{d}\sigma_A$ and $\mathrm{d}\sigma_C$ as well as some finite terms while the remaining finite parts are written as some new insertion operators $\boldsymbol{P}$ and $\boldsymbol{K}$.

2.4. The Subtraction Method by Catani and Seymour

In this section the subtraction method proposed by Catani and Seymour [1, 2] will be outlined. Even though this thesis deals with partons with finite masses the structure of the method in the massive case is very similar to the massless case which makes it possible and instructive to write both algorithms in an analogous form.

2.4.1. The Subtraction Method for Massless Partons

The Catani-Seymour subtraction method is based on the dipole picture where the splitting of a parton is not viewed as a $1 \to 2$ but as a $2 \to 3$ process, where apart from the splitting parton, the so-called *emitter*, a *spectator* parton is present as depicted in figure 2.2. The spectator absorbs a longitudinal recoil that arises when a splitting is performed with all participating partons remaining on their mass shells. There are four different configurations with the emitter and the spectator parton being either part of the initial or final state, i.e.

- final-state emitter and final-state spectator (FF) dipoles $\mathcal{D}_{ij,k}$
- final-state emitter and initial-state spectator (FI) dipoles $\mathcal{D}_{ij}^{a}$
- initial-state emitter and final-state spectator (IF) dipoles $\mathcal{D}_{j}^{ai}$
- initial-state emitter and initial-state spectator (II) dipoles $\mathcal{D}^{ai,b}$.

In lepton-lepton collisions partons are only present in the final state and therefore only the FF dipoles are relevant. If one initial-state hadron is considered also the FI and IF configurations are present and finally for the case of two incoming hadrons all four dipole configurations are needed.

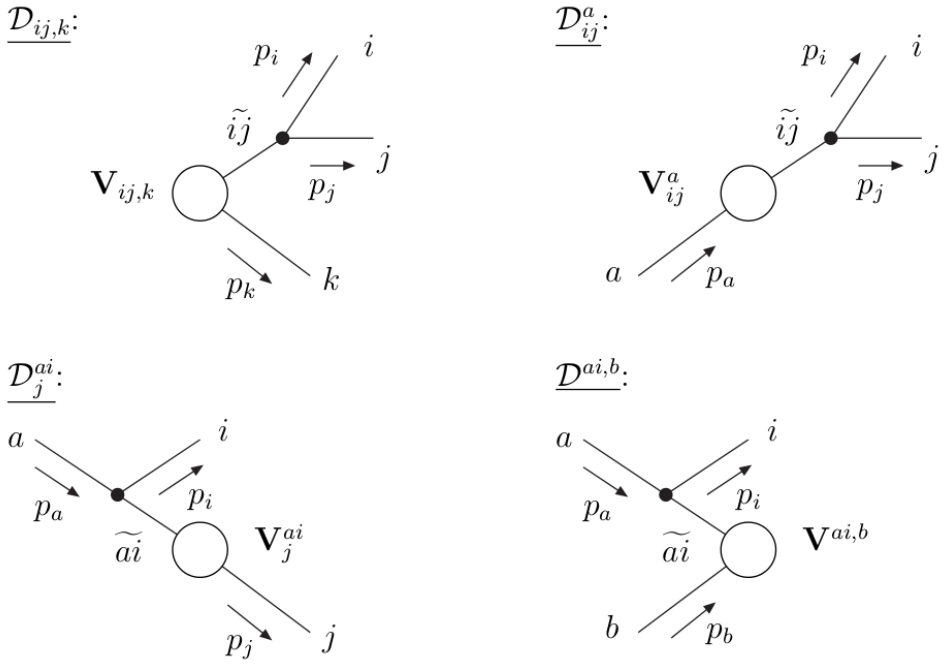

Figure 2.2.: In the dipole picture there are four different configurations depending on whether the emitter and the spectator are part of the initial or the final state. These configurations are called final-final (FF, upper left panel), final-initial (FI, upper right panel), initial-final (IF, lower left panel) and initial-initial (II, lower right panel). Picture taken from [11].

The Subtraction Terms

The subtraction term is constructed as a sum over all possible dipole configurations, i.e. all possible combinations of two partons are formed to build an emitter while every single one of the remaining partons is considered a spectator. Thus. in the case of hadron-hadron collisions the subtracted real-emission contribution is given by

$$\begin{aligned} &\mathrm{d}\sigma_R - \mathrm{d}\sigma_A \qquad (2.31)\\ &= \mathcal{SF}\left[\left|\mathcal{M}_1^{(0)}(\Phi_{m+1})\right|^2 F_J^{(m+1)}(\Phi_{m+1}) - \sum_{\substack{\text{splittings}\\ \&\text{ spectators}}} \mathcal{D}(\Phi_{m+1}) F_J^{(m)}(\tilde{\Phi}(\Phi_{m+1}))\right] \mathrm{d}\Phi_{m+1}\ . \end{aligned}$$

Each dipole configuration comes with their own kinematics which includes a projection $\tilde{\Phi}(\Phi_{m+1})$ from the $m+1$-particle final state of the real-emission kinematics to a corresponding Born-type m-particle final state. More explicitly, the sum over all relevant

splittings and spectators for the case of hadron-hadron collisions is given by

$$\begin{aligned}
&\sum_{\text{dipoles}} \mathcal{D}(\Phi_{m+1}) F_J^{(m)}(\tilde{\Phi}_m(\Phi_{m+1})) \\
&= \sum_{\substack{\text{pairs}\\ i,j}} \sum_{k\neq i,j} \mathcal{D}_{ij,k}(p_1,\ldots,p_{m+1};p_a,p_b) F_J^{(m)}(p_1,\ldots,\tilde{p}_{ij},\tilde{p}_k,\ldots,p_{m+1};p_a,p_b) \\
&+ \sum_{\substack{\text{pairs}\\ i,j}} \Big[\mathcal{D}_{ij}^{a}(p_1,..,p_{m+1};p_a,p_b) F_J^{(m)}(p_1,..,\tilde{p}_{ij},..,p_{m+1};\tilde{p}_a,p_b) + (a\leftrightarrow b)\Big] \\
&+ \sum_{i} \sum_{k\neq i} \Big[\mathcal{D}_{k}^{ai}(p_1,..,p_{m+1};p_a,p_b) F_J^{(m)}(p_1,..,\tilde{p}_{k},..,p_{m+1};\tilde{p}_{ai},p_b) + (a\leftrightarrow b)\Big] \\
&+ \sum_{i} \Big[\mathcal{D}^{ai,b}(p_1,..,p_{m+1};p_a,p_b) F_J^{(m)}(\tilde{p}_1,..,\tilde{p}_{m+1};\tilde{p}_{ai},p_b) + (a\leftrightarrow b)\Big]
\end{aligned} \tag{2.32}$$

Each dipole $\mathcal{D}$ itself has the structure

$$\mathcal{D} = \begin{array}{c}\text{propagator-like}\\ \text{factor}\end{array} \times \begin{array}{c}\text{color \& spin-correlated}\\ \text{Born matrix element}\end{array} \otimes \begin{array}{c}\text{splitting}\\ \text{function}\end{array} , \tag{2.33}$$

e.g. the massless final-final dipole reads

$$\mathcal{D}_{ij,k} = -\frac{1}{2p_i\cdot p_j}\left|\mathcal{M}_{m+0}^{(0)}(\tilde{\Phi}(\Phi_{m+1}))\right|^2 \otimes \boldsymbol{V}_{ij,k}(p_i,p_j,p_k) \ . \tag{2.34}$$

The symbol $\otimes$ is a convenient short-hand that indicates color and spin correlations which in the notation from section 5.1 of [2] are given by

$$\begin{aligned}
&\left|\mathcal{M}_{m+0}^{(0)}(\tilde{\Phi}(\Phi_{m+1}))\right|^2 \otimes \boldsymbol{V}_{ij,k}(p_i,p_j,p_k) \\
&\qquad = \langle \ldots,\tilde{ij},\ldots,\tilde{k},\ldots | \frac{\boldsymbol{T}_k\cdot\boldsymbol{T}_{ij}}{\boldsymbol{T}_{ij}^2}\boldsymbol{V}_{ij,k}(p_i,p_j,p_k) | \ldots,\tilde{ij},\ldots,\tilde{k},\ldots\rangle
\end{aligned} \tag{2.35}$$

for the case of the FF configurations. The $\boldsymbol{T}_i$ are color-charge matrices and lead to the aforementioned color-correlations and the splitting functions $\boldsymbol{V}_{ij,k}$ are matrices in the helicity space of the emitter. The Born matrix element has to be evaluated at an m-particle final-state kinematics which is achieved by applying the $\tilde{\Phi}$ projection. The projections $\tilde{\Phi}$ and the splitting functions for the massless case for all of the four different dipole configurations and each of the possible splittings that may occur are given in section 5 of [2].

The Insertion Operators

As mentioned before the integrated subtraction terms and the collinear counterterm

$$\int_m \left(\int_1 \mathrm{d}\sigma_A + \mathrm{d}\sigma_C\right) \tag{2.36}$$

are rewritten as the insertion operators $\boldsymbol{I}$, $\boldsymbol{P}$ and $\boldsymbol{K}$. The m-parton NLO contribution $\bar{\mathcal{V}}$ is then given by

$$\begin{aligned}\bar{\mathcal{V}} = \sum_{a,b} \int_0^1 \mathrm{d}\eta_a \int_0^1 \mathrm{d}\eta_b \; f_a(\eta_a,\mu_F^2) f_b(\eta_b,\mu_F^2) \int_m \Big[&\mathcal{V}(p_a,p_b,\epsilon) + \boldsymbol{I}(\epsilon) \otimes \mathcal{B}_{ab}(p_a,p_b) \\ + \sum_{a'} \int_0^1 \mathrm{d}x \big(\boldsymbol{K}_{\mathrm{FS}}^{a,a'}(x) + \boldsymbol{P}^{a,a'}(xp_a,x,\mu_F^2)\big) &\otimes \mathcal{B}_{a'b}(xp_a,p_b) \\ + \sum_{b'} \int_0^1 \mathrm{d}x \big(\boldsymbol{K}_{\mathrm{FS}}^{b,b'}(x) + \boldsymbol{P}^{b,b'}(xp_b,x,\mu_F^2)\big) &\otimes \mathcal{B}_{ab'}(p_a,xp_b) \Big] \mathrm{d}\Phi_m \; . \end{aligned} \tag{2.37}$$

The term 'insertion operator' is suggested by the form of equation (2.35) which also applies to the operators $\boldsymbol{I}$, $\boldsymbol{P}$ and $\boldsymbol{K}$, e.g.

$$\mathcal{B}_{ab} \otimes \boldsymbol{I} = \langle 1,\ldots,m|\boldsymbol{I}|1,\ldots,m\rangle \tag{2.38}$$

After integration over the additional one-particle phase space only color correlations are left. The $\boldsymbol{I}$-operator contains all integrated subtraction terms as well as singularities from the collinear counterterm while the operators $\boldsymbol{P}$ and $\boldsymbol{K}$ are finite and in the case of the $\boldsymbol{K}$-operator dependent on the factorization scheme which is indicated by the index FS. In the following the different insertion operators will be discussed in more detail.

The factorized form of the dipoles 2.33 allows for the analytic integration of all parts related to the splitting. Let it be emphasized again that this only needed to be done once and for all. All process dependence is encoded in the Born, virtual and real-emission matrix elements while the subtraction algorithm itself is completely general. Since by construction the subtraction terms mimic the singularity structure of the real-emission contribution applying dimensional regularization and integrating the dipoles gives the same pole expansion in $1/\epsilon$ as the regularized virtual correction matrix elements. The insertion operator $\boldsymbol{I}$ for the massless algorithm is given in [2] as

$$\boldsymbol{I}(\epsilon) = -\frac{\alpha_s}{2\pi} \frac{(4\pi)^\epsilon}{\Gamma(1-\epsilon)} \sum_J \frac{1}{\boldsymbol{T}_J^2} \mathcal{V}_J(\epsilon) \sum_{K\neq J} \boldsymbol{T}_J \boldsymbol{T}_K \left(\frac{\mu^2}{2p_J p_K}\right)^\epsilon \tag{2.39}$$

with the functions

$$\mathcal{V}_J(\epsilon) = \boldsymbol{T}_J^2 \left(\frac{1}{\epsilon^2} - \frac{\pi^2}{3}\right) + \gamma_J \frac{1}{\epsilon} + \gamma_J + K_J + \mathcal{O}(\epsilon) \; . \tag{2.40}$$

There are different conventions regarding the expansion in $1/\epsilon$ that differ in finite terms and the $1/\epsilon$-poles. In the calculation of the virtual and insertion operator contributions the same scheme has to be chosen for both contributions in order to get the correct absolute value. A widely used scheme is the *expanded convention* where $(4\pi)^\epsilon/\Gamma(1-\epsilon)$ is kept as a common prefactor and the term $(\mu^2/(2p_I\cdot p_J))^\epsilon$ is expanded in ϵ as

$$\left(\frac{\mu^2}{2p_I\cdot p_J}\right)^\epsilon = 1 + \epsilon \ln\left(\frac{\mu^2}{2p_I\cdot p_J}\right) + \frac{\epsilon^2}{2}\ln^2\left(\frac{\mu^2}{2p_I\cdot p_J}\right) + \mathcal{O}(\epsilon^3) \tag{2.41}$$

and multiplied with the functions $\mathcal{V}_J(\epsilon)$ to give the full expansion including the divergent terms and thus enable explicit checks of the cancellation of all singularities. Applying this

convention to the γ_J-terms in $\mathcal{V}_J(\epsilon)$ and rewriting equation 2.39 in a form that will be more suitable for comparison with the massive algorithm later on yields

$$\begin{aligned}\boldsymbol{I}(\epsilon) = &-\frac{\alpha_s}{2\pi}\frac{(4\pi)^\epsilon}{\Gamma(1-\epsilon)} \\ &\times\sum_J\sum_{K\neq J}\frac{\boldsymbol{T}_J\boldsymbol{T}_K}{\boldsymbol{T}_J^2}\left[\boldsymbol{T}_J^2\left(\frac{\mu^2}{s_{JK}}\right)^\epsilon\left(\frac{1}{\epsilon^2}-\frac{\pi^2}{3}\right)+\frac{\gamma_J}{\epsilon}+\gamma_J\ln\frac{\mu^2}{s_{JK}}+\gamma_J+K_J\right].\end{aligned} \tag{2.42}$$

The sums over J and K run over all the initial- and final-state partons. $\boldsymbol{T}_J$ and $\boldsymbol{T}_K$ denote the color-charge operators and $s_{JK} = 2p_J\cdot p_K$. μ is the *'t Hooft mass* which is an auxiliary energy scale that enters in dimensional regularization. The other factors and constants are

$$\boldsymbol{T}_q^2 = \boldsymbol{T}_{\bar{q}}^2 = C_F = \frac{N_c^2-1}{2N_c} \qquad \boldsymbol{T}_g^2 = C_A = N_c \tag{2.43a}$$

$$\gamma_q = \gamma_{\bar{q}} = \frac{3}{2}C_F \qquad \gamma_g = \frac{11}{6}C_A - \frac{2}{3}T_R N_f \tag{2.43b}$$

$$K_q = K_{\bar{q}} = \left(\frac{7}{2}-\frac{\pi^2}{6}\right)C_F \qquad K_g = \left(\frac{67}{18}-\frac{\pi^2}{6}\right)C_A - \frac{10}{9}T_R N_f \tag{2.43c}$$

The normalization of the Gell-Mann matrices is usually chosen such that $T_R = 1/2$. Finally, let it be noted that all the above results are the expressions found when using conventional dimensional regularization. However, to change to other regularization schemes only minor changes in the form of additional finite terms have to be made. Some remarks in that regard are made in the added note at the very end of [2].

The insertion operator $\boldsymbol{P}^{a,a'}(xp,x,\mu_F^2)$ is given by

$$\boldsymbol{P}^{a,a'}(xp_a,x,\mu_F^2) = \frac{\alpha_s}{2\pi}P^{aa'}(x)\frac{1}{\boldsymbol{T}_{a'}^2}\sum_{I\neq a'}\boldsymbol{T}_I\boldsymbol{T}_{a'}\ln\frac{\mu_F^2}{2xp_a\cdot p_I} \tag{2.44}$$

where the sum over I runs over all partons and $P^{aa'}(x)$ denotes the +-regularized Altarelli-Parisi splitting probabilities that are given in equation (8.1) in appendix A.1.

The operator $\boldsymbol{K}_{\mathrm{FS}}^{a,a'}(x)$ depends on the factorization scheme used for the parton distributions and is given by

$$\begin{aligned}\boldsymbol{K}_{\mathrm{FS}}^{a,a'}(x) = \frac{\alpha_s}{2\pi}\Bigg\{&\overline{K}^{aa'}(x) - K_{\mathrm{FS}}^{aa'}(x) \\ &+\delta^{aa'}\sum_i\boldsymbol{T}_i\boldsymbol{T}_a\frac{\gamma_i}{\boldsymbol{T}_i^2}\left[\left(\frac{1}{1-x}\right)_+ + \delta(1-x)\right] - \boldsymbol{T}_b\boldsymbol{T}_{a'}\frac{1}{\boldsymbol{T}_{a'}^2}\tilde{K}^{aa'}(x)\Bigg\}\end{aligned} \tag{2.45}$$

with

$$\begin{aligned}\overline{K}^{aa'}(x) &= \hat{P}'_{aa'}(x) + P_{\mathrm{reg}}^{aa'}(x)\ln\frac{1-x}{x} \\ &+ \delta^{ab}\left[\boldsymbol{T}_a^2\left(\frac{2}{1-x}\ln\frac{1-x}{x}\right)_+ - \delta(1-x)(\gamma_a + K_a - \frac{5}{6}\pi^2\boldsymbol{T}_a^2)\right].\end{aligned} \tag{2.46}$$

The concrete expressions for the functions $\overline{K}^{ab}(x)$ as well as the definitions of $K_{\mathrm{FS}}^{aa'}(x)$, $\tilde{K}^{aa'}(x)$, $\hat{P}'_{aa'}(x)$ and $P_{\mathrm{reg}}^{aa'}(x)$ are given in appendix A.1.

Both in the $\boldsymbol{P}$ and $\boldsymbol{K}$ operators appear expressions of the form $(g(x))_+$ where $g(x)$ is a function of x that contains some divergence. Just as in the case of distributions this *plus prescription* is defined by its effect on a test function $f(x)$ which is given by

$$\int_0^1 f(x)[g(x)]_+ \mathrm{d}x := \int_0^1 [f(x) - f(1)]g(x)\mathrm{d}x \ . \tag{2.47}$$

This prescription serves to pick out the correct finite remainders that are left after cancellation of the IR divergences. More comments on the treatment of the plus prescriptions will be made in section 6.2 where the implementation of the algorithms in Herwig++/Matchbox will be discussed.

In summary, the following ingredients need to be provided for the application of the subtraction algorithm:

- Obviously, the usual Born, virtual and real-emission matrix elements are needed with the tree-level, i.e. the Born and the real-emission matrix elements being given in 4 dimensions and the virtual contribution in d dimensions.
- The color-correlated Born matrix elements in d dimensions for the integrated subtraction terms.
- The Born matrix elements in 4 dimensions including color and spin correlations for all external gluons for the subtraction terms.

2.4.2. The Subtraction Method for Massive Partons

The basic structure of the subtraction algorithm for massive partons is completely analogous to the massless case. However, the kinematic terms are algebraically more complex since they now include modifications due to the non-zero particle masses.

The Subtraction Terms

The kinematics is constructed such as to allow all partons except the incoming ones to be massive on-shell particles. Moreover, the splittings are performed in such a way that all of the involved partons remain on-shell both before and after the splitting. The massive dipole splitting functions and corresponding phase space definitions are given in section 5 of [11].

In order to understand the differences to the massless case let us have a look at the example of the massive FF dipole phase space. In section 2.2 the factorization of the real-emission phase space into a Born-type part and a splitting part was sketched in equation (2.21) as

$$\mathrm{d}\Phi_{m+1} = \mathrm{d}\tilde{\Phi}_m(\Phi_{m+1})\mathrm{d}\Phi_{\mathrm{add}}(\Phi_{m+1}) \ . \tag{2.48}$$

More concretely, the three-particle phase space that participates in the splitting in the case of the FF configurations factorizes as

$$\mathrm{d}\Phi(p_i, p_j, p_k; Q) = \mathrm{d}\Phi(\tilde{p}_{ij}, \tilde{p}_k; Q)[\mathrm{d}p_i(\tilde{p}_{ij}, \tilde{p}_k)] \tag{2.49}$$

for the massless case where $Q = p_i + p_j + p_k = \tilde{p}_{ij} + \tilde{p}_k$ denotes the total momentum of all splitting partners [2]. Q is invariant in the splitting since in the dipole picture the kinematics are constructed such as to balance the momenta among all three dipole partons. This is in contrast to the classical $1 \to 2$ splittings where a reshuffling of the

momenta between the splitting phase space and the other partons has to be performed in order to keep all particles on-shell. $\mathrm{d}\Phi(\tilde{p}_{ij}, \tilde{p}_k; Q)$ denotes the contribution of the dipole to the Born-type phase space and $[\mathrm{d}p_i(\tilde{p}_{ij}, \tilde{p}_k)]$ represents the remaining one-particle splitting phase space that was so far dubbed $\Phi_{\mathrm{add}}(\Phi_{m+1})$. For the massive case the FF phase space factorization becomes

$$\mathrm{d}\Phi(p_i, p_j, p_k; Q) = \mathrm{d}\Phi(\tilde{p}_{ij}, \tilde{p}_k; Q)[\mathrm{d}p_i(\tilde{p}_{ij}, \tilde{p}_k)]\theta(1 - \mu_i - \mu_j - \mu_k) \tag{2.50}$$

where $\mu_n = m_n/\sqrt{Q^2}$ for $n = i, j, k$. The additional step function θ merely reflects the fact that from a configuration with a given momentum only particles with certain maximum masses can be created.

In the massless case the splitting kinematics can be calculated from the momenta p_i, p_j and p_k as

$$y_{ij,k} = \frac{p_i p_j}{p_i p_j + p_j p_k + p_k p_i} \qquad \text{and} \qquad \tilde{z}_i = \frac{p_i p_k}{p_i p_k + p_j p_k} \ . \tag{2.51}$$

There is no straight-forward intuitive interpretation of the physical meaning of $y_{ij,k}$ and $\tilde{z}_i$ but it can be said that $\tilde{z}_i$ is influenced by the orientation of the spectator k relative to the splitting products i and j while $y_{ij,k}$ additionally takes into account the orientation of the splitting children i and j towards each other. The possible values for $y_{ij,k}$ and $\tilde{z}_i$ span the interval $[0, 1]$. In the collinear limit $\tilde{z}_i$ tends to the Altarelli-Parisi splitting variable z which describes the longitudinal momentum fraction of the parton i with respect to the emitter $\tilde{ij}$ (see sections 4.3 and 5.1 of [2]). In the soft limit, however, $y_{ij,k} \to 0$ and $\tilde{z}_i \to 1$. For the case of massive case the definitions of $y_{ij,k}$ and $\tilde{z}_i$ remain unchanged. Note that this is the case only for the FF and the IF configurations whereas in the FI configuration there are slight differences between the definitions for the massless and massive cases. Moreover, the allowed ranges for $y_{ij,k}$ and $\tilde{z}_i$ are reduced in the massive case to the intervals $[y_-, y_+]$ and $[z_-(y_{ij,k}), z_+(y_{ij,k})]$ where, for example, the boundaries for $y_{ij,k}$ are given by the expressions

$$y_- = \frac{2\mu_i\mu_j}{1 - \mu_i^2 - \mu_j^2 - \mu_k^2} \geq 0 \qquad \text{and} \qquad y_+ = 1 - \frac{2\mu_k(1 - \mu_k)}{1 - \mu_i^2 - \mu_j^2 - \mu_k^2} \leq 1 \ . \tag{2.52}$$

The Insertion Operators

In the massive case the $\boldsymbol{I}$-Operator is modified to read

$$\begin{aligned} \boldsymbol{I}(\epsilon) = &-\frac{\alpha_s}{2\pi}\frac{(4\pi)^\epsilon}{\Gamma(1-\epsilon)} \\ &\times \sum_J \sum_{K \neq J} \frac{\boldsymbol{T}_J \boldsymbol{T}_K}{\boldsymbol{T}_J^2} \left[\boldsymbol{T}_J^2 \left(\frac{\mu^2}{s_{JK}} \right)^\epsilon \left(\mathcal{V}_J^{(K)} - \frac{\pi^2}{3} \right) + \Gamma'_J + \gamma_J \ln \frac{\mu^2}{s_{JK}} + \gamma_J + K_J \right] \end{aligned} \tag{2.53}$$

with

$$\mathcal{V}_J^{(K)} = \begin{cases} \mathcal{V}_J(\epsilon, \kappa) & \text{for } J \in \mathrm{FS} \\ \mathcal{V}_J(\epsilon, \kappa = 2/3) & \text{for } J \in \mathrm{IS} \text{ and } K \in \mathrm{FS} \\ \frac{1}{\epsilon^2} & \text{for } J \in \mathrm{IS} \text{ and } K \in \mathrm{IS} \end{cases} \tag{2.54}$$

and

$$\Gamma'_J = \begin{cases} \Gamma_J(\epsilon) & \text{for } J \in \mathrm{FS} \\ \frac{\gamma_J}{\epsilon} & \text{for } J \in \mathrm{IS}. \end{cases} \tag{2.55}$$

When comparing this expression with the massless $\boldsymbol{I}$-operator in equation (2.42) one can see that the contributions for initial-state splittings with an initial-state spectator coincide.

This is exactly what is expected since also in the massive formalism initial-state partons have to be massless.

The functions $\mathcal{V}(\epsilon,\kappa) = \mathcal{V}_j(s_{jk},m_j,m_k,\{m_F\},\epsilon,\kappa)$ can be decomposed into a singular contribution $\mathcal{V}_j^{(\mathrm{S})}$ symmetric in the indices j and k and a neither symmetric nor singular part $\mathcal{V}_j^{(\mathrm{NS})}$, i.e.

$$\mathcal{V}_j(s_{jk},m_j,m_k,\{m_F\},\epsilon,\kappa) = \mathcal{V}_j^{(\mathrm{S})}(s_{jk},m_j,m_k,\epsilon) + \mathcal{V}_j^{(\mathrm{NS})}(s_{jk},m_j,m_k,\{m_F\},\kappa) \tag{2.56}$$

The singular part expanded in powers of ϵ reads

$$\begin{aligned}
\mathcal{V}_j^{(\mathrm{S})}(s_{jk},m_j>0,m_k>0,\epsilon) &= \frac{1}{v_{jk}}\left[\frac{1}{\epsilon}\ln\rho - \frac{1}{4}\ln^2\rho_j^2 - \frac{1}{4}\ln^2\rho_k^2 - \frac{\pi^2}{6}\right. \\
&\qquad \left. + \ln\rho\ln\frac{Q_{jk}^2}{s_{jk}}\right] && \text{(2.57a)} \\
\mathcal{V}_j^{(\mathrm{S})}(s_{jk},m_j>0,m_k=0,\epsilon) &= \frac{1}{2\epsilon^2} + \frac{1}{2\epsilon}\ln\frac{m_j^2}{s_{jk}} - \frac{1}{4}\ln^2\frac{m_j^2}{s_{jk}} - \frac{\pi^2}{12} \\
&\qquad -\frac{1}{2}\ln\frac{m_j^2}{s_{jk}}\ln\frac{s_{jk}}{Q_{jk}^2} - \frac{1}{2}\ln\frac{m_j^2}{Q_{jk}^2}\ln\frac{s_{jk}}{Q_{jk}^2} && \text{(2.57b)} \\
\mathcal{V}_j^{(\mathrm{S})}(s_{jk},m_j=0,m_k=0,\epsilon) &= \frac{1}{\epsilon^2} && \text{(2.57c)}
\end{aligned}$$

where

$$Q_{jk}^2 = s_{jk} + m_j^2 + m_k^2 \qquad \mu_n^2 = \frac{m_n^2}{Q_{jk}^2} \qquad v_{jk} = \sqrt{1 - \frac{p_j^2 p_k^2}{(p_j p_k)^2}} \tag{2.58}$$

$$\rho = \sqrt{\frac{1-v_{jk}}{1+v_{jk}}} \qquad \rho_n = \sqrt{\frac{1-v_{jk}+2\mu_n^2/(1-\mu_j^2-\mu_k^2)}{1+v_{jk}+2\mu_n^2/(1-\mu_j^2-\mu_k^2)}} \quad (n=j,k) \tag{2.59}$$

The non-singular part $\mathcal{V}_j^{(\mathrm{NS})}(s_{jk},m_j,m_k,\{m_F\},\kappa)$ is given in appendix A.2. Expanding $(\mu^2/s_{JK})^\epsilon$ as in equation (2.41) one can obtain the expanded form of this part of the $\boldsymbol{I}$-operator with the complete pole coefficients. If the pole structure of $\mathcal{V}_J$ is written as

$$\mathcal{V}_J = V_J^{(-2)}\cdot\frac{1}{\epsilon^2} + V_J^{(-1)}\cdot\frac{1}{\epsilon} + V_J^{(0)} \tag{2.60}$$

with the superscript in parentheses denoting the order of the pole the term contains then one gets the following overall pole structure out of combining $\mathcal{V}_J$ with the expansion of $(\mu^2/s_{JK})^\epsilon$:

$$\text{double poles } 1/\epsilon^2 \text{ from} \qquad V_J^{(-2)} \tag{2.61}$$

$$\text{single poles } 1/\epsilon \text{ from} \qquad V_J^{(-1)} + V_J^{(-2)}\ln\tfrac{\mu^2}{s_{JK}} \tag{2.62}$$

$$\text{finite parts from} \qquad V_J^{(0)} + V_J^{(-1)}\ln\tfrac{\mu^2}{s_{JK}} + V_J^{(-2)}\tfrac{1}{2}\ln^2\tfrac{\mu^2}{s_{JK}}\ . \tag{2.63}$$

The functions Γ_j only contain single poles $1/\epsilon$ and read

$$\Gamma_g(\{m_F\},\epsilon) = \frac{1}{\epsilon}\gamma_g - \frac{2}{3}T_R\sum_{F=1}^{N_F}\ln\frac{m_F^2}{Q_{\text{aux}}^2} \tag{2.64}$$

$$\Gamma_q(\epsilon) = \frac{1}{\epsilon}\gamma_q \tag{2.65}$$

$$\Gamma_Q(\mu,m_Q,\epsilon) = C_F\left(\frac{1}{\epsilon}+\frac{1}{2}\ln\frac{m_Q^2}{\mu^2}-2\right) \tag{2.66}$$

The term

$$\frac{2}{3}T_R\sum_{F=1}^{N_F}\ln\frac{m_F^2}{Q_{\text{aux}}^2} \tag{2.67}$$

cancels against the same contribution in $\mathcal{V}_g^{(\text{NS})}$ which is given in appendix A.2.

The $\boldsymbol{P}$-operator is identical to the massless case and is given by

$$\boldsymbol{P}^{a,a'}(xp_a,x,\mu_F^2) = \frac{\alpha_s}{2\pi}P^{aa'}(x)\frac{1}{\boldsymbol{T}_{a'}^2}\sum_{I\neq a'}\boldsymbol{T}_I\boldsymbol{T}_{a'}\ln\frac{\mu_F^2}{xs_{Ia}} \tag{2.68}$$

where $P^{aa'}(x)$ denote the Altarelli-Parisi splitting probabilities that are given in equation (8.1) in appendix A.

In contrast to $\boldsymbol{P}$ the $\boldsymbol{K}$-operator is modified in the case of massive partons and is now given by the rather lengthy expression

$$\begin{aligned}
\boldsymbol{K}_{\text{FS}}^{aa'}(x) = \frac{\alpha_s}{2\pi}\Bigg\{ & \overline{K}^{aa'}(x) - K_{\text{FS}}^{aa'}(x) \\
& - \sum_j \boldsymbol{T}_j\boldsymbol{T}_{a'}\mathcal{K}_j^{a,a'}(x,s_{ja},m_j,\{m_F\}) \\
& - \frac{1}{\boldsymbol{T}_{a'}^2}\sum_j \boldsymbol{T}_j\boldsymbol{T}_{a'}\Bigg[P_{\text{reg}}^{aa'}(x)\ln\left(\frac{(1-x)s_{ja}}{(1-x)s_{ja}+m_j^2}\right) \\
& + \gamma_a\delta^{aa'}\delta(1-x)\left(\ln\frac{s_{ja}-2m_j\sqrt{s_{ja}+m_j^2}+2m_j^2}{s_{ja}} + \frac{2m_j}{\sqrt{s_{ja}+m_j^2}+m_j}\right)\Bigg] \\
& - \boldsymbol{T}_b\boldsymbol{T}_{a'}\left[\frac{1}{\boldsymbol{T}_{a'}^2}P_{\text{reg}}^{aa'}(x)\ln(1-x) + \delta^{aa'}\left(\left(\frac{2}{1-x}\ln(1-x)\right)_+ - \frac{\pi^2}{3}\delta(1-x)\right)\right]\Bigg\}
\end{aligned} \tag{2.69}$$

where some new functions $\mathcal{K}_j^{a,a'}$ have been introduced. Their definition is given in appendix A.2.

Chapter 3

Parton Showers and Matching

At the LHC the number of jets that can be resolved in final states is roughly about $\mathcal{O}(10)$ [13, 14]. Matrix elements give an accurate description of the interactions at a certain fixed order in perturbation theory, provided the observable is sufficiently *inclusive* and the final-state particles are well-separated. However, for events with a multitude of jets this will not be the case anymore. Instead, a resummation of the scale hierarchies, which span the range from the hard interaction to increasingly soft radiation, is needed in this context. Also, while it is theoretically possible to calculate matrix elements for processes with such a large number of final-state partons they would be quite complicated and time-consuming to generate and sample with current technology. Hence, a different strategy is needed to go beyond the usual $2 \to n$ calculations with $n = 2, 3, 4$ based on Feynman diagrams and get an explicit handle on higher multiplicities.

Furthermore, the soft radiation that is present in QCD increases towards lower energy scales and finally culminates in confinement and hadronisation. At this stage of the calculation several hundreds or thousands of particles are present in a single proton-proton collision event. Monte Carlo event generators seek to give an *exclusive* description at this level of detail, far beyond the reach of fixed-order calculations, and in the end output hadron-level final states.

Parton showers provide the means to fill in the gap in both of these cases. They allow for the evolution of events from the high energy scales associated with the hard process down to the low energy scales associated with hadronisation. Let it be emphasized that parton showers still belong to the realm of perturbation theory whereas the models of fragmentation and hadronisation do not.

3.1. The Parton Shower Approximation

The standard approach to obtain a first idea about the leading contributions for QCD radiation is to investigate the processes $e^+e^- \to q\bar{q}$ and $e^+e^- \to q\bar{q}g$. If the gluon kinematics

is parametrized in terms of the energy fraction z and the angle θ between the gluon and the quark, the cross section can according to [14] and [15] be written as

$$\frac{\mathrm{d}\sigma_{q\bar{q}g}}{\mathrm{d}z\mathrm{d}\cos\theta} = \sigma_{q\bar{q}} \times \frac{\alpha_s}{2\pi} C_F \left[\frac{2}{\sin^2\theta} \frac{1+(1-z)^2}{z} - z \right] \tag{3.1}$$

with the color factor $C_F = (N_C^2 - 1)/2N_C = 4/3$. From this expression two classes of divergences can be seen: The *collinear* singularities that arise for $\theta = 0$ and $\theta = \pi$, i.e. whenever the gluon is collinear to either the quark or the antiquark, and the *soft* singularity for $z = 0$. By rewriting

$$\frac{2\mathrm{d}\cos\theta}{\sin^2\theta} \approx \frac{\mathrm{d}\theta^2}{\theta^2} + \frac{d\bar{\theta}^2}{\bar{\theta}^2} \qquad \text{with} \qquad \bar{\theta} = \pi - \theta \tag{3.2}$$

this can be approximately decomposed into two contributions, where the gluon is either emitted by the quark or by the antiquark

$$\mathrm{d}\sigma_{q\bar{q}g} \approx \sigma_{q\bar{q}} \sum_{j=q,\bar{q}} \frac{\alpha_s}{2\pi} C_F \frac{\mathrm{d}\theta_j^2}{\theta_j^2} \frac{1+(1-z)^2}{z} \mathrm{d}z \ . \tag{3.3}$$

One finds that this factorization property is general for QCD matrix elements in the collinear limit, i.e. for small values of θ, and has the following structure:

$$\mathrm{d}\sigma_{m+1} \approx \mathrm{d}\sigma_m \sum_{\substack{\text{partons } i \\ \text{emissions } j}} \frac{\alpha_s}{2\pi} \frac{\mathrm{d}\theta^2}{\theta^2} P_{ij}(z)\mathrm{d}z \ . \tag{3.4}$$

In analogy to the introductory example, a sum is performed over all splittings that lead to the desired configuration. The collinear singularities for $\theta = 0$ are factored off from the *DGLAP splitting functions* $P_{ij}(z)$ originally derived by Dokshitzer [16], Gribov and Lipatov [17] and Altarelli and Parisi [18] which describe the emission of a parton j by a parton i. Some - but not all - of the splitting functions $P_{ij}(z)$, that are also referred to as *shower kernels* for reasons that will become obvious later on, contain a soft divergence for $z = 0$. The explicit expressions for four spacetime dimensions can e.g. be found in [14] or [4] or obtained from the formulas for d dimensions given in equation 8.12 in appendix A.1 by letting $\epsilon \to 0$. Let it be noted that instead of the emission angle θ other variables such as the transverse momentum $p_\perp^2 = z^2(1-z)^2\theta^2E^2$ or the virtuality $q^2 = z(1-z)\theta^2E^2$ could be used, where E denotes the energy of the parton before the splitting. In fact, any other quantity Q^2 that is related to the others by

$$\frac{\mathrm{d}\theta^2}{\theta^2} = \frac{\mathrm{d}p_\perp^2}{p_\perp^2} = \frac{\mathrm{d}q^2}{q^2} = \frac{\mathrm{d}Q^2}{Q^2} \tag{3.5}$$

would be suited and result in exactly the same mathematical expression as equation 3.4 [14, 15]. In the following the symbol Q^2 will be used to indicate a generic ordering variable. Again, the term *ordering variable* will become plausible in the next section.

The situation in the soft limit, i.e. for small energy fractions z but not necessarily small angles θ, is slightly different. In contrast to the collinear case, here the factorization between the hard process and the soft splitting already takes place at the amplitude level. The emission of a soft gluon j by two partons i and k for instance can in the soft limit be written as [19]

$$\mathrm{d}\sigma_{m+1} \propto \left(\frac{2s_{ik}}{s_{ij}s_{jk}} - \frac{2m_i^2}{s_{ij}^2} - \frac{2m_k^2}{s_{jk}^2} \right) \times \mathrm{d}\sigma_m \ . \tag{3.6}$$

- Collinear Factorization

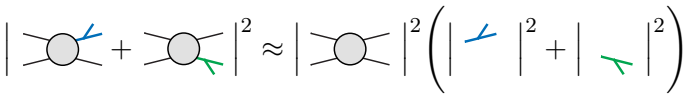

- Soft Factorization

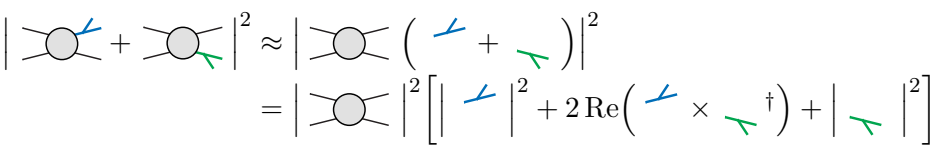

- Dipole/Antenna Factorization

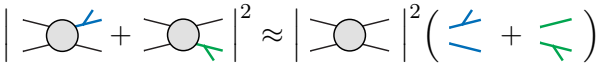

Figure 3.1.: Schematic depiction of the different types of factorizations and splitting functions and the resulting terms in the summation over emitters and splittings. Note that for the sake of clarity only the simplest situation was sketched which corresponds to the contributions present in the process $e^+e^- \to q\bar{q}$.

The factor in parenthesis is called *soft eikonal factor*. Again this factor holds in general for arbitrary QCD processes and for massless partons can be expressed as [14]

$$\mathrm{d}\sigma_{m+1} = \mathrm{d}\sigma_m \frac{d\omega}{\omega} \frac{d\Omega}{2\pi} \frac{\alpha_s}{2\pi} \sum_{i,j} C_{ij} W_{ij} \tag{3.7}$$

with

$$W_{ij} = \omega^2 \frac{p_i p_j}{(p_i q)(q p_j)} \ . \tag{3.8}$$

It is important to note that in the soft regime the interference terms dominates and thus the emission cannot be interpreted as coming from either of the partons separately but rather as being emitted by pairs of colored particles. Pictorially speaking, the long wavelength associated with the low energy of the emitted particle cannot resolve the emitting partons. This is in contrast to the collinear limit where the interference terms are left out. The different types of factorizations and the resulting terms are sketched in figure 3.1.

A special property of the soft limit is that emissions only occur inside of cones around the emitting partons with the cone sizes given by the angular separation of the interfering partons. This behavior can be restored in collinear factorization if angular ordering, i.e. evolution in something like $\mathrm{d}\theta^2$, is chosen as it was and is being done in Herwig and Herwig++.

In contrast to the ordinary splitting which is a $1 \to 2$ process the idea behind the *dipole* or *antenna* picture is to radiate off a colored dipole consisting of two partons, the *emitter* and the *spectator*, in a $2 \to 3$ process. In this way four-momentum conservation can be asserted while all particles remain on their mass shells in a natural and easy way. This is not as easily possible in the case of $1 \to 2$ splittings. Since in the dipole picture the emitted particle is radiated off the whole dipole the soft emission case is not considered separately from collinear emission but directly built in. This is in contrast to the treatment

of conventional showers with $1 \to 2$ splittings where the emission matrix element can be written as a sum over the emissions off each leg only in the case of collinear emissions. Thus, soft coherence effects are more naturally incorporated in the dipole picture.

Independently of whether the collinear or the soft limit, dipoles or antennae are considered or which kinematical parametrization is used, the general structure is always

$$\mathrm{d}\sigma_{m+1} \approx \mathrm{d}\sigma_m \times \sum_{\substack{\text{emitters and} \\ \text{splittings}}} \frac{\alpha_s}{2\pi} \cdot \text{phase space} \cdot \text{splitting function} \tag{3.9}$$

and from this basic formulation the construction of a parton shower algorithm will be outlined in the next section.

3.2. Basic Parton Shower Algorithms

The form of equation (3.4) already suggests that leading contributions from subsequent emissions can be estimated to all orders by a Markov chain, i.e. a recursive, history-independent procedure, that evolves a state from a high scale with well-separated emissions to lower scales with increasingly soft and collinear emissions. Hence the term *ordering variable* for Q^2. Let us repeat equation 3.4 in a slightly modified and generalized version in order to stress that the following treatment seeks to be agnostic of the concrete choices of kinematical parametrizations and splitting functions:

$$\mathrm{d}\sigma_{m+1} \approx \mathrm{d}\sigma_m \sum_{i,j} \frac{\alpha_s}{2\pi} \frac{\mathrm{d}Q^2}{Q^2} P_{ij}(z, Q^2)\mathrm{d}z \tag{3.10}$$

i represents the emitter, which may be either a single parton as in the case of classical showers with $1 \to 2$ splittings or a color dipole as in the case of dipole or antenna showers with $2 \to 3$ splittings. j indicates the kind of splitting that happens. From this the differential probability of having a parton or dipole i perform a splitting into an interval $[Q^2, Q^2 + dQ^2]$ of the ordering variable is given by

$$\mathrm{d}\mathcal{P}_i(Q^2) = \frac{\alpha_s}{2\pi} \frac{\mathrm{d}Q^2}{Q^2} \sum_j \int_{z_-(Q^2)}^{z_+(Q^2)} P_{ij}(z, Q^2)\mathrm{d}z \ , \tag{3.11}$$

where $z_\pm(Q^2)$ may take into account phase space boundaries due to kinematical restrictions as e.g. in the case of massive partons. We now want to derive the probability $\Delta_i(Q^2, q^2)$ of having no splitting between an upper value Q^2 and a lower value q^2. According to the definition of differentiation we have

$$\frac{\mathrm{d}\Delta_i(Q^2, q^2)}{\mathrm{d}q^2} = \frac{\Delta_i(Q^2, q^2 + \mathrm{d}q^2) - \Delta_i(Q^2, q^2)}{\mathrm{d}q^2} \ . \tag{3.12}$$

Given the definition of Δ_i as a non-emission probability and since $d\mathcal{P}_i$ denotes the differential emission probability, we have

$$\Delta_i(Q^2, q^2 - \mathrm{d}q^2) = \Delta_i(Q^2, q^2) \cdot (1 - \mathrm{d}\mathcal{P}_i(q^2)) \tag{3.13}$$

and conversely also

$$\Delta_i(Q^2, q^2 + \mathrm{d}q^2) = \Delta_i(Q^2, q^2) \cdot (1 + \mathrm{d}\mathcal{P}_i(q^2)) \ . \tag{3.14}$$

Thus, the evolution of $\Delta(Q^2, q^2)$ for different values of the lower scale q^2 is governed by the differential equation

$$\frac{\mathrm{d}\Delta_i(Q^2, q^2)}{\mathrm{d}q^2} = \Delta_i(Q^2, q^2)\frac{\mathrm{d}\mathcal{P}_i}{\mathrm{d}q^2} \tag{3.15}$$

This differential equation can be solved by separation of variables and subsequent integration from a lower scale μ^2_{IR} to the upper scale Q^2. Requiring $\Delta(Q^2, Q^2) = 1$ one obtains the *Sudakov form factor*

$$\Delta_i(Q^2, \mu^2_{\mathrm{IR}}) = \exp\left[-\frac{\alpha_s}{2\pi}\int_{\mu^2_{\mathrm{IR}}}^{Q^2}\frac{\mathrm{d}q^2}{q^2}\sum_j\int_{z_-(Q^2)}^{z_+(Q^2)} P_{ij}(z, q^2)\mathrm{d}z\right] = \exp\left[-\int_{\mu^2_{\mathrm{IR}}}^{Q^2}\mathrm{d}\mathcal{P}_i(q^2)\right]. \tag{3.16}$$

The quantity

$$\Gamma(q^2) = \int_{z_-(q^2)}^{z_+(q^2)} P(z, q^2)\mathrm{d}z \tag{3.17}$$

is called *Sudakov anomalous dimension*. To obtain no splitting at all by none of the partons or dipoles i between the scales Q^2 and μ^2_{IR} one simply needs to multiply all the corresponding Sudakov factors to obtain

$$\Delta(Q^2, \mu^2_{\mathrm{IR}}, \Phi_m) = \prod_i \Delta_i(Q^2, Q_0^2) = \exp\left[-\frac{\alpha_s}{2\pi}\int_{\mu^2_{\mathrm{IR}}}^{Q^2}\frac{\mathrm{d}q^2}{q^2}\sum_{i,j}\int_{z_-(Q^2)}^{z_+(Q^2)} P_{ij}(z, q^2)\mathrm{d}z\right]. \tag{3.18}$$

Here, the phase space dependence was made explicit in order to emphasize that the product has to be performed over all partons present in the phase space configuration Φ_m. Besides the relation $\Delta_i(Q^2, Q^2) = 1$ that is already clear from the very definition of the Sudakov form factor, one can also see, that for vanishing P_{ij}, i.e. no possible splitting, $\Delta(Q^2, q^2, \Phi_m) = 1$, so the probability for no emission is unity. Correspondingly, for very large P_{ij}, $\Delta_i(Q^2, q^2)$ vanishes, indicating that emissions become certain. Another useful property of the Sudakov form factor is its transitivity, i.e.

$$\Delta(Q_0^2, Q_1^2, \Phi_m)\Delta(Q_1^2, Q_2^2, \Phi_m) = \Delta(Q_0^2, Q_2^2, \Phi_m) \tag{3.19}$$

In order to establish at which scale q^2 the next emission is going to happen for a given parton configuration with Q^2 it is necessary to derive an expression for the emission probability distribution. This is precisely given by

$$\Delta(Q^2, q^2, \Phi_m) \cdot \frac{\mathrm{d}\mathcal{P}}{\mathrm{d}q^2}\ , \tag{3.20}$$

which has a Sudakov factor vetoing emissions above the scale q^2 and $\mathrm{d}\mathcal{P}/\mathrm{d}q^2$ which is the probability distribution for an emission at q^2. On the other hand this is just the right-hand side of the differential equation 3.15 describing the evolution of the Sudakov form factor, summed over all splittings. Thus, the desired emission probability distribution is just the derivative of the Sudakov form factor with respect to the lower scale

$$\frac{\mathrm{d}}{\mathrm{d}q^2}\Delta(Q^2, q^2, \Phi_m)\ . \tag{3.21}$$

Having this result at hand we can now sketch all the steps that form part of a parton shower starting from a hard event at a scale $Q^2 = Q_0^2$ and $k = 0$:

- One way of generating emissions according to the probability distribution given by the derivative of the Sudakov form factor is to invert and sample its integral, the Sudakov form factor itself. This is done by generating a random number $r_k \in \mathcal{U}([0,1])$ where $\mathcal{U}([0,1])$ represents the uniformly distributed random numbers between 0 and 1 and solving the equation $r_k = \Delta(Q_k^2, Q_{k+1}^2, \Phi_{m+k})$ for the variable Q_{k+1}^2 which describes the scale of the next emission done by the parton shower. Note however, that the implementation is nowadays done differently in practice for technical reasons. In Herwig++ the *veto algorithm* is used which is built on a modified version of a *von Neumann accept-reject algorithm*. It is described in [20], in appendix A3 of [15] and in [21].

- Because of its perturbative nature we cannot describe the behavior at arbitrarily small scales with the parton shower. On the contrary, below certain scales perturbation theory is not justified any more and hadronisation models are needed. Therefore, some lower parton shower cut off μ_{IR} is needed, which in practice is mostly chosen to be around $1 \ldots 2$ GeV. So in the second step we need to verify whether the scale of the next emission that was determined in the previous step is above this shower cut off. If not, the emission is vetoed and the event is passed over to the hadronisation handlers.

- If on the other hand the emission lies above μ_{IR} then we need to determine what kind of splitting j to take place and what emitting parton or dipole i was involved. This can of course be done by comparing the relative contributions $P_{ij}(z, Q_{k+1}^2)$ of all the different possible splittings.

- Having performed the splitting the child parton is considered as a new possible parent for another splitting and the whole procedure is repeated over and over again from the beginning with increasing k until no more splittings can be performed above the infrared shower cut off μ_{IR}.

3.3. Matching of Fixed-Order NLO Calculations and Parton Showers

As described so far, parton showers give an all-order resummation of the leading contributions and are necessary in Monte Carlo QCD calculations in order to have a correct estimation of soft and collinear splittings while matrix elements are accurate to a certain order in perturbation theory and correctly describe the associated hard emissions. However, when trying to improve the accuracy of a leading-order Monte Carlo calculation by naively including next-to-leading order matrix elements for the hard process, *double-counting* occurs. It arises since a parton shower acting on a Born contribution and producing an emission mimics the contribution that is more accurately described by the real emission part of the NLO matrix elements. Likewise, other contributions generated by the parton shower produce double-counting with respect to the virtual corrections. The procedure of adapting the calculation so as to avoid this double-counting is called *matching*.

Before turning to the mathematical expressions that arise in the context of NLO matching let us build up the ingredients step by step. Using $\mathrm{d}\mathcal{P} = \sum_i \mathrm{d}\mathcal{P}_i$ for the total differential emission probability summed over all possible splittings i the parton shower algorithm outlined in section 3.2 can be cast in mathematical notation as a *parton shower operator*

$\mathrm{PS}[Q^2, \mu^2_{\mathrm{IR}}, \Phi_m, O]$. This operator evolves a state between an upper scale Q^2, which represents the scale of the hard process, and a lower scale μ^2_{IR}, which is the infrared cutoff of the shower and marks the transition to non-perturbative physics. It may be written as

$$\begin{aligned}\mathrm{PS}[Q^2, \mu^2_{\mathrm{IR}}, \Phi_m, O] = \Delta(Q^2, \mu^2_{\mathrm{IR}}, \Phi_m) O_m(\Phi_m) \\ + \int_{\mu^2_{\mathrm{IR}}}^{Q^2} \mathrm{d}\mathcal{P}(q^2) \Delta(Q^2, q^2, \Phi_m)\, \mathrm{PS}[q^2, \mu^2_{\mathrm{IR}}, \Phi_{m+1}, O]\ ,\end{aligned} \tag{3.22}$$

which closely follows the form in [19]. O denotes the observable of interest which is calculated from the respective n-emission final states Φ_{m+n}. There are two possibilities for the evolution between Q^2 and μ^2_{IR}: Either there may be no emission generated by the parton shower as expressed by the Sudakov factor $\Delta(Q^2, \mu^2_{\mathrm{IR}}, \Phi_m)$ in the first term or there may be an emission at an intermediate scale q^2 as represented by $\mathrm{d}\mathcal{P}(q^2)$ in the second term. Obviously then there has to be no emission between Q^2 and q^2 which is the reason for the Sudakov factor $\Delta(Q^2, q^2, \Phi_m)$. Since the intermediate scale q^2 may be anywhere between Q^2 and μ^2_{IR} it is integrated over. Finally, additional emissions may occur below q^2 and thus the parton shower operator for evolution between q^2 and μ^2_{IR} is recursively inserted in the second term.

Note that when the total inclusive cross section is calculated instead of a differential or exclusive observable, i.e. $O = 1$, upon iteration of equation 3.22 one obtains

$$\begin{aligned}&\mathrm{PS}[Q^2, \mu^2_{\mathrm{IR}}, \Phi_m, 1] \\ &= \Delta(Q^2, \mu^2_{\mathrm{IR}}, \Phi_m) + \int_{\mu^2_{\mathrm{IR}}}^{Q^2} \mathrm{d}\mathcal{P}(q^2) \Delta(Q^2, q^2, \Phi_m)\, \mathrm{PS}[q^2, \mu^2_{\mathrm{IR}}, \Phi_{m+1}, 1] \\ &= \Delta(Q^2, \mu^2_{\mathrm{IR}}, \Phi_m) + \int_{\mu^2_{\mathrm{IR}}}^{Q^2} \mathrm{d}\mathcal{P}(q^2) \Delta(Q^2, q^2, \Phi_m) \Delta(q^2, \mu^2_{\mathrm{IR}}, \Phi_{m+1}) \\ &\quad + \int_{\mu^2_{\mathrm{IR}}}^{Q^2} \mathrm{d}\mathcal{P}(q^2) \Delta(Q^2, q^2, \Phi_m) \int_{\mu^2_{\mathrm{IR}}}^{q^2} \mathrm{d}\mathcal{P}(q'^2) \Delta(q^2, q'^2, \Phi_{m+1}) \Delta(q'^2, \mu^2_{\mathrm{IR}}, \Phi_{m+2}) + \dots\end{aligned} \tag{3.23}$$

This really just is

$$\sum_{n=0}^{\infty} \text{probability for } n \text{ emissions} = 1 \tag{3.24}$$

and gives unity as it corresponds to the sum over all possibilities. Thus, parton showers do not modify the total inclusive cross section obtained from fixed-order calculations.

Let us now have a look at the situation for an observable O at leading order. From now on the explicit mentioning of the phase space dependence will be suppressed for the matrix elements. Likewise, all pdf factors and the corresponding sums over partons are suppressed for the sake of clarity. The pure LO prediction is calculated as

$$O_{\mathrm{LO}} = \int \mathrm{d}\Phi_m \mathcal{B} O_m\ . \tag{3.25}$$

When applying the parton shower to the prediction for O and including only the first splitting one obtains

$$\begin{aligned}&(O_{\mathrm{LO+PS}})_{1^{\mathrm{st}}\mathrm{emission}} \\ &= \int \mathrm{d}\Phi_m \mathcal{B} \Delta(Q^2, \mu^2_{\mathrm{IR}}, \Phi_m) O_m + \int \mathrm{d}\Phi_m \mathcal{B} \int_{\mu^2_{\mathrm{IR}}}^{Q^2} \mathrm{d}\mathcal{P}(q^2) \Delta(Q^2, q^2, \Phi_m) O_{m+1}\ .\end{aligned} \tag{3.26}$$

Expanding the Sudakov form factor

$$\Delta(Q^2, \mu_{\mathrm{IR}}^2, \Phi_m) = 1 - \int_{\mu_{\mathrm{IR}}^2}^{Q^2} \mathrm{d}\mathcal{P}(q^2) + \mathcal{O}(\alpha_s^2) \tag{3.27}$$

and truncating all terms beyond $\mathcal{O}(\alpha_s^{F+1})$ yields

$$\begin{aligned} &O_{\mathrm{LO+PS}} \\ &\quad = \int \mathrm{d}\Phi_m \mathcal{B} O_m(\Phi_m) + \int \mathrm{d}\Phi_m \mathcal{B} \int_{\mu_{\mathrm{IR}}^2}^{Q^2} \mathrm{d}\mathcal{P}(q^2) \left[O_{m+1} - O_m\right] + \mathcal{O}(\alpha_s^{F+2}) \ . \end{aligned} \tag{3.28}$$

Naively acting on the NLO cross section with the parton shower operator gives

$$\begin{aligned} O_{\mathrm{NLO+PS}}^{\mathrm{unmatched}} &= \int \mathrm{d}\Phi_m \left[\mathcal{B} + \bar{\mathcal{V}}\right] O_m \\ &+ \int \mathrm{d}\Phi_m \mathcal{B} \int_{\mu_{\mathrm{IR}}^2}^{Q^2} \mathrm{d}\mathcal{P}(q^2) \left[O_{m+1} - O_m\right] \\ &+ \int \mathrm{d}\Phi_{m+1} \left[\mathcal{R} O_{m+1} - \mathcal{A} O_m\right] + \mathcal{O}(\alpha_s^{F+2}) \end{aligned} \tag{3.29}$$

where $\bar{\mathcal{V}}$ denotes the m-parton contribution to the NLO cross section which is in full detail given in equation (2.37). This is just the combination of $O_{\mathrm{LO+PS}}$ with the usual NLO correction terms since any additional action of the parton shower on the NLO corrections results in terms of order $\mathcal{O}(\alpha_s^{F+2})$. The term in the second line is exactly the one that introduces the double counting since $\mathcal{B}\,\mathrm{d}\mathcal{P}(q^2)\mathcal{O}_{m+1}$ contains parts of the real emission $\mathcal{R}\mathcal{O}_{m+1}$ and $\mathcal{B}\,\mathrm{d}\mathcal{P}(q^2)\mathcal{O}_m$ parts of the virtual contributions in $\bar{\mathcal{V}}\mathcal{O}_m$.

There are different matching strategies with the same common goal of removing the double counting. According to [19] they can be categorized into phase space slicing, subtraction and unitarity methods, the second of which will be outlined in the following. As the name already suggests, the idea behind the subtraction methods is to subtract the terms responsible for the double counting and let the parton shower fill them in again so as to restore the correct NLO cross section. Thus, the matched cross section for the hard process generation would be

$$\begin{aligned} O_{\mathrm{NLO}}^{\mathrm{matched}} &= \int \mathrm{d}\Phi_m \left[\mathcal{B} + \bar{\mathcal{V}}\right] O_m \\ &- \int \mathrm{d}\Phi_m \mathcal{B} \int_{\mu_{\mathrm{IR}}^2}^{Q^2} \mathrm{d}\mathcal{P}(q^2) \left[O_{m+1} - O_m\right] \\ &+ \int \mathrm{d}\Phi_{m+1} \left[\mathcal{R} O_{m+1} - \mathcal{A} O_m\right] \ . \end{aligned} \tag{3.30}$$

Rearranging this according to the affected observable bin and the dimensionality of the phase space yields

$$\begin{aligned} O_{\mathrm{NLO}}^{\mathrm{matched}} &= \left\{ \int \mathrm{d}\Phi_m \left[\mathcal{B} + \bar{\mathcal{V}}\right] - \int \mathrm{d}\Phi_{m+1} \mathcal{A} + \int \mathrm{d}\Phi_m \mathcal{B} \int_{\mu_{\mathrm{IR}}^2}^{Q^2} \mathrm{d}\mathcal{P}(q^2) \right\} O_m \\ &+ \left\{ \int \mathrm{d}\Phi_{m+1} \mathcal{R} - \int \mathrm{d}\Phi_m \mathcal{B} \int_{\mu_{\mathrm{IR}}^2}^{Q^2} \mathrm{d}\mathcal{P}(q^2) \right\} O_{m+1} \ . \end{aligned} \tag{3.31}$$

Note however, that this expression does not generate separately finite observable values for m and $m+1$ parton events since the IR divergence of the real-emission contribution $\mathcal{R}O_{m+1}$ which is counted in the $m+1$ parton bin is not canceled by any other term. More specifically, the subtraction term $\mathcal{A}$ appears in combination with the m-parton observable O_m and the parton shower contribution $\mathcal{B}\,\mathrm{d}\mathcal{P}(q^2)$ which is counted in the $m+1$ parton bin is cut off for scales below μ_{IR}. As for the subtraction term this was already the case at fixed-order NLO. As a consequence, $m+1$-particle predictions that approach the m-particle limit diverge at fixed order. Examples for this in the process $pp \to t\bar{t}$ are the transverse momentum of the first jet in the limit $p_{\perp,\text{jet }1} \to 0$ or the transverse momentum of the top-antitop quark pair $p_{\perp,t\bar{t}} = (p_t + p_{\bar{t}})_\perp$ in the limit $p_{\perp,t\bar{t}} \to 0$ which will be treated in section 7.3. In order to obtain separately finite values for both configurations the quantity

$$\int \mathrm{d}\Phi_{m+1} \mathcal{A}_{\mathrm{bridge}}(\Phi_{m+1}) \cdot \theta(\mu_{\mathrm{IR}}^2 - q^2) \left[O_m - O_{m+1}\right]$$

can be added where $\mathcal{A}_{\mathrm{bridge}}$ is called *bridge cross section*. According to [22] this is just a power correction if infrared-safe observables are considered, i.e. it does not destroy the resummation of large logarithms that is done by the parton shower. Note that this additional term is restricted to the phase space region below the parton shower cutoff scale μ_{IR}. This term subtracts the real-emission singularity in the $m+1$-parton bin and the corresponding singularity of the subtraction term $\mathcal{A}$ in the m-parton bin.

More explicitly, the general matched cross section before the application of the parton shower is given by

$$\begin{aligned} O_{\mathrm{NLO}}^{\mathrm{matched}} = &\int \mathrm{d}\Phi_m \left[\mathcal{B} + \bar{\mathcal{V}}\right] O_m \\ &+ \left\{ \int \mathrm{d}\Phi_m \mathcal{B} \int_{\mu_{\mathrm{IR}}^2}^{Q^2} \mathrm{d}\mathcal{P}(q^2) + \int \mathrm{d}\Phi_{m+1} \left[\mathcal{A}_{\mathrm{bridge}} \cdot \theta(\mu_{\mathrm{IR}}^2 - q^2) - \mathcal{A}\right] \right\} O_m \\ &+ \left\{ \int \mathrm{d}\Phi_{m+1} \left[\mathcal{R} - \mathcal{A}_{\mathrm{bridge}} \cdot \theta(\mu_{\mathrm{IR}}^2 - q^2)\right] - \int \mathrm{d}\Phi_m \mathcal{B} \int_{\mu_{\mathrm{IR}}^2}^{Q^2} \mathrm{d}\mathcal{P}(q^2) \right\} O_{m+1} \ . \end{aligned} \tag{3.32}$$

Recall from chapter 2 that there is a freedom of choice regarding the subtraction terms $\mathcal{A}(\Phi_{m+1})$. The same is true for the bridge cross section $\mathcal{A}_{\mathrm{bridge}}(\Phi_{m+1})$ and also for the shower kernels as long as of course the same kernels are chosen for the matching subtraction in the hard process generation and for the parton shower which is applied afterwards. Any splitting functions that exhibit the correct singular behavior in the soft and collinear limits are suited for these tasks. Based on this fact two principal matching prescriptions based on the subtraction approach were formulated [15]:

- The MC@NLO method [23, 24, 25] can be recovered from equation (3.32) by choosing the real-emission matrix elements for the bridge cross section, i.e. $\mathcal{A}_{\mathrm{bridge}} = \mathcal{R}$, which results in

$$\begin{aligned} &O_{\mathrm{NLO}}^{\mathrm{MC@NLO}} \\ &= \left\{ \int \mathrm{d}\Phi_m \left[\mathcal{B} + \bar{\mathcal{V}} + \mathcal{B} \int_{\mu_{\mathrm{IR}}^2}^{Q^2} \mathrm{d}\mathcal{P}(q^2)\right] + \int \mathrm{d}\Phi_{m+1} \left[\mathcal{R}\theta(\mu_{\mathrm{IR}}^2 - q^2) - \mathcal{A}\right] \right\} O_m \\ &+ \left\{ \int \mathrm{d}\Phi_{m+1} \mathcal{R}\theta(q^2 - \mu_{\mathrm{IR}}^2) - \int \mathrm{d}\Phi_m \mathcal{B} \int_{\mu_{\mathrm{IR}}^2}^{Q^2} \mathrm{d}\mathcal{P}(q^2) \right\} O_{m+1} \ , \end{aligned} \tag{3.33}$$

and basing the parton shower on the splitting functions of the subtraction terms, i.e. $\mathcal{BP} = \mathcal{A}$, which yields

$$\begin{aligned} O_{\text{NLO}}^{\text{MC@NLO}} &= \left\{ \int \mathrm{d}\Phi_m \left[\mathcal{B} + \bar{\mathcal{V}}\right] + \int \mathrm{d}\Phi_{m+1} \left[(\mathcal{R} - \mathcal{A})\,\theta(\mu_{\text{IR}}^2 - q^2) - \mathcal{A}\,\theta(q^2 - Q^2)\right] \right\} O_m \\ &+ \left\{ \int \mathrm{d}\Phi_{m+1} \theta(q^2 - \mu_{\text{IR}}^2) \left[\mathcal{R} - \mathcal{A}\,\theta(Q^2 - q^2)\right] \right\} O_{m+1} \ . \end{aligned} \tag{3.34}$$

Note that choosing $\mathcal{A}_{\text{bridge}} = \mathcal{R}$ corresponds to separating the real-emission contribution into a finite and a singular part and counting the latter in the m-parton bin:

$$\begin{aligned} \mathcal{R}\mathcal{O}_{m+1} &= \left[\mathcal{R}\theta(q^2 - \mu_{\text{IR}}^2) + \mathcal{R}\theta(\mu_{\text{IR}}^2 - q^2)\right] \mathcal{O}_{m+1} \\ &\approx \mathcal{R}\theta(q^2 - \mu_{\text{IR}}^2)\mathcal{O}_{m+1} + \mathcal{R}\theta(\mu_{\text{IR}}^2 - q^2)\mathcal{O}_m \ . \end{aligned} \tag{3.35}$$

The original MC@NLO generator was built to generate the hard process according to equation (3.33) and pass these events to Herwig which would add the parton shower on top. Most commonly, the FKS subtraction terms [26, 27] were used.

In the hard process generation two types of events are created: The Born-like m parton configurations, which make up the second line in equation (3.33), are called S-events and the real-emission-like $m + 1$ parton configurations in the third line are referred to as H-events. The parton shower is applied to both of them. Note that the weights of the H-events become negative if the approximation based on the Born matrix elements and the shower kernels is larger than the exact expression in the real-emission matrix elements. This has a negative impact on the Monte Carlo uncertainty as will later become clear from equation (4.13) but in practice the fraction of events with negative weights normally is not more than about 10% which is an acceptable penalty [19].

- The POWHEG approach [28] was explicitly constructed so as to avoid the presence of negative weights. It effectively constitutes a matrix element correction for the parton shower since the ratio $\mathcal{R}/\mathcal{B}$ is used for the first emission. As described in [14], the POWHEG-matched cross section reads

$$O_{\text{NLO}}^{\text{POWHEG}} = \left\{ \int \mathrm{d}\Phi_m \left[\mathcal{B} + \bar{\mathcal{V}}\right] + \int \mathrm{d}\Phi_{m+1} \left[\mathcal{R} - \mathcal{A}\right] \right\} O_m \ , \tag{3.36}$$

which is just the total inclusive cross section, and the Sudakov form factor for the first emission is modified to

$$\Delta(Q^2, \mu_{\text{IR}}^2, \Phi_m) = \exp\left[- \int \frac{\mathrm{d}\Phi_{m+1}}{\mathrm{d}\Phi_m} \frac{\mathcal{R}}{\mathcal{B}}\, \theta(q^2 - \mu_{\text{IR}}^2) \right] \ . \tag{3.37}$$

Since all infrared divergences are canceled, the Born matrix element represents the largest contribution and consequently the weights are non-negative, thus motivating the name 'POsitive Weight Hard Emission Generator'. Note that for POWHEG the parton shower has to be ordered in hardness, i.e. some quantity like the transverse momentum of the emitted particles, in order to have the real emission be reproduced correctly by the first emission. For efficiency reasons subsequent emissions are again based on conventional splitting kernels $\mathcal{P}$.

In Herwig++/Matchbox the Catani-Seymour subtraction terms $\mathcal{A}_{\mathrm{CS}}$ are used both for the subtraction terms and the bridge cross section such that

$$\begin{aligned} O_{\mathrm{NLO}}^{\mathrm{matched}} &= \int \mathrm{d}\Phi_m \left[\mathcal{B} + \bar{\mathcal{V}}\right] O_m \\ &+ \left[\int \mathrm{d}\Phi_m \mathcal{B} \int_{\mu_{\mathrm{IR}}^2}^{Q^2} \mathrm{d}\mathcal{P}(q^2) - \int \mathrm{d}\Phi_{m+1} \mathcal{A}_{\mathrm{CS}} \theta(q^2 - \mu_{\mathrm{IR}}^2)\right] O_m \\ &+ \left[\int \mathrm{d}\Phi_{m+1} \mathcal{R} - \int \mathrm{d}\Phi_m \mathcal{B} \int_{\mu_{\mathrm{IR}}^2}^{Q^2} \mathrm{d}\mathcal{P}(q^2) - \int \mathrm{d}\Phi_{m+1} \mathcal{A}_{\mathrm{CS}} \theta(\mu_{\mathrm{IR}}^2 - q^2)\right] O_{m+1} \ . \end{aligned} \tag{3.38}$$

Chapter 4

The Monte Carlo Method

The exact analytical calculation of total or differential cross sections can only be achieved for a very limited number of examples. Once incoming hadrons are considered and ever more final-state particles are involved, the calculations increase in complexity and the corresponding integrals are no longer analytically solvable. Even worse, the high number of dimensions that comes along with complicated final states also prevents the use of standard numerical integration algorithms. On the other hand, the statistical interpretation of quantum physics already hints at an approach that has developed into one of the most important tools in high energy physics, the Monte Carlo method.

In the first two sections the Monte Carlo method and the generation of histogrammed distributions will be reviewed briefly, mostly for the sake of clarifying the notation and giving a motivation for the formulas that will be used in the remaining sections to derive a method for combining multiple event samples.

4.1. Monte Carlo Integration

The Riemann integral in one dimension is defined as

$$\int_a^b g(x)\,\mathrm{d}x = \lim_{N\to\infty} \frac{b-a}{N} \sum_{i=1}^{N} g(x_i) \ . \tag{4.1}$$

This can be generalized to d dimensions in a straightforward manner as

$$\Sigma := \int_\Omega g(\vec{x})\,\mathrm{d}^d\vec{x} = \lim_{N\to\infty} \frac{V}{N} \sum_{i=1}^{N} g(\vec{x}_i) \tag{4.2}$$

where V denotes the volume of the domain of integration Ω. The idea now is to use a sequence of (pseudo-)random numbers instead of the grid of cells $\vec{x}_i$ that is used in the definition of the Riemann integral. If the number of points used is large enough and the

random numbers are uniformly distributed this should be a good approximation of the true integral Σ. So let the estimator of the integral value Σ be

$$\sigma := \frac{V}{N} \sum_{i=1}^{N} g\left(\vec{r}_i\right) \ , \tag{4.3}$$

where the fact that random or pseudorandom numbers are used is emphasized by the symbol $\vec{r}$.

One can show several properties of this estimator that ensure the desired behavior of the calculation:

- Consistency

  $$\lim_{N\to\infty} \sigma = \Sigma \tag{4.4}$$

  A *consistent* estimator tends to the true value Σ in the limit of an infinite number of points.

- Bias

  $$E[\sigma] = \Sigma \tag{4.5}$$

  Estimators for which this property holds are called *unbiased*. This means that even for finite point numbers N the estimator does not systematically deviate from the true value Σ.

- Convergence

  $$\mathrm{Var}[\sigma] = \frac{V^2}{N} \mathrm{Var}[g] \tag{4.6}$$

  since

  $$\begin{aligned} \mathrm{Var}\left[\sigma\right] &= \mathrm{Var}\left[\frac{V}{N}\sum_{i=1}^{N} g(\vec{r}_i)\right] \overset{(a)}{=} \frac{V^2}{N^2}\sum_{i=1}^{N} \mathrm{Var}\left[g(\vec{r}_i)\right] \\ &\overset{(b)}{=} \frac{V^2}{N^2}\mathrm{Var}\left[g\right]\sum_{i=1}^{N} 1 = \frac{V^2}{N}\mathrm{Var}\left[g\right] \end{aligned} \tag{4.7}$$

  where (a) holds because the random numbers are uncorrelated and (b) because all random numbers $g(\vec{r}_i)$ are identically distributed.

  Obviously, the variance of the estimator decreases with the number of points, i.e. the estimator should converge to its expectation value.

All in all, the result σ of the Monte Carlo integration, which in our context is just the total cross section, and its error or uncertainty δ are given by

$$\sigma = \frac{V}{N}\sum_{i=1}^{N} g_i \qquad \text{and} \qquad \delta = \frac{V}{\sqrt{N(N-1)}}\sqrt{\sum_{i=1}^{N} g_i^2 - \frac{1}{N}\left(\sum_{i=1}^{N} g_i\right)^2} \ . \tag{4.8}$$

The factor $N-1$ stems from the fact that the standard deviation of a sample of N points with respect to the mean is given by

$$\frac{1}{\sqrt{N-1}}\sqrt{\sum_{i=1}^{N}\left(g_i - \bar{g}\right)^2} \tag{4.9}$$

with the mean

$$\bar{g} = \frac{1}{N} \sum_{i=1}^{N} g_i \tag{4.10}$$

also being calculated from the data. It can be shown that the naive expression

$$\frac{1}{\sqrt{N}} \sqrt{\sum_{i=1}^{N} (g_i - \bar{g})^2} \tag{4.11}$$

really is a biased estimator of the true standard deviation of the function g. It would only be unbiased if the mean $\bar{g}$ were replaced by the expectation value $E[g] = \mu_g$ which of course is unknown when given a finite data sample. A derivation of the formula for the standard deviation is given in the appendix.

From the expressions in (4.8) one can directly see two important features of Monte Carlo integration:

- The statistical error is independent of the number of dimensions d of the integral. This is in contrast to usual methods of numerical integration which normally behave worse than Monte Carlo for more than four dimensions. Therefore, Monte Carlo integration is the preferred choice for particle physics where high-dimensional integrals are common.
- The statistical error can be reduced by either sampling more points or by reducing the variance of the integrand. The latter fact leads to techniques such as importance sampling and multi-channel sampling.

With the abbreviations

$$G_1 := \sum_{i=1}^{N} g_i \qquad \text{and} \qquad G_2 := \sum_{i=1}^{N} g_i^2 \tag{4.12}$$

the above result can be written as

$$\sigma = \frac{V}{N} G_1 \qquad \text{and} \qquad \delta = \frac{V}{\sqrt{N(N-1)}} \sqrt{G_2 - \frac{1}{N} G_1^2} \; . \tag{4.13}$$

4.2. Distributions and Histograms

Differential cross sections cannot be calculated exactly by event generators based on the Monte Carlo method. However, it is possible to generate binned distributions that approximate the values of the exact differential distributions for each discrete bin. On the other hand, the differential cross section integrated over one bin is just a total cross section with cuts corresponding to the bin boundaries. This already suggests that the formulas for the total cross section and its error are closely linked to their counterparts for differential distributions.

Given a histogram with B equally-sized bins of width ΔX spanning the interval $[X_0, X_B]$ and therefore each bin b covering the interval $[X_{b-1}, X_b]$ the total cross section fulfills the relation

$$\sigma = \sum_{b=1}^{B} \sigma_b = \sum_{b=1}^{B} \int_{X_{b-1}}^{X_b} \frac{\mathrm{d}\sigma}{\mathrm{d}x}(x) \, \mathrm{d}x \; , \tag{4.14}$$

where σ_b denotes the total cross section cut to the boundaries of bin b. On the other hand, the sum over all bins can be inserted into the expression for the total cross section from the last section,

$$\sigma = \frac{V}{N} G_1 = \frac{V}{N} \sum_{i=1}^{N} g_i = \frac{V}{N} \sum_{i=1}^{N} \sum_{b=1}^{B} \theta(x_i - X_{b-1}) \theta(X_b - x_i) g_i = \sum_{b=1}^{B} \frac{V}{N} G_{1,b} \tag{4.15}$$

where the short-hand

$$G_{1,b} := \sum_{i=1}^{N} \theta(x_i - X_{b-1}) \theta(X_b - x_i) g_i \tag{4.16}$$

for the sum of weights in a specific bin b was introduced. Thus we have

$$\int_{X_{b-1}}^{X_b} \frac{\mathrm{d}\sigma}{\mathrm{d}x}(x) \mathrm{d}x = \sigma_b = \frac{V}{N} G_{1,b} = \frac{V}{N} \sum_{i=1}^{N} \theta(x_i - X_{b-1}) \theta(X_b - x_i) g_i \tag{4.17}$$

and for sufficiently narrow bins due to

$$\int_{X_{b-1}}^{X_b} \frac{\mathrm{d}\sigma}{\mathrm{d}x}(x) \mathrm{d}x \approx (X_b - X_{b-1}) \cdot \frac{\mathrm{d}\sigma}{\mathrm{d}x}(x_b) = \Delta X \cdot \frac{\mathrm{d}\sigma}{\mathrm{d}x}(x_b) \ , \tag{4.18}$$

where x_b is a point inside the bin b, we can approximate the exact value of the differential distribution with the expression

$$\sigma_x(x_b) := \frac{\mathrm{d}\sigma}{\mathrm{d}x}(x_b) \approx \frac{1}{\Delta X} \frac{V}{N} G_{1,b} \ . \tag{4.19}$$

Up to the factor accounting for the bin width this has exactly the same structure as the formula for the total cross section.

Likewise, the expression for the statistical uncertainty of the total cross section can be straight-forwardly generalized to give the uncertainty of a histogram bin as

$$\delta_x(x_b) = \frac{V}{\Delta X \sqrt{N(N-1)}} \sqrt{G_{2,b} - \frac{1}{N} G_{1,b}^2} \ . \tag{4.20}$$

with the additional short-hand

$$G_{2,b} = \sum_{i=1}^{N} \theta(x_i - X_{b-1}) \theta(X_b - x_i) g_i^2 \tag{4.21}$$

for the sum of the squared weights in each bin.

4.3. Combination of Multiple Monte Carlo Runs

Going from leading order to next-to-leading order or going from a fixed-order calculation to a more complicated simulation by switching on the parton shower or additional features of the event generator such as the hadronisation model drastically increases the computation time. Therefore, methods for speeding up the event generation become more important or even a necessity for sufficiently complicated processes and simulations.

The Monte Carlo method allows for an easy parallelization of the computational efforts. It is based on the generation of random numbers that should be truly independent and

uncorrelated. Therefore, it is straightforward to divide a large run up into several smaller jobs that run independently of each other and are combined afterwards.

The Rivet project provides on its webpage a Python script for the combination of the `*.aida` files produced by the Rivet toolkit [29]. However, with this script only jobs with equal numbers of events can be combined. Moreover, in Rivet 1.9.0 which was used throughout this thesis, the uncertainty of histogram bins is calculated as

$$\sqrt{G_{2,b}} \qquad \text{as opposed to} \qquad \sqrt{G_{2,b} - \frac{1}{N} G_{1,b}^2} \tag{4.22}$$

which was given in equation 4.20. Therefore, fully general equations for the combination of jobs with arbitrary number of events were derived.

In the previous sections the estimation of the cross section was given by

$$\sigma = \frac{V}{N} G_1 = \frac{V}{N} \sum_{i=1}^{N} g_i \ . \tag{4.23}$$

Now instead of simply one event sample consider M runs with $N^{(j)}$ events and an estimated integral value $\sigma^{(j)}$ each. If those had been calculated in a single run the weights would of course simply have been added up. Given the number of events, the integration volume and the final result the sum of the weights can be recovered and this can be used to deduce how to combine the different parallel runs to give a combined result σ. Note that this result is constructed such as to be the same as if all of the M parallel runs had been one single run with a total of

$$N = \sum_{j=1}^{M} N^{(j)} \tag{4.24}$$

events. The combined result for the cross section is then given by

$$\sigma = \frac{V}{N} \sum_{i=1}^{N} g_i = \frac{V}{N} \sum_{j=1}^{M} \sum_{i_j=1}^{N^{(j)}} g_{i_j} = \frac{V}{N} \sum_{j=1}^{M} \frac{N^{(j)} \sigma^{(j)}}{V} \tag{4.25}$$

and thus

$$\sigma = \frac{1}{N} \sum_{j=1}^{M} N^{(j)} \sigma^{(j)} \ . \tag{4.26}$$

Accordingly, one can derive the expression for the correct combination of statistical uncertainties as

$$\delta = \frac{1}{\sqrt{N(N-1)}} \sqrt{\sum_{j=1}^{M} \left(N^{(j)} {\sigma^{(j)}}^2 + N^{(j)} (N^{(j)} - 1) {\delta^{(j)}}^2 \right) - \frac{1}{N} \left(\sum_{j=1}^{M} N^{(j)} \sigma^{(j)} \right)^2} \tag{4.27}$$

the derivation of which is given in appendix C.1.

In the same fashion the formulas for the combined differential cross sections and their statistical uncertainties can be derived as

$$\sigma_x(x_b) = \frac{1}{N} \sum_{j=1}^{M} N^{(j)} \sigma_x^{(j)}(x_b) \tag{4.28}$$

and

$$\delta_x(x_b) = \frac{1}{N(N-1)} \times \sqrt{\sum_{j=1}^{M}\left[N^{(j)}{\sigma_x^{(j)}}^2(x_b) + N^{(j)}(N^{(j)}-1){\delta_x^{(j)}}^2(x_b)\right] - \frac{1}{N}\left(\sum_{j=1}^{M} N^{(j)}\sigma_x^{(j)}(x_b)\right)^2}\,, \tag{4.29}$$

the derivation of which is given in appendix C.2.

Chapter 5

Programs and Utilities

In this chapter, at first the structure and functionality of general-purpose Monte Carlo event generators will be outlined in section 5.1. Thereafter, the programs and tools used in this thesis will be discussed in the remaining sections.

5.1. General-Purpose Monte Carlo Event Generators

General-purpose Monte Carlo event generators are some of the most important workhorses in particle physics. The results of high energy collider experiments cannot be described and understood simply by means of Monte Carlo simulations at fixed-order level in perturbation theory. Modern colliders and in particular hadron colliders such as the Large Hadron Collider (LHC) provide a very challenging environment with events containing several hundreds or even thousands of particles.

Monte Carlo event generators aim at producing a realistic physics description of the events observed in the experiments and generate events with increasing complexity in multiple steps that are sketched in figure 5.1. At the core is the *hard process* which is the generation of particle configurations according to the matrix elements obtained in fixed-order perturbation theory. This is the process with the highest energy scale where the particles of interest, such as a Higgs boson or a pair of top quarks, are produced. The next step is the addition of initial- or final-state radiation which is done by means of a parton shower and effectively resums higher order corrections which are not taken into account by the fixed-order matrix elements for the hard process. Since perturbation theory ceases to be valid at lower energies, the parton shower is cut off at a small scale. The hadronization model subsequently clusters together the particles and creates hadrons out of them which may then decay to lighter particles according to the various accessible decay channels. Whenever the beam particles are not fundamental but composite particles, a constituent parton is extracted from each of the incoming hadron with a probability distribution given by the *parton distribution function* (pdf) that describes the momentum distribution of a specific parton inside the incoming hadron. The remainders of the incoming hadrons,

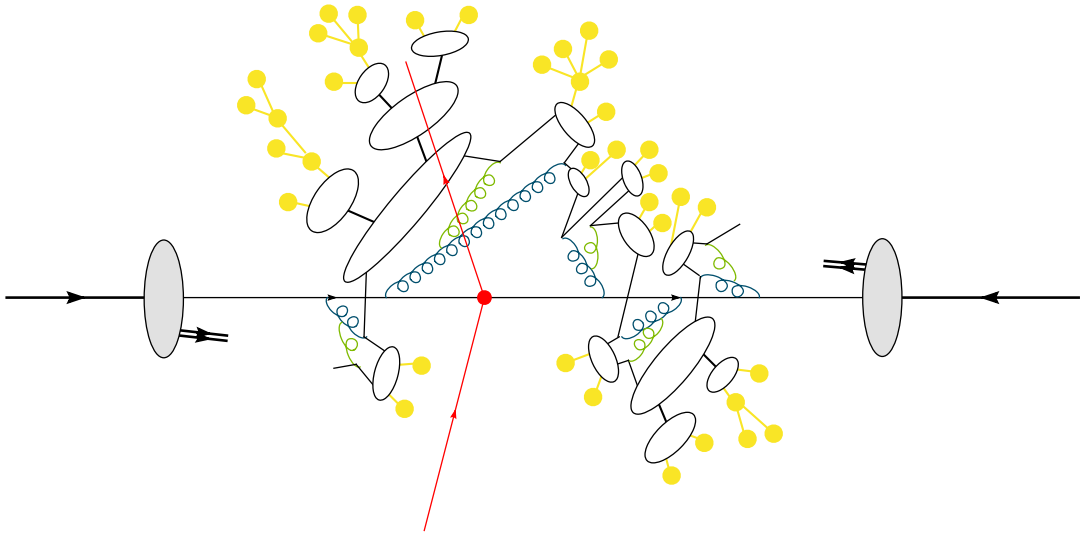

Figure 5.1.: Schematic representation of a hadron-hadron collision event as simulated by a general-purpose Monte Carlo event generator. Depicted are the hard interaction (red), initial-state radiation produced by the parton shower (green) and clustering, decays and hadronization. For the sake of clarity the underlying event is not displayed. Picture taken from [14].

usually referred to as *remnants*, that are left over after the parton extraction, however, can participate in further scattering or *multiple parton interactions* which gives rise to the *underlying event*.

The resulting set of final-state particles can be output as an event file specifying the particles and their momenta or directly passed to analysis software by means of which histograms for differential cross sections can be generated.

For an even more detailed simulation the events can be passed to dedicated detector simulations like Geant [30]. These feature an accurate model of the detector and provide detailed simulations of the reactions that the produced particles undergo when passing through the detector material. Also taken into account is the pile-up environment, i.e. multiple hard interactions during one detector readout period.

Let it be stressed that beside the convenient mathematical property which is the dimension-independent convergence rate a key feature of the Monte Carlo method is that its output closely resembles experimental results. Therefore many of the tools and techniques that are used in data analysis can also be applied to Monte Carlo data and thereby permit a close interplay between the two. One application of this is the use of Monte Carlo data in experimental analyses, as for instance in the discovery of the Higgs boson [31, 32].

5.2. Herwig++ and Matchbox

Herwig++ is one of the main general-purpose Monte Carlo event generators and as such has at its disposal all the different simulation steps such as hard process generation, parton shower, hadronization and multiple parton interaction outlined at the end of the previous chapter. `Matchbox` is an extension of Herwig++ that is dedicated to automated next-to-leading order calculations, the goal being to provide NLO accuracy per default.

For many years the most common procedure for the inclusion of a hard process in Monte Carlos has been the direct implementation of the amplitudes or matrix elements as source code. This approach has advantages of is own like the possibility to tailor the phase space generation specifically for each process and optimize for speed. However, with the development and availability of ever more programs for the automated generation of next-to-leading order matrix elements it became desirable to make use of these tools in the framework of general-purpose Monte Carlo event generators. With the Binoth Les Houches Accord (BLHA) [33, 34] a standard for the communication between Monte Carlo and external matrix element generators was proposed. These matrix element generators are usually referred to as matrix element or one-loop providers (OLPs). Both terms are often used interchangeably in this thesis. Apart from the interfaces built on the BLHA it is often also possible to implement direct dedicated interfaces to external matrix element providers. Both kinds of interfaces allow the event generators to request a specific process from the OLPs which then check whether they can provide the process and if so generate the corresponding matrix elements or call some precompiled process libraries. After an initialization phase, where e.g. parameters are communicated, the Monte Carlo generator can then obtain numerical results for generated phase-space configurations from the OLPs.

The upcoming Herwig++/Matchbox release is foreseen to feature interfaces to a variety of matrix element providers, including GoSam [35, 36, 37], HJets++ [38, 39], MadGraph [40], NJet, OpenLoops [41, 42, 43, 44] and VBFNLO [45]. In this thesis matrix elements provided by MadGraph, GoSam and OpenLoops were used. The interfaces to `GoSam` and OpenLoops are built on the Binoth Les Houches Accord and pass information on the matrix element level to Herwig++/Matchbox as opposed to the MadGraph interface which works on the amplitude level. The latter therefore allows for the passing of color information which is why Herwig++/Matchbox can add showers to tree-level, i.e. Born and real-emission, matrix elements generated by `MadGraph`. Furthermore, it is possible to combine tree-level matrix elements of one matrix element generator in conjunction with the matrix elements for virtual contributions by a different OLP. This specifically makes it possible to use tree-level amplitudes with color information by MadGraph combined with one-loop matrix elements by e.g. GoSam and finally add a parton shower on top.

Herwig++ features the so-called *repository* which is a virtual directory structure where in a combination of object orientation and file system behavior objects can be created, modified and sorted into different folders. A default repository layout is created during the installation and only modifications of this default setup have to be put in the infiles. In this setup switching from one OLP to another can be done by changing a few lines in the input files. Furthermore, a specific path to the location of previously compiled process libraries can be passed to some of the interfaces. This can be very useful since for sufficiently complicated processes the compilation of the matrix elements may take up both quite some time and disk space.

One particular feature of Herwig++ is the availability of two very different parton showers. The traditional angular-ordered shower that was the trademark of the original Fortran Herwig [46, 47, 48] is still available in a modified version in its successor Herwig++. Also available is a new dipole-type shower [49] built on the splitting functions that are used in the Catani-Seymour subtraction algorithm.

5.3. Rivet

Rivet (Robust Independent Validation of Experiment and Theory) [50] is a toolkit that allows for the comparison of Monte Carlo simulations and experimental data. Throughout this thesis Rivet 1.9.0 was used. On the one hand, Rivet provides libraries with more than 200 experimental analyses, including e.g. data from the LHC experiments ALICE, ATLAS, CMS and LHCb, while on the other hand it makes available to the user a variety of functions that can be used to analyze events generated in Monte Carlo simulations and produce histograms of physical observables. Amongst many other features the application of jet algorithms, that are part of FastJet, to final states is included. One possibility for passing events from the event generator to Rivet is via HepMC event files that are either written to disk or fed through a FIFO pipe [1]. However, Herwig++ has a direct interface that makes use of the API [2] exposed by Rivet such that the creation of HepMC output is not necessary. The desired Rivet analyses can simply be listed in the Herwig++ infile and will then be applied to the events during the event generation.

5.4. Herwig-Parallel

Herwig-Parallel is a collection of python scripts that were written during this thesis in order to start, monitor, control and merge parallel runs of Herwig++ on computer clusters. They allow for the creation of parallel runs consisting of an arbitrary number of jobs. More jobs can be added to an existing run thus making it easy to increase the statistics. Once all jobs of a run are finished they can be combined in order to obtain the final combined results for the total cross section and histograms that are either produced by Rivet or by analyses directly built into Herwig++. Several other control and configuration features are provided. These include e.g. automated and configurable consistency checks by means of which jobs that deviate significantly from the others can be identified in a run. This works even in the presence of very different statistics for each job. Also provided is a configuration system with which Herwig-Parallel can rapidly be adapted to different clusters and batch queue systems.

This way of implementing a parallelization of Herwig++ exploits the very nature of the Monte Carlo method which makes use of random numbers that should be independent. Thus, instead of having to implement a parallelized software execution at the program source code level by means of parallel programming techniques such as OpenMP or MPI one can simply run several statistically independent instances of the Monte Carlo generator and combine the results afterwards. The obvious advantages of this are the simplicity and great flexibility. One does not have to rely special platform or computer cluster infrastructures and it is even easily possible to combine the results obtained from different computer clusters.

Herwig-Parallel uses the formulas for the combination of total cross sections and histogrammed distributions that were given in section 4.3. However, since these where derived on the fully general basics of the Monte Carlo method there is a subtlety related to their use in the context of event generators. While for a standard Monte Carlo integration a weight of zero is perfectly normal, an event generator must not produce events with zero

[1] FIFO pipes are named pipes in Unix-like systems and can be used for communication between different processes without the need of writing data to the disk.

[2] The application programming interface (API) comprises the set of functions which can be called by other programs in order to interact with a certain program or library, i.e. in this case Rivet.

weight. These might be forbidden phase-space configurations or configurations that are vetoed by cuts. Therefore, one has to distinguish between Monte Carlo *attempts* and *events* where *attempt* refers to any particle configuration with any weight that is generated in a Monte Carlo run while *events* are only those configurations which have a non-zero weight and are therefore accepted as possible events and written to an event record or piped through the analysis toolchain. Since this distinction is no inherent part of the Monte Carlo integration the meaning of the variable N used throughout the previous chapter is the number of *attempts* and not the number of physical *events* produced by the generator.

As demonstrated in the previous chapter the only ingredients for the statistically correct combination of M independent jobs indexed by j are the information on the number of attempts $N^{(j)}$ for each of the jobs and obviously each of the obtained total and histogrammed cross sections and errors $\sigma^{(j)}$, $\delta^{(j)}$, $\sigma_x^{(j)}(x_b)$ and $\delta_x^{(j)}(x_b)$. While the latter are provided as the result of event generator runs, the number of *attempts* is not output by Herwig++, nor was Rivet 1.9.0 designed to use this information for the calculation of bin uncertainties. Due to this, patches were developed for ThePEG, Herwig++ and Rivet such as to provide all the necessary infrastructure for Herwig-Parallel. These patches consist of a modification of the API exposed by Rivet and of ThePEG's interface to Rivet in order to allow Herwig++ and ThePEG to pass the number of attempts to Rivet, a modification of the calculation of bin errors in Rivet and finally a Herwig++ analysis handler called `ParallelRunAnalysis`. When added to a Herwig++ infile with

```
cd /Herwig/Generators
create Herwig::ParallelRunAnalysis /Herwig/Analysis/ParallelRunAnalysis
    HwAnalysis.so
insert LHCGenerator:AnalysisHandlers 0 /Herwig/Analysis/ParallelRunAnalysis
```

the latter outputs the current numbers of attempts and events as well as the currently estimated total cross section and its uncertainty during the Herwig++ run.

Plots that demonstrate the correct working of the Herwig-Parallel scripts are given at the beginning of chapter 7.

5.5. MCFM

MCFM (Monte Carlo for FeMtobarn processes) [51] is a parton-level Monte Carlo program that only calculates the hard process in fixed-order perturbation theory but does not add any parton showers or hadronization effects. A variety of processes is available at next-to-leading order including the process $pp \to t\bar{t}$ with stable top quarks. Therefore MCFM was well-suited to serve as a baseline for validating the implementation of the Catani and Seymour algorithm with massive quarks. Since MCFM can neither create HepMC output nor be interfaced to Rivet it was necessary to implement the analysis for the comparison within `MCFM`. The booked and filled histograms are written to disk as a `C++` source code file which by means of Root can be converted to a `*.root` file. By using a set of tools that are shipped with Rivet it is possible to subsequently produce files that can be processed by `Rivet`. The entire toolchain for generating Rivet histogram plots from an MCFM run is the following:

1. `root <filename>.C` produces `<filename>.root`
2. `root2flat -f <filename>.dat <filename>.root` gives a file `<filename>.dat`

3. `flat2aida -o <filename>.aida <filename>.dat` finally outputs the `*.aida`-file that can be plotted with Rivet

Chapter 6

Implementation of the Catani-Seymour Algorithm in Herwig++

6.1. Dipoles

The dipole splitting functions that are used in the IR subtraction are located in the `MatrixElement/Matchbox/Dipoles` folder of the Herwig++ source tree. They are derived from the base class `SubtractionDipole`. Each dipole implements the function `canHandle` which, when the sum over all partons and dipoles is performed, establishes whether the current dipole is responsible for the proposed splitting and should be evaluated. Also implemented by each dipole is the function `me2` which returns the value of $\mathcal{D}$. Each dipole implementation includes the corresponding massless or massive tilde kinematics $\tilde{\Phi}(\Phi_{m+1})$ that calculates all the kinematical quantities such as $y_{ij,k}$ and $\tilde{z}_i$ in the case of the FF configurations from the $m+1$-parton real-emission final state. Using these variables the values of $\mathcal{D}$ can then be computed according to the formulas given in section 5 of [11].

6.2. Insertion Operators

In equation (2.37) the virtual and insertion operator contribution to the NLO cross section was given as

$$\begin{aligned}\sum_{a,b}\int_0^1 \mathrm{d}\eta_a \int_0^1 \mathrm{d}\eta_b\ f_a(\eta_a,\mu_F^2) f_b(\eta_b,\mu_F^2) \int_m \Big[\mathcal{V}_{ab} + \mathcal{B}_{ab}(p_a,p_b)\otimes \boldsymbol{I} \\ + \sum_{a'}\int_0^1 \mathrm{d}x \big(\boldsymbol{K}_{\mathrm{FS}}^{a,a'}(x) + \boldsymbol{P}^{a,a'}(xp_a,x,\mu_F^2)\big)\otimes \mathcal{B}_{a'b}(xp_a,p_b) \\ + \sum_{b'}\int_0^1 \mathrm{d}x \big(\boldsymbol{K}_{\mathrm{FS}}^{b,b'}(x) + \boldsymbol{P}^{b,b'}(xp_b,x,\mu_F^2)\big)\otimes \mathcal{B}_{ab'}(p_a,xp_b)\Big]\mathrm{d}\Phi_m\ .\end{aligned} \tag{6.1}$$

However, this form is not optimally suited for the implementation in a Monte Carlo generator since the Born contribution and the Born matrix elements that appear in combination with the $\boldsymbol{P}$- and $\boldsymbol{K}$-operators are evaluated with three different kinematics. Therefore, a slightly modified version is implemented in Herwig++/Matchbox. In the second line of equation (6.1) the η_a-integration is substituted for an integration over z_a which is defined as $z_a := x\eta_a$. Therefore the integration changes according to

$$\int_0^1 \mathrm{d}\eta_a = \int_0^x \frac{\mathrm{d}z_a}{x} = \int_0^1 \frac{\mathrm{d}z_a}{x}\theta(x - z_a) \; . \tag{6.2}$$

This modification is sketched in figure 6.1b. Renaming η_b as $z_b = \eta_b$ and applying the accordingly modified procedure to the first and the third line of equation (6.1) as well yields

$$\begin{aligned}
\sum_{a,b} \int_0^1 \mathrm{d}z_a \int_0^1 \mathrm{d}z_b \int_m \mathrm{d}\Phi_m \Bigg\{ & f_a(z_a, \mu_F^2) f_b(z_b, \mu_F^2) \left(\mathcal{V}_{ab} + \mathcal{B}_{ab}(z_a P_A, z_b P_B) \otimes \boldsymbol{I}\right) \\
& + \sum_{a',b'} \int_0^1 \frac{\mathrm{d}x}{x} \Bigg[\theta(x - z_a) f_a\left(\frac{z_a}{x}, \mu_F^2\right) f_b(z_b, \mu_F^2) \delta_{bb'} \left(\boldsymbol{K}_{\mathrm{FS}}^{a,a'}(x) + \boldsymbol{P}^{a,a'}(z_a P_A, x, \mu_F^2)\right) \\
& + \theta(x - z_b) f_a(z_a, \mu_F^2) f_b\left(\frac{z_b}{x}, \mu_F^2\right) \delta_{aa'} \left(\boldsymbol{K}_{\mathrm{FS}}^{b,b'}(x) + \boldsymbol{P}^{b,b'}(z_b P_B, x, \mu_F^2)\right) \Bigg] \\
& \otimes \; \mathcal{B}_{a'b'}(z_a P_A, z_b P_B) \Bigg\} \; .
\end{aligned} \tag{6.3}$$

This substitution has consequences on what quantities remain fixed during the x-integration. In the main part of [11] the variable $p_a = \eta_a P_A$ is constant during the integration over x which in turn only affects $p_{a'} = x p_a$. In the Herwig++/Matchbox implementation however, $p_{a'} = z_a P_A$ is kept constant during the x-integration which only has an effect on $p_a = \frac{z_a}{x} P_A$. This way, if a splitting occurs with a higher momentum fraction x transferred to the splitting child that subsequently participates in the hard process then parton a has to be extracted from hadron A with an accordingly lower momentum such as to keep $p_{a'}$ constant.

However, simply making the substitution for the $\boldsymbol{K}$- and $\boldsymbol{P}$-operators as in equation (6.3) will yield incorrect results. This is due to the fact that some parts of the finite $\boldsymbol{P}$- and $\boldsymbol{K}$-operators stem from the collinear counterterm while others result from the integration of the subtraction terms as sketched in figure 6.2. More specifically, only the finite functions $K_{\mathrm{FS}}^{aa'}$ in the $\boldsymbol{K}$-operator come from the collinear counterterm. In the case of the $\boldsymbol{P}$-operator singular terms from the collinear counterterm and from the integrated dipoles combine to give a finite result. Performing the above substitution therefore changes the way the integration of the dipoles is done and as a consequence its result. The core question is which quantities are kept fix during the x-integration when using the +- or the x_+-regularization prescriptions, which are defined in equations (5.54) and (5.55) of [11]. In the integration of the FI dipoles there are terms that simultaneously depend on x and on $\mu_n = m_n/\sqrt{2\tilde{p}_{ij} p_a}$ (with $n = i, j, ij$). The integration of the dipoles is carried out in such a way that μ_Q of the massive quark is considered an independent variable and kept fixed when x is integrated over (see section 5.2.3 of [11]). With the above substitution the definition of p_a is changed to $p_a = z_a/x \cdot P_A$ which is not independent of x anymore. This results in additional finite terms that have to be taken into account. These complications are treated in appendix B of [11], e.g. by replacing the functions $\mathcal{K}_j^{ab}$ with some new functions $\bar{\mathcal{K}}_j^{aa'}$ which are given

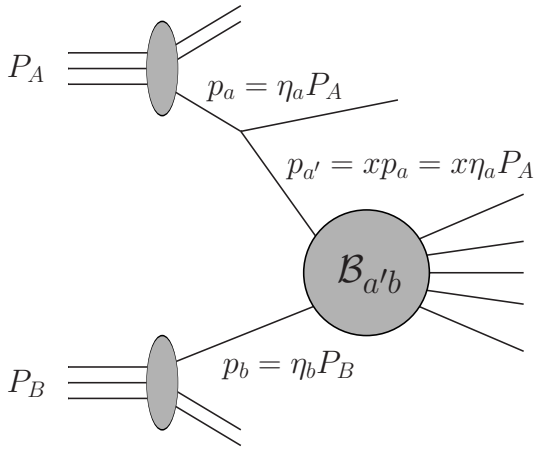

(a) Catani and Seymour

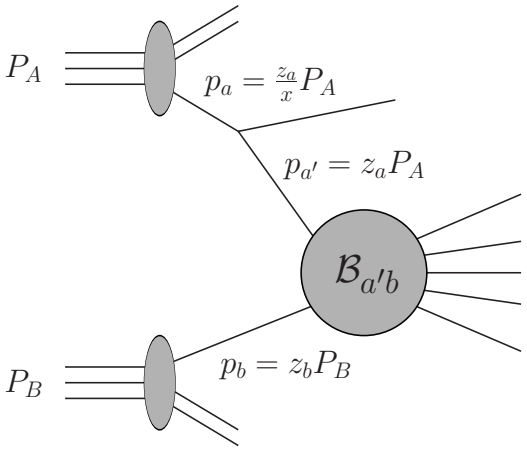

(b) After substituting $z_a := x\eta_a$

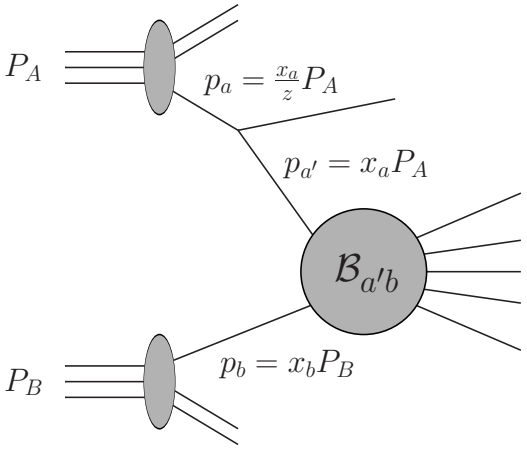

(c) Implementation in Herwig++/Matchbox

Figure 6.1.: Comparison of how the integrations over the parton distribution functions and a subsequent splitting are performed in the paper by Catani and Seymour and the implementation of the operators $\boldsymbol{P}$ and $\boldsymbol{K}$ in Matchbox. The implementation was modified such that the underlying Born matrix elements $\mathcal{B}_{a'b}$ and $\mathcal{B}_{ab'}$ are evaluated at the same incoming momenta as for the Born and virtual contribution which can be seen from equation 6.4.

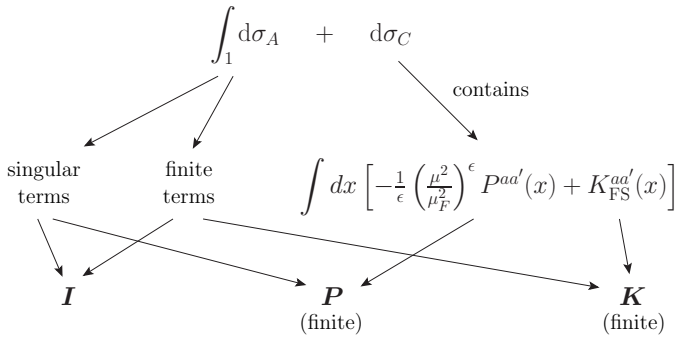

Figure 6.2.: Sketch of the different contributions to the insertion operators. For the sake of clarity only the relevant parts of the collinear counterterm $\mathrm{d}\sigma_C$ are explicitly given while additional factors have been left out.

in equations (B.17) and (B.18) of [11]. The $\boldsymbol{P}$-operator does not contain any dependence on μ_Q and therefore is not modified.

The substitution $z_a := x\eta_a$ had already been used in the implementation of the massless subtraction algorithm. However, the $\boldsymbol{K}$-operator is much simpler in the massless case and in particular does not feature terms depending on μ_Q since this quantity vanishes in the massless limit. As a consequence this complication had not been present in the existing implementation of the massless subtraction algorithm.

Finally, the variables x and z are interchanged in the Herwig++/Matchbox nomenclature (see figure 6.1c for a sketch), thus giving the expression

$$\begin{aligned}
&\sum_{a,b}\int_0^1 \mathrm{d}x_a \int_0^1 \mathrm{d}x_b \int_m \mathrm{d}\Phi_m \Bigg\{ f_a(x_a,\mu_F^2) f_b(x_b,\mu_F^2)\left(\mathcal{V}_{ab} + \mathcal{B}_{ab}(x_a P_A, x_b P_B)\otimes \boldsymbol{I}\right) \\
&\quad + \sum_{a',b'}\int_0^1 \frac{\mathrm{d}z}{z}\Bigg[\theta(z-x_a) f_a\left(\frac{x_a}{z},\mu_F^2\right) f_b(x_b,\mu_F^2)\delta_{bb'}\left(\boldsymbol{K}_{\mathrm{FS}}^{a,a'}(z) + \boldsymbol{P}^{a,a'}(x_a P_A, z, \mu_F^2)\right) \\
&\quad + \theta(z-x_b) f_a(x_a,\mu_F^2) f_b\left(\frac{x_b}{z},\mu_F^2\right)\delta_{aa'}\left(\boldsymbol{K}_{\mathrm{FS}}^{b,b'}(z) + \boldsymbol{P}^{b,b'}(x_b P_B, z, \mu_F^2)\right)\Bigg] \\
&\qquad\qquad \otimes\ \mathcal{B}_{a'b'}(x_a P_A, x_b P_B)\Bigg\}\,.
\end{aligned} \tag{6.4}$$

The implementations of the insertion operators are located in `MatrixElement/Matchbox/InsertionOperators`, the massive $\boldsymbol{I}$-operator in `DipoleMIOperator.cc` and the massive $\boldsymbol{P}$- and $\boldsymbol{K}$-operators in `DipoleMPKOperator.cc`. Both feature a function `apply(const cPDVector& pd)` that checks whether the partons involved require the use of the massive implementation. This is the case when either massive final-state particles are present or a gluon can split into a massive quark-antiquark pair. At the same time it is ensured that all initial-state particles are massless. The calculation of the finite parts is done in the functions `me2()` and the $\boldsymbol{I}$-operator features the additional functions `meLoopSinglePole()` and `meLoopDoublePole()` that return the coefficients of the $1/\epsilon$ and $1/\epsilon^2$ poles such as to enable pole cancellation checks as described in section 7.2.3.

The function `me2()` of the massive $\boldsymbol{P}$- and $\boldsymbol{K}$-operator checks which of the incoming particles are partons and have to be extracted from hadrons. It then triggers the calculation of the corresponding contributions by the function `sumParton(int id)` where `id` is either a' or b' depending on whether the terms in the second or the third line of equation (6.4) are to be calculated. If e.g. the second line is to be calculated, the factor $f_b(x_b, \mu_F^2)$ is included in the function `me2()`. The remaining part

$$\int_0^1 \mathrm{d}x_a \int_{x_a}^1 \frac{\mathrm{d}z}{z} \sum_a f_a\left(\frac{x_a}{z}, \mu_F^2\right) \left(\boldsymbol{K}_{\mathrm{FS}}^{a,a'}(z) + \boldsymbol{P}^{a,a'}(x_a P_A, z, \mu_F^2)\right) \otimes \mathcal{B}_{a'b}(x_a P_A, x_b P_B) \quad (6.5)$$

is then calculated in `sumParton(int id)`.

Chapter 7

Validations and Results

7.1. Combination of Parallel Runs

The formulas for the combination of total and differential cross sections and their respective errors where given in section 4.3 and the implementation in Herwig-Parallel was described in section 5.4. The correct working was tested by splitting a calculation into different numbers of jobs but with the same overall statistics. In figure 7.1 the results for several runs for the process $pp \to t\bar{t}j$ at leading order are depicted. The details of the setup are described in section 7.2 where the exact same calculation though with higher statistics is used for a comparison between Herwig++ and MCFM. In this section the focus will instead be on the combination of the jobs that are part of a run. As a baseline six conventional runs consisting of just a single job were run with different seeds for the random number generator and 25 million events each. In a next step parallel runs where the 25 million events where split up equally into a different number of jobs were run. More specifically, 6 runs with 10 $\times$ 2.5 million events, another 6 runs with 100 $\times$ 250k events and finally, titled 'even more jobs per run' in figure 7.1 runs with 250 $\times$ 100k, 500 $\times$ 50k and 1000 $\times$ 25k events were done. However, each of these runs so far consisted of jobs with the same number of events which is why in order to test the fully general case runs with heterogeneous event numbers had to be created. The following configurations were used and labeled 'mixed' in the figure:

- 10 $\times$ 1.2M + 100 $\times$ 130k events
- 10 $\times$ 1.2M + 500 $\times$ 26k events
- 2 $\times$ 4M + 20 $\times$ 400k + 225 $\times$ 40k events

As can be seen in fig 7.1 all total cross sections agree quite well within the error margins. Furthermore, since the number of events is kept at 25 million for all runs the errors should be of similar size and again it can be seen in the plot that this is indeed the case.

Some validation plots for the combination of differential cross sections are shown in figure 7.2. The plots depict the transverse momentum distributions of the top quark and the

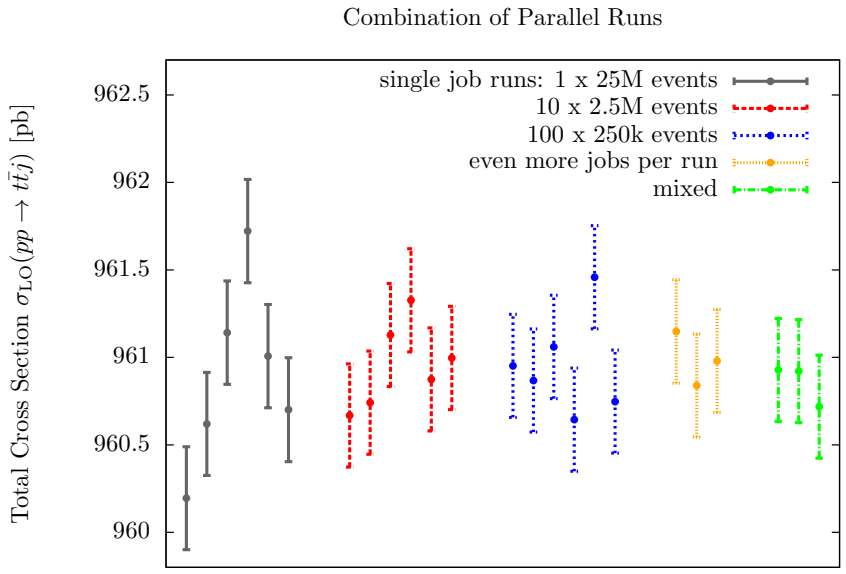

Figure 7.1.: Validation of the total cross sections obtained from the combination of parallel runs with the process $pp \to t\bar{t}j$ at fixed-order LO. Runs with equal statistics were split up. Several runs were repeated with different seeds for the random number generator.

jet in the process $pp \to t\bar{t}$ at fixed-order NLO. A run with a single job and 50 million events is compared against runs where the same number of events is split up into 10 or 100 equally sized jobs and another run consisting of differently sized jobs (10 x 4M + 100 x 400k + 600 x 100k events). As can be seen from the plots good agreement within the uncertainty margins is found for all runs independent of there composition. Apart from the central value also the statistical errors indicated by the error bars or the yellow band drawn for the single-job run in the ratio plot are of comparable sizes which indicates that the combination works in the desired way. Last but not least it can be seen that the fluctuations of the central values seem plausible compared to the given uncertainties.

7.2. Fixed-Order

In order to validate the implementation of the Catani-Seymour subtraction algorithm for processes including massive quarks in proton-proton collisions the process $pp \to t\bar{t}$ was studied at fixed order as a first benchmark. Herwig++/Matchbox was run with matrix elements provided by GoSam as well as MadGraph and OpenLoops via the respective OLP interfaces. MCFM was used as a baseline for the comparison. By using Herwig++/Matchbox with three different external OLPs it was ensured that the interfaces work correctly and that the matrix elements provided by the OLPs are in agreement.

7.2.1. Tree-level Contributions

As a first step comparisons for the tree-level processes $pp \to t\bar{t}$ and $pp \to t\bar{t}j$ with the massless jet constituents $j = \{g, u, \bar{u}, d, \bar{d}, s, \bar{s}, c, \bar{c}, b, \bar{b}\}$ were made in order to establish a

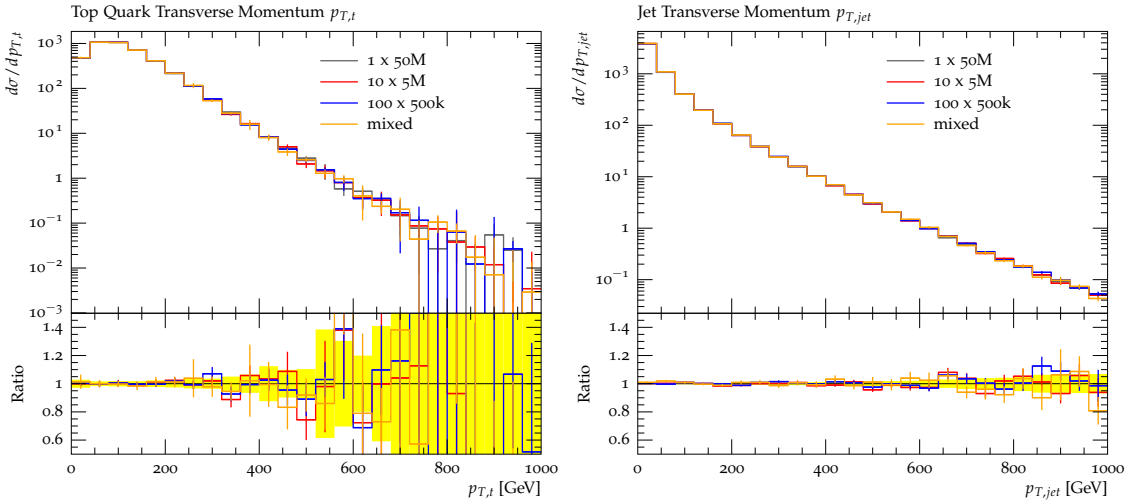

Figure 7.2.: Validation of the differential cross sections obtained from the combination of parallel runs with the process $pp \to t\bar{t}$ at fixed-order NLO. Runs with 50 million events were split up into a different number of parallel jobs and compared against a run with only one single job. For the run labeled 'mixed' jobs with different event numbers were combined (10 x 4M + 100 x 400k + 600 x 100k events).

baseline setup at LO. Even though the process including a jet only enters as a real-emission contribution for $pp \to t\bar{t}$ at NLO it is a worthwhile check to validate the corresponding matrix elements and phase space generation.

A fixed factorization and renormalization scale of

$$\mu_F = \mu_R = 80 \text{ GeV}$$

was used in order to rule out any deviations due to differences in the running of α_s. For both processes the CT10 parton distributions were used and a value of

$$\Lambda_{\text{QCD}} = 203.685184 \text{ MeV}$$

was set for Herwig++'s strong two-loop coupling in order to achieve a consistent value for α_s in Herwig++/Matchbox and MCFM of

$$\alpha_s^{(\text{MCFM})}(\mu_R^2) = \alpha_s^{(\text{Herwig++})}(\mu_R^2) = 0.12036114$$

For $pp \to t\bar{t}$ no cuts were applied whatsoever while for $pp \to t\bar{t}j$ the jet was required to have a transverse momentum of $p_{\perp,\text{jet}} \geq 20$ GeV and an absolute rapidity of $|y_{\text{jet}}| \leq 5$. Apart from the hard process generation all other features such as parton shower, hadronization and multiple parton interactions were disabled in Herwig++. The top quark was set stable and given a mass of $m_t = 173.5$ GeV. Runs were conducted for energies ranging from 7 TeV to 14 TeV and the initialization phase and the numbers of events were chosen such as to achieve a relative statistical uncertainty of 0.01% on the total cross sections for all runs.

The benchmark results for the total cross sections are depicted in figure 7.3 for the process $pp \to t\bar{t}$ and in figure 7.5 for $pp \to t\bar{t}j$ respectively. The total cross sections calculated by MCFM and Herwig++ are in good agreement even though the results of the Herwig++

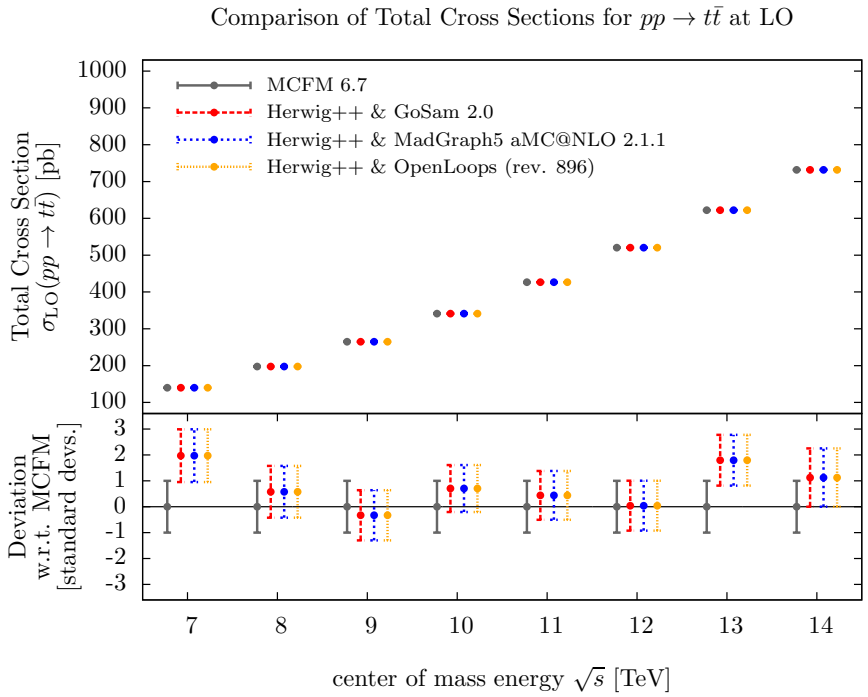

Figure 7.3.: Fixed-order comparison of total cross sections for the process $pp \to t\bar{t}$ at LO for different center-of-mass energies between MCFM and Herwig++ interfaced to either GoSam, MadGraph or OpenLoops. The error bars indicate the statistical uncertainty on the total cross section and are normalized to the results of the MCFM runs. The relative uncertainty of all the runs is about 0.01%.

runs seem to exhibit a very slight bias towards higher values in the case of $pp \to t\bar{t}$. This may be due to some differences in the internal workings of the phase space population between the generators. Let it be emphasized again however that the relative uncertainties are only about 0.01% for all runs and therefore the agreement is deemed sufficiently good for the purpose of this comparison. Very good agreement between MCFM and Herwig++ is also found for the differential cross sections. As an example the transverse momentum and rapidity distributions of the top quark are shown in figs. 7.4 and 7.6. More distributions are included in figs. D.1 and D.2 in appendix D. Furthermore it can be noted already from the plots that the Herwig++ runs with the different OLPs look exactly the same and indeed the numerical results are identical. The same holds for the differential distributions where again a look at the raw histogram data shows identical results. This is due to the fact that the generation and numerically stable evaluation of tree-level matrix elements is relatively straight forward. Since as a result of the numerically identical matrix elements the same phase space points are sampled by Herwig++ for all OLPs exactly identical results are obtained.

7.2.2. Real-Emission Contributions: Subtraction Checks

As pointed out in chapter 2.2 the IR subtraction term is constructed to approximate the real-emission matrix element in those phase space regions where a parton is either soft or collinear to another parton. The soft limit for a parton i can of course be probed with the variable E_i. For the collinear configurations of the partons i and j the variable

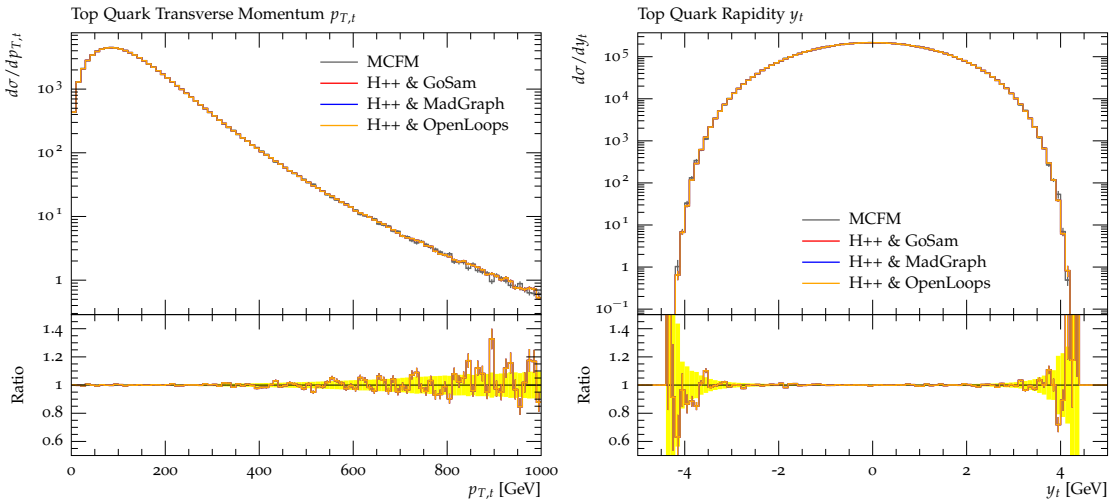

Figure 7.4.: Fixed-order comparison of the transverse momentum and rapidity distributions of the top quark for the process $pp \to t\bar{t}$ at LO for a center-of-mass energy of 14 TeV. The yellow error bands denote the statistical uncertainty for the results of MCFM.

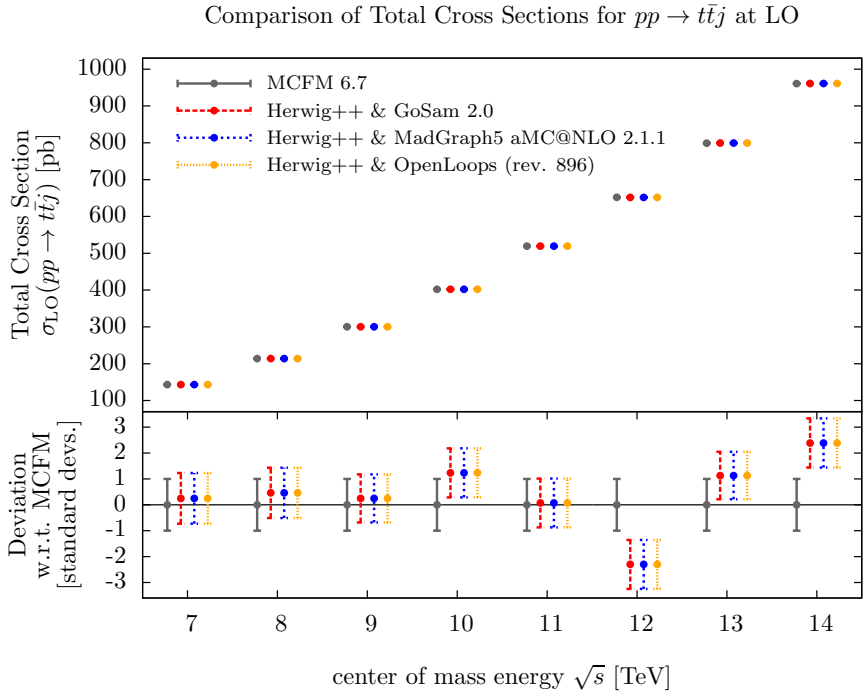

Figure 7.5.: Fixed-order comparison of total cross sections for the process $pp \to t\bar{t}j$ at LO with massless jet constituents $j = \{g, u, \bar{u}, d, \bar{d}, s, \bar{s}, c, \bar{c}, b, \bar{b}\}$ for different center-of-mass energies between MCFM and Herwig++ interfaced to either GoSam, MadGraph or OpenLoops. The error bars indicate the statistical uncertainty on the total cross section and are normalized to the results of the MCFM runs. The relative uncertainty of all the runs is about 0.01%.

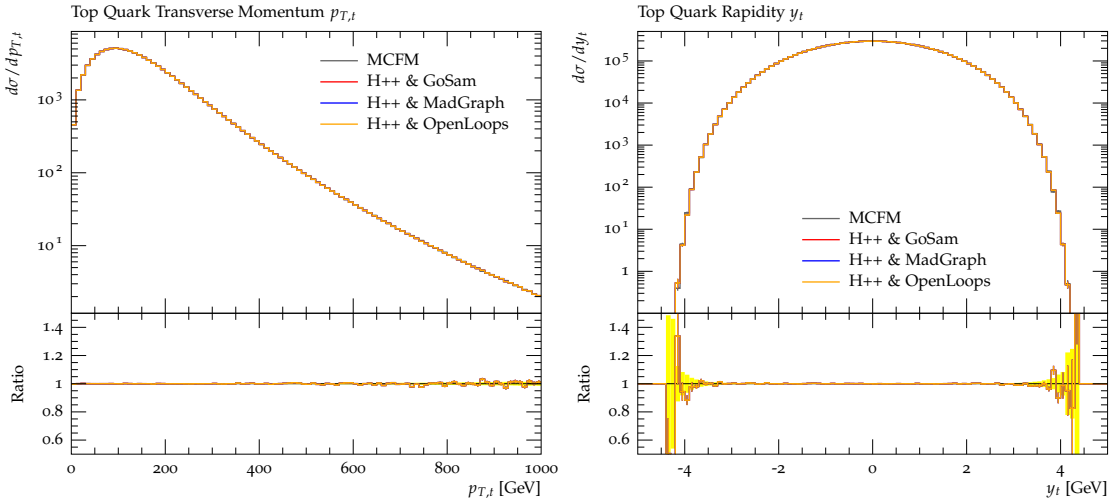

Figure 7.6.: Fixed-order comparison of the transverse momentum and rapidity distributions of the top quark for the process $pp \to t\bar{t}j$ at LO for a center-of-mass energy of 14 TeV. The yellow error bands denote the statistical uncertainty for the results of MCFM.

$s_{ij} = 2p_ip_j = 2(E_iE_j - |\vec{p}_i||\vec{p}_j|\cos\theta_{ij})$ can be used where θ_{ij} denotes the angle between both partons. It vanishes only in the collinear case for massless partons but as mentioned earlier may still become small even in the presence of massive quarks. A standard way to check the correct working of the subtraction is to plot the ratio

$$\frac{\text{subtraction term}}{\text{real-emission matrix element}} \tag{7.1}$$

as a function of either the parton energies E_i or the invariants $\sqrt{s_{ij}}$. For increasingly small values of the energy or the invariant the ratio should obviously tend to unity. In the subtraction plots the subtraction ratios for all phase space points are filled into histograms and the area between the maxima and minima for each bin are drawn. While this method preserves information on which of the two contributions is larger it does not depict much details for ratios closely around unity. Therefore an alternative method based on the relative difference

$$\frac{|\text{subtraction term} - \text{real-emission matrix element}|}{\text{real-emission matrix element}} \tag{7.2}$$

which is symbolically written as $|\mathcal{D} - \mathcal{M}|/\mathcal{M}$ in the subtraction plots was implemented in Herwig++/Matchbox. The absolute value needs to be taken such as to allow plotting on a logarithmic scale. While this does not allow to see which of the two values was larger it resolves much more detail closer to the IR limits. Both types of plots are contrasted in figure 7.7 where the same subtraction data for soft gluon emission is shown in both representations in order to highlight the differences between both types of plots. More subtraction plots will be shown and discussed later on in this section.

In previous work on the massive dipole subtraction algorithm done by Martin Stoll in the course of his diploma thesis [3] electron-positron collisions were considered. Thus, partons only appear in the final state and the FI, IF or II dipoles, which only come into play for hadron collisions, are not yet needed. Therefore, even though a preliminary implementation for massive partons existed it was used and extensively validated for the first time in

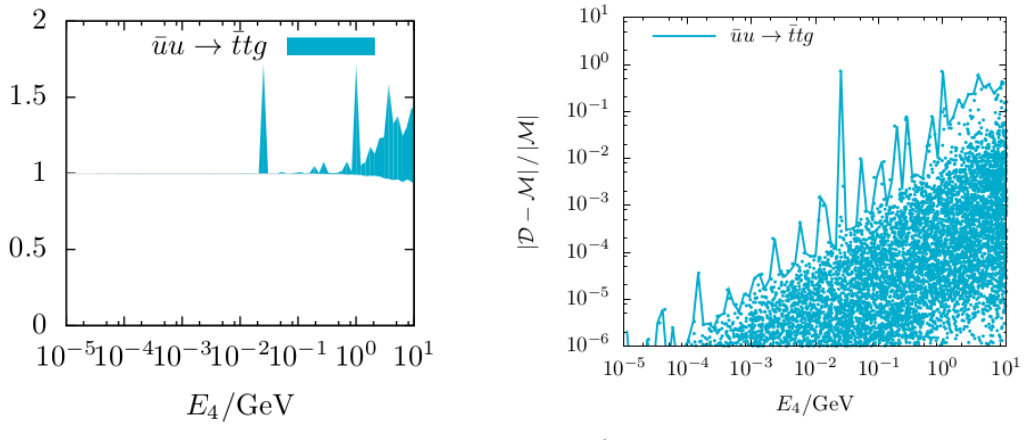

(a) Ratio $\mathcal{D}/\mathcal{M}$ (b) Relative difference $|\mathcal{D}-\mathcal{M}|/\mathcal{M}$

Figure 7.7.: For the subtraction plots either the ratio between the subtraction dipoles and the real-emission matrix element - symbolically denoted by $\mathcal{D}/\mathcal{M}$ in the left-hand panel - can be used or a logarithmic plot of the relative difference between the two - written as $|\mathcal{D}-\mathcal{M}|/\mathcal{M}$ in the right-hand panel. The solid line in the relative difference plot on the right-hand side simply connects the highest data points in each bin. Depicted in both plots is the subtraction for the case of soft gluon emission.

this thesis. In table 7.1 the list of all massive dipoles is given including the dipole name used in Herwig++/Matchbox and for cross-reference also the symbol used in [1, 2, 11]. Since this was the first time all dipoles were put into action, at first the implementation of all of them was checked, debugged and modified at the source code level and also extended to cover top quarks which were treated for the first time in Herwig++/Matchbox. Furthermore, for all massive dipoles - not only the ones participating in $pp \to t\bar{t}$ - example processes were run so as to have sufficient statistics for each contribution. It was extensively checked that all relevant dipoles are selected and no configurations are left out. By means of the subtraction plots the correct limiting behavior was established.

As an example a very small selection of the numerous plots that are created for $pp \to t\bar{t}$ are shown in figure 7.8. Depicted there are a subtraction plot for soft gluon emission on the lower right panel and three different collinear configurations which are described in the caption of the image. As can be seen, the relative difference indeed tends to zero when approaching the IR limit which is exactly the desired behavior. As can be seen from the inclinations of the enveloping solid line or also the bulk of points the convergence roughly occurs linearly in the quantity on the abscissa. This behavior can be understood. For example, the invariant $s_{ij} = 2p_i \cdot p_j$ which appears as $1/s_{ij}$ in the propagator-like factor of equation (2.33) for FF and FI configurations depends on the energy E_i of an emitted gluon i as

$$s_{ij} = 2p_i \cdot p_j = 2E_i \cdot (E_j - |\vec{p_j}| \cos\theta_{ij}) \ . \tag{7.3}$$

Thus, the expansion of the matrix elements and dipoles around the IR limit in terms of E_i is given by

$$\mathcal{M} = m_{-1} \cdot \frac{1}{E_i} + m_0 + m_1 \cdot E_i + \dots \tag{7.4}$$

dipole name	symbol	splitting	present in $pp \to t\bar{t}$
FFMgg	$\boldsymbol{V}_{gg,k}$	$g \to gg$	
FFMqg	$\boldsymbol{V}_{gQ,k}$	$Q \to Qg$	✓
FFMqq	$\boldsymbol{V}_{Q\bar{Q},k}$	$g \to Q\bar{Q}$	
FIMqg	$\boldsymbol{V}^{a}_{gQ}$	$Q \to Qg$	✓
FIMqq	$\boldsymbol{V}^{a}_{Q\bar{Q}}$	$g \to Q\bar{Q}$	
IFMgg	$\boldsymbol{V}^{gg}_{j}$	$g \to gg$	✓
IFMgq	$\boldsymbol{V}^{qq}_{j}$	$q \to gq$	✓
IFMqg	$\boldsymbol{V}^{qg}_{j}$	$q \to qg$	✓
IFMqq	$\boldsymbol{V}^{gq}_{j}$	$g \to q\bar{q}$	✓

Table 7.1.: List of all massive dipoles. Note that there are no massive II dipoles since initial-state particles always have to be massless. For final-state splittings the order of the child partons does not matter but the initial-state splittings were written in such a way that the first child parton always participates in the hard process while the second simply is an outgoing particle.

and

$$\mathcal{D} = d_{-1} \cdot \frac{1}{E_i} + d_0 + d_1 \cdot E_i + \dots \ , \tag{7.5}$$

If the dipoles really approximate the matrix elements in the IR limit, d_{-1} and m_{-1} have to coincide. Thus, it follows that

$$\frac{|\mathcal{D} - \mathcal{M}|}{|\mathcal{M}|} = \frac{|d_0 - m_0 + (d_1 - m_1) \cdot E_i + \dots|}{|m_{-1} \cdot \frac{1}{E_i} + m_0 + \dots|} \xrightarrow{E_i \to 0} \frac{|d_0 - m_0|}{|m_{-1}|} \cdot E_i \ . \tag{7.6}$$

This is exactly what is observed in the subtraction plot for soft gluon emission that is depicted on the lower right panel of figure 7.8. A similar argument can be made for the collinear limit. Convergence of the matrix elements and dipoles was observed in all subtraction plots and for all dipole configurations and in particular, errors were corrected in the massive dipoles that had not been used before such as to achieve a correct subtraction.

7.2.3. Virtual Contributions: Pole Cancellation Checks

When dimensional regularization is used for the IR singularities the m-parton contribution to the NLO correction can be written as

$$\int_m (\mathcal{V} + \mathcal{B} \otimes \boldsymbol{I}) \, \mathrm{d}\Phi_m \tag{7.7}$$

with both the virtual correction $\mathcal{V}$ and the integrated subtraction term $\mathcal{B} \otimes \boldsymbol{I}$ being expansions in $1/\epsilon$. Since the sum of both terms should be finite the contributions coming from both should cancel against each other order by order in $1/\epsilon$ at matrix element level, i.e.

$$\int_m (\mathcal{V} + \mathcal{B} \otimes \boldsymbol{I}) \, \mathrm{d}\Phi_m = \int_m \left(0 \cdot \frac{1}{\epsilon^2} + 0 \cdot \frac{1}{\epsilon} + \text{finite terms} \right) \mathrm{d}\Phi_m \tag{7.8}$$

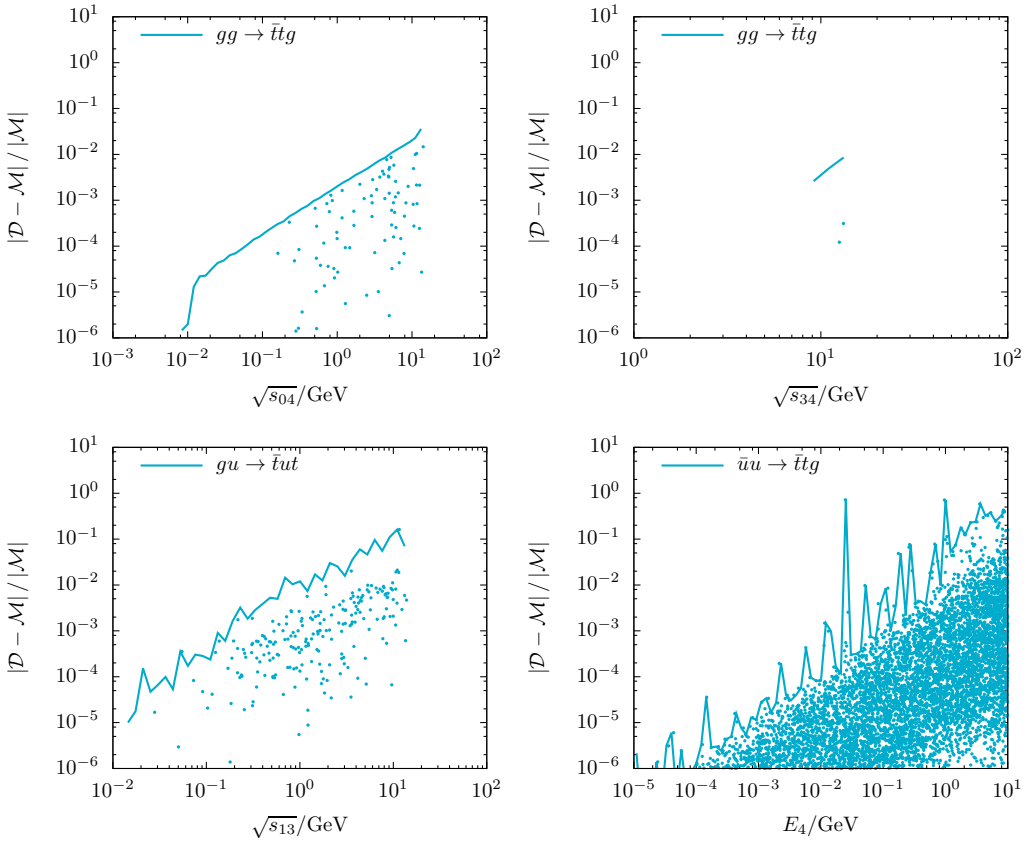

Figure 7.8.: Small selection of the subtraction plots obtained in the real-emission contribution to $pp \to t\bar{t}$. The indices refer to the different particles of the respective process and begin with the id 0 for the first parton. In the panel on the upper left the subtraction plot for a collinear configuration of the final-state gluon and the first of the incoming gluons is depicted. In the lower left panel the outgoing u-quark is collinear to the incoming u-quark. The panel on the upper right shows the collinear emission of a gluon by the top quark and on the lower right the subtraction plot for soft gluon emission is shown. Apart from the desired convergent behavior one can see the relative distribution of the various limits. E.g. the soft gluon emission which is depicted in the lower right plot occurs much more often than the collinear limits shown in the other plots.

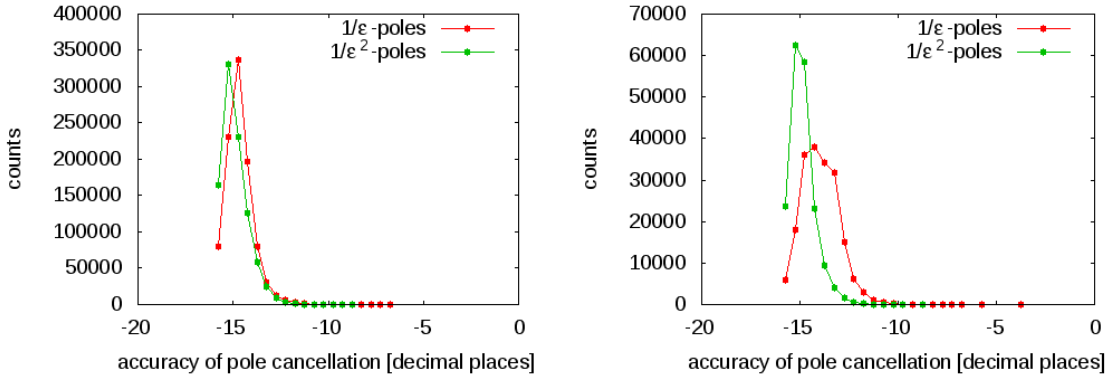

(a) pole cancellation in the subprocess $gg \to t\bar{t}$ (b) pole cancellation in the subprocess $u\bar{u} \to t\bar{t}$

Figure 7.9.: Selection of the pole cancellation plots obtained for the process $pp \to t\bar{t}$. The pole coefficients of both the $1/\epsilon$ poles as well as the $1/\epsilon^2$ poles agree on at least 10 to 11 decimal places.

To explicitly check the cancellation of the poles one can compare the coefficients for the respective singularities from the virtual contribution and the integrated subtraction term and check how good they agree. This can be done by means of the quantity

$$\log\left(\left|1 - \frac{|\text{pole coefficient from insertion operator } \boldsymbol{I}|}{|\text{pole coefficient from virtual contribution matrix element } \mathcal{V}|}\right|\right) \tag{7.9}$$

for both the $1/\epsilon$ and the $1/\epsilon^2$ poles separately. The more precisely the coefficients from both terms agree the more negative this quantity gets. Some exemplary plots are shown in figure 7.9 from which it can be seen that the pole coefficients obtained from the virtual contribution matrix elements $\mathcal{V}$ calculated by the OLPs and the insertion operator $\boldsymbol{I}$ calculated in Herwig++/Matchbox agree on at least 10 to 11 digits. In many cases even up to 14 or 15 decimal places coincide which practically corresponds to the resolution of double precision floating point numbers that are used in the calculations. More pole cancellation plots are given in appendix D.

Even though all subtraction terms were validated separately the integrated counterparts of the dipoles FFMgg, FFMqq and FIMqq cannot be checked in the process $pp \to t\bar{t}$. In order to establish the correct working of those contributions it will be necessary to investigate processes such as $pp \to t\bar{t}j$ with massless jet constituents and $pp \to t\bar{t}b\bar{b}$ with massive b-quarks.

7.2.4. Full Next-to-leading Order Comparison

For the full NLO calculation the CT10NLO parton distributions were used and a strong coupling with

$$\Lambda_{\text{QCD}} = 203.8672\text{MeV} \tag{7.10}$$

was set in Herwig++. The value of the strong coupling at the fixed scale of $\mu_F = \mu_R = 80$ GeV was

$$\alpha_s^{(\text{MCFM})}(\mu_R^2) = \alpha_s^{(\text{Herwig++})}(\mu_R^2) = 0.12037772\ .$$

No jet cuts were used. Apart from that everything else was just the same as in the leading order comparisons. Again the runs were adjusted such as to achieve a statistical uncertainty of 0.01% or less on the total cross sections.

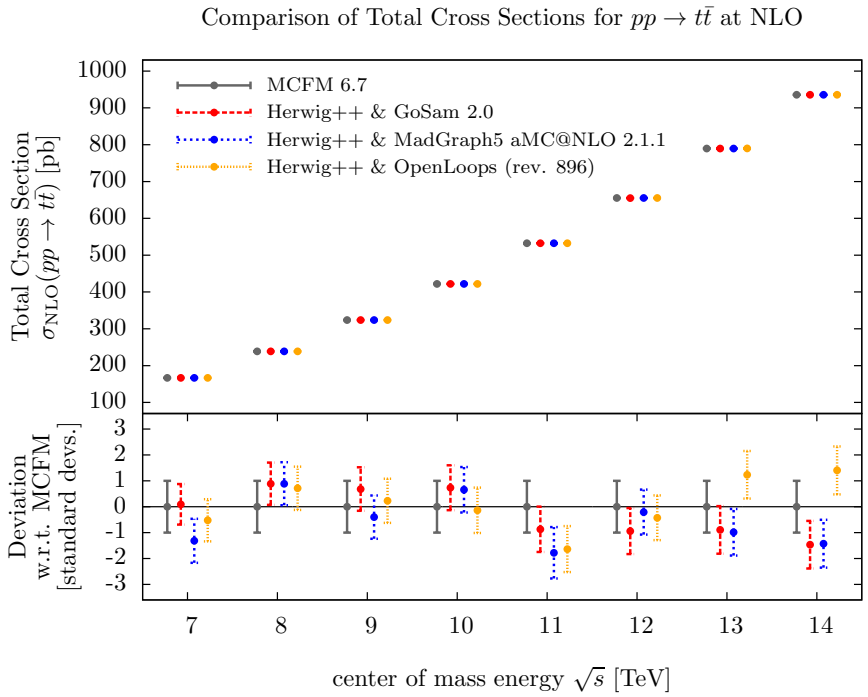

Figure 7.10.: Fixed-order comparison of total cross sections for the process $pp \to t\bar{t}$ at NLO with massless jet constituents $j = \{g, u, \bar{u}, d, \bar{d}, s, \bar{s}, c, \bar{c}, b, \bar{b}\}$ for different center-of-mass energies between MCFM and Herwig++ interfaced to either GoSam, MadGraph or OpenLoops. The error bars indicate the statistical uncertainty on the total cross section and are normalized to the results of the MCFM runs. The relative uncertainty of all the runs is about 0.01% or less.

The benchmark results for the total NLO cross sections are depicted in figure 7.10 and the differential cross sections in figure 7.11. Just as for the tree-level benchmarks, MCFM is compared to Herwig++ which is interfaced to the three matrix element providers GoSam, MadGraph and OpenLoops. In this comparison both the tree-level as well as the virtual contributions were taken from the same matrix element provider, i.e. the matrix elements from the different providers were not mixed. Again, good agreement is found for the total cross sections. In contrast to the LO comparisons the results for Herwig++ and the matrix element providers do not coincide exactly anymore which probably is due to the different techniques for the calculation and evaluation of the one-loop amplitudes used by the matrix element providers. Very good agreement is also found for the differential cross sections.

7.3. Matching to the QTilde Shower

As explained in section 3.3 the purpose of matching is to preserve the correct NLO-level prediction for observables when a parton shower is applied to a fixed-order calculation. Moreover, it is to provide a transition between the fixed-order prediction which is only valid for hard interactions and the parton shower prediction that is restricted to the regions approaching the infrared limits.

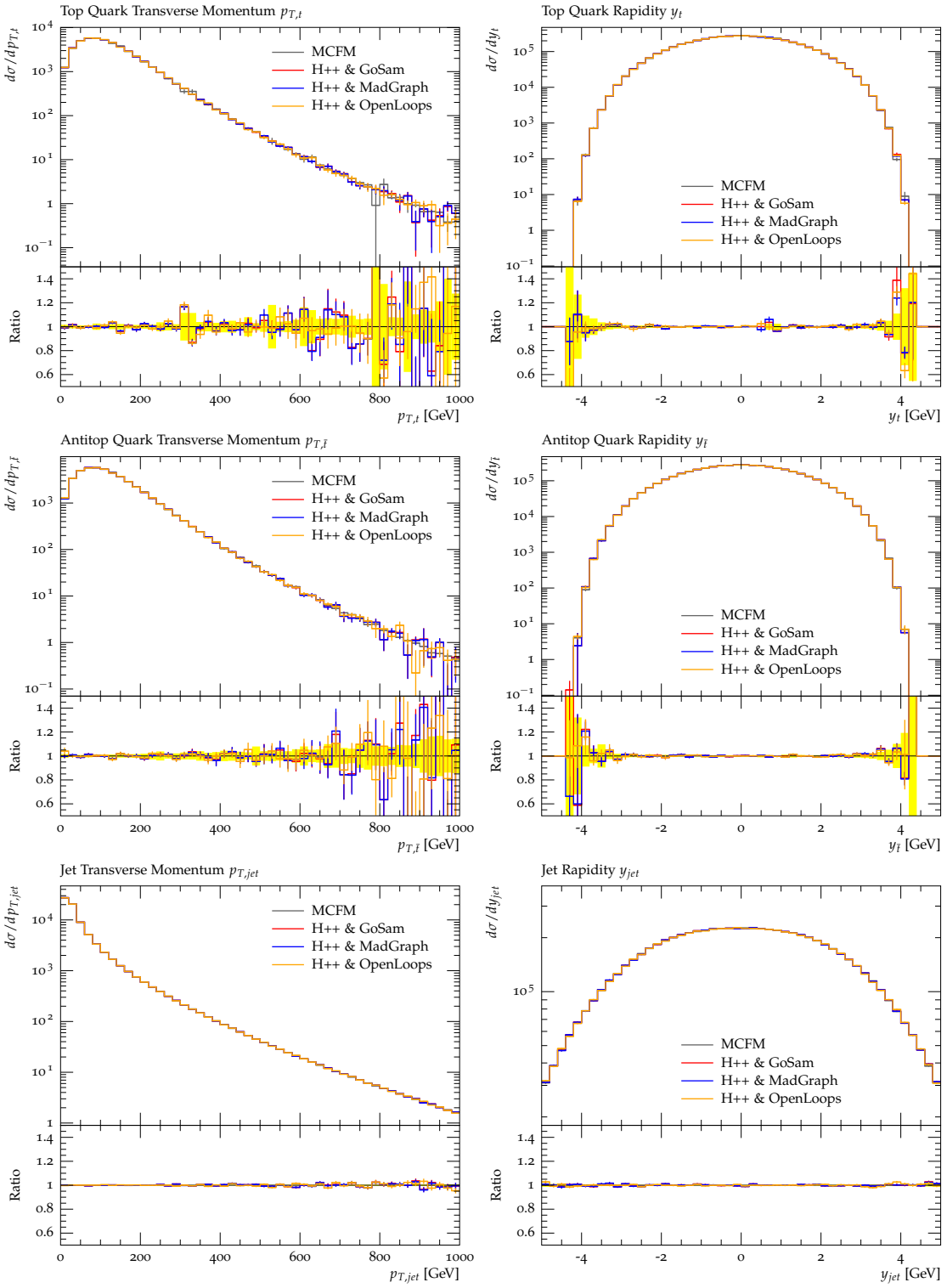

Figure 7.11.: Fixed-order comparison of the transverse momentum and rapidity distributions of the top quark, the anti-top quark and the jet parton for the process $pp \to t\bar{t}$ at NLO for a center-of-mass energy of 14 TeV. The yellow error bands denote the statistical uncertainty for the results of MCFM.

Scale	LO	LO + QTS
	(total cross section ± statistical uncertainty ± scale uncertainty)	
TopMassScale	$395.03\,\text{pb} \pm 0.06\,\text{pb}^{+23.1\%}_{-17.8\%}$	$394.93\,\text{pb} \pm 0.06\,\text{pb}^{+23.1\%}_{-17.8\%}$
TopMTScale	$460.59\,\text{pb} \pm 0.07\,\text{pb}^{+24.9\%}_{-18.6\%}$	$460.57\,\text{pb} \pm 0.07\,\text{pb}^{+24.9\%}_{-15.6\%}$
TopMinMTScale	$512.72\,\text{pb} \pm 0.08\,\text{pb}^{+26.9\%}_{-19.1\%}$	$512.74\,\text{pb} \pm 0.08\,\text{pb}^{+26.9\%}_{-19.1\%}$

Table 7.2.: Comparison of total cross sections in the process $pp \to t\bar{t}$ at 14 TeV for fixed-order LO and LO with the qtilde shower. Both the statistical and the scale uncertainties are given, the latter of which are estimated from simultaneous variations of the factorization, renormalization and shower start scale by factors of 0.5 and 2.

The correct working of the matching procedure was evaluated with the example process $pp \to t\bar{t}$ for which the fixed-order NLO calculation was combined with the angular-ordered qtilde shower by means of the MC@NLO-like prescription given in equation (3.38).

For the calculation, tree-level amplitudes from MadGraph were combined with one-loop matrix elements from GoSam using Matchbox's hybrid amplitude mechanism. For all simulations 50 jobs with 400000 events apiece were run. The CT10 parton distributions were used and a value of $\alpha(m_Z = 91.188\text{GeV}) = 0.118$ was set in the running coupling `MatchboxNLOAlphaS`. Runs were made for three different scale choices for the factorization and renormalization scales:

- TopMassScale
$$\mu^2_{m_{t\bar{t}}} = (p_t + p_{\bar{t}})^2$$
- TopMTScale
$$\mu^2_{m_{T,t\bar{t}}} = \sum_{i=t,\bar{t}} \left(m_i^2 + p_{T,i}^2\right)$$
- TopMinMTScale
$$\mu^2_{\min_{t\bar{t}}\{m_T\}} = \min_{i=t,\bar{t}} \left(m_i^2 + p_{T,i}^2\right) \ .$$

The same scales were also used as the start scale of the parton shower. In the case of the qtilde shower it is possible to so via the commands

```
set /Herwig/Shower/Evolver:HardVetoScaleSource Read
```

In contrast, the default start scale of the parton shower is given by

$$\mu^2_{\text{PS}} = \min_{i=t,\bar{t},j} \left(m_i^2 + p_{T,i}^2\right) \ , \tag{7.11}$$

which also takes into account the transverse mass of the additional parton present in H-events. In order to assess the scale uncertainties, variations of the renormalization, factorization and shower start scales were made. All of the aforementioned scales were varied up and down simultaneously by a factor of 2.

The results for the total cross sections of the leading order runs are summarized in table 7.2 from which it can be seen that just as expected the total cross sections are not modified by

Scale	NLO (total cross section ± statistical uncertainty ± scale uncertainty)	NLO + QTS (total cross section ± statistical uncertainty ± scale uncertainty)
TopMassScale	$702.16\,\text{pb} \pm 0.17\,\text{pb}^{+11.6\%}_{-11.0\%}$	$700.43\,\text{pb} \pm 1.58\,\text{pb}^{+12.0\%}_{-11.0\%}$
TopMTScale	$759.99\,\text{pb} \pm 0.20\,\text{pb}^{+11.1\%}_{-10.5\%}$	$760.82\ \text{pb} \pm 1.97\,\text{pb}^{+11.4\%}_{-10.6\%}$
TopMinMTScale	$820.80\,\text{pb} \pm 0.21\,\text{pb}^{+12.8\%}_{-10.6\%}$	$820.35\ \text{pb} \pm 2.27\,\text{pb}^{+13.1\%}_{-10.9\%}$

Table 7.3.: Comparison of total cross sections in the process $pp \to t\bar{t}$ at 14 TeV for fixed-order NLO and NLO matched to the qtilde shower. Both the statistical and the scale uncertainties are given, the latter of which are estimated from simultaneous variations of the factorization, renormalization and shower start scale by factors of 0.5 and 2.

the parton shower. This is just the consequence of the parton shower's unitarity. Likewise, table 7.3 summarizes the results for the NLO cross sections where again it can be seen that the fixed-order (NLO) and the matched (NLO+QTS) calculations agree within the statistical uncertainty. In both tables also the scale uncertainties are given. They are estimated from simultaneous variations of the factorization, the renormalization and also the shower start scale by factors of 0.5 and 2. The latter characterizes the hardest emission that can be generated by the shower. As can be seen from the values in the table, the scale uncertainties are reduced to approximately 10...13% at NLO from around 19...27% at LO.

From a whole range of observables the transverse momentum $p_{T,t\bar{t}}$ of the top quark pair was selected for the following discussion since - as already mentioned in section 3.3 - it very clearly reveals the effects of the matching. It vanishes at leading order and thus non-zero values for $p_{T,t\bar{t}}$ in an LO+PS calculation are entirely due to the parton shower. Since the parton shower approximates the IR limits, its prediction is reliable only for low transverse momenta. In contrast, at fixed-order NLO the top-antitop quark pair acquires a transverse momentum as it recoils against a parton generated by the real-emission contribution which should give a good description for a hard jet and thus high transverse momenta $p_{T,t\bar{t}}$. This is exactly what can be seen in figure 7.12. On the other hand, the fixed-order NLO prediction diverges for increasingly small transverse momenta and jumps to negative values that are caused by the virtual corrections. The LO plus parton-shower calculation gives a finite result for low transverse momenta but produces too few high-$p_{t\bar{t}}$ emissions. The damping that is observed in the region of low transverse momentum is known as the *Sudakov suppression* or *Sudakov damping* and the maximum at around 15 GeV is usually referred to as the *Sudakov peak*. Both are a result of the parton shower adding terms of the form

$$\int \mathrm{d}\Phi_m \mathcal{B} \int_{\mu^2_{\mathrm{IR}}}^{Q^2} \mathrm{d}\mathcal{P}(q^2)[O_{m+1} - O_m] \ , \tag{7.12}$$

which e.g. appears in equation (3.28). Such terms subtract a contribution from the m-parton bin of the observable and add it back to the $m+1$-parton bin. This way, the differential cross section is pushed into configurations of the $t\bar{t}$-quark pair with higher transverse momenta by parton shower emissions. As can be seen in figure 7.12, the matched calculation smoothly interpolates between both limits - it approaches the fixed-order NLO prediction for high values of $p_{T,t\bar{t}}$ and the parton shower prediction for small transverse momenta. However, since the total cross section of the fixed-order NLO calculation is preserved, the matched distribution overshoots the other two predictions in the transition

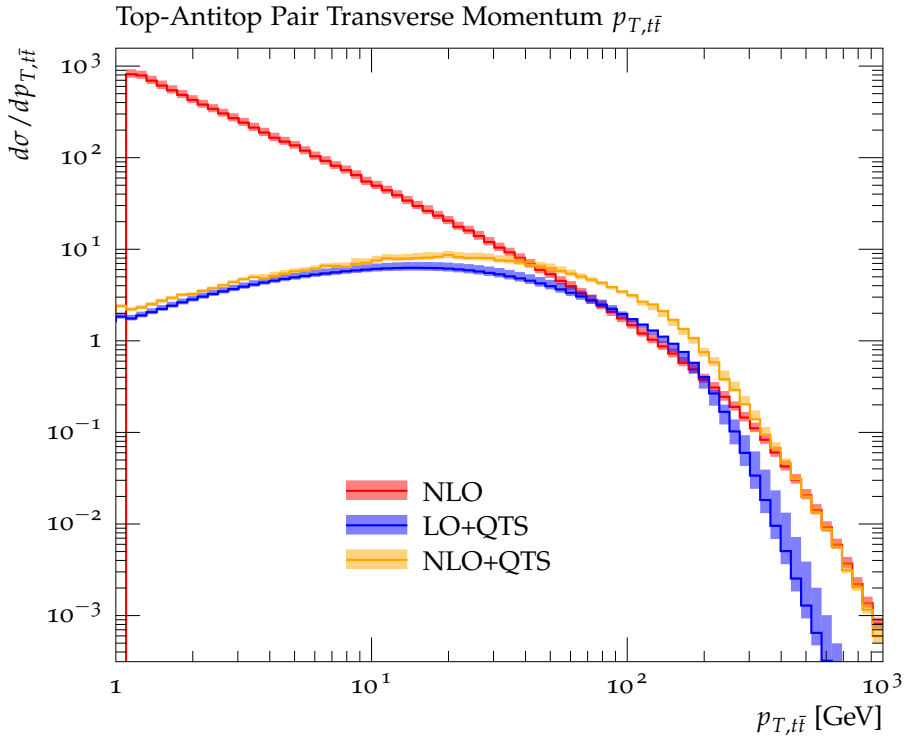

Figure 7.12.: Transverse momentum distribution of the $t\bar{t}$-pair for $pp \to t\bar{t}$ at NLO matched to the qtilde shower. The TopMinMTScale is used for the factorization, renormalization and shower start scales. The error bands denote the scale uncertainties as estimated by simultaneous variations of the factorization, renormalization and shower start scales by factors of 2 and 0.5.

region. Let it be emphasized that this is no shortcoming of the matching prescription but rather a necessary consequence of the conservation of the total cross section. When looking at the bands that indicate the scale uncertainties it can be seen that the parton shower prediction has a narrow band for low transverse momenta which widens substantially towards larger values of $p_{T,t\bar{t}}$ where the prediction becomes increasingly more unreliable. For the fixed-order NLO calculation the scale uncertainty grows in proportion to the value of the differential cross section and therefore appears to have a constant thickness when a logarithmic y-axis is used. The matched distribution, in contrast, has a narrow band throughout.

Similar results are obtained for the TopMassScale and the TopMTScale which are depicted in figure 7.13. For the case of the TopMassScale, however, the curve for the matched cross section approaches the fixed-order result for higher values of $p_{T,t\bar{t}} \approx 800...900\,\text{GeV}$ in contrast to $p_{T,t\bar{t}} \approx 350...400\,\text{GeV}$ for the TopMinMTScale and the TopMTScale. For low transverse momenta, the matched prediction for the TopMassScale lies slightly more above the LO+PS curve than for the other two scales. The result, that the matched distributions do not exactly coincide with the LO+PS predictions is due to the fact that the parton shower only approximates but not fully reproduces the non-emission of the virtual contribution. Differences are therefore to be expected in this region.

If instead of from the hard process scale $Q = \mu_F = \mu_R$ the parton shower is started from its default start scale μ_{PS}, it was found that the matched prediction of the transverse momentum spectrum of the top quark pair drops to negative values around 12 GeV and

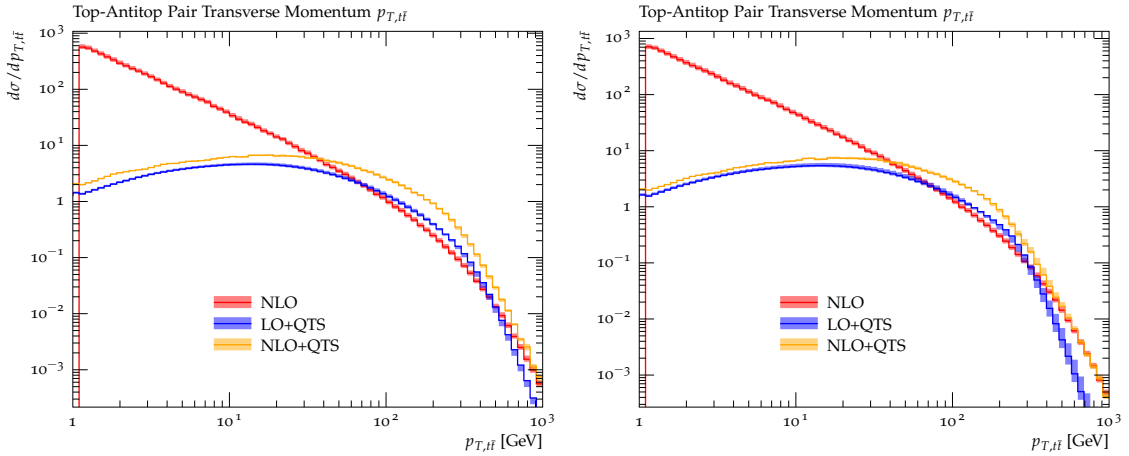

(a) TopMassScale (b) TopMTScale

Figure 7.13.: Transverse momentum distribution of the $t\bar{t}$-pair for $pp \to t\bar{t}$ at NLO matched to the qtilde shower. The TopMassScale and the TopMTScale are used for the factorization, renormalization and shower start scales. The error bands denote the scale uncertainties as estimated by simultaneous variations of the factorization, renormalization and shower start scales by factors of 2 and 0.5.

therefore does not approach the LO+PS prediction for small transverse momenta. This can be seen in figure 7.14 where the TopMinMTScale is used as the factorization and renormalization scale and where the different contributions to the matched NLO cross section for the case of using the hard process scale Q as the shower start scale in the left panel is contrasted to the default start scale μ_{PS} which is shown in the right panel. The contributions shown for both cases are the S-events with one emission by the parton shower (dashed red curve), the S-events with the full parton shower added on top (solid red curve), the H-events with no parton shower emission (solid blue curve), the H-events with the full parton shower added on top (solid blue curve) and finally the matched prediction with the full parton shower (solid yellow curve). First of all, it can be seen that, just as expected, the S- and H-events with the full parton shower add up to the matched prediction. The curves for the S-events are identical for both start scales since as can be seen from equation 7.11 the default shower start scale and the TopMinMTScale give the same results in the absence of an emission. Also, the curves corresponding to the H-events with no parton shower emissions coincide. This is because, if the default shower start scale is used, in the matching subtraction for the H-events the upper phase space boundary Q is calculated from a phase space configuration where the emission was clustered back to either the top or the antitop quark. It therefore coincides again with the TopMinMTScale. However, one can see the differences for the H-events with the full parton shower: In case the default shower start scale is used, the parton shower only creates few emissions and as a consequence, the resulting curve is not too different from the one corresponding to the H-events with no shower emission at all. In particular, with the default shower start scale the parton shower cannot create emissions harder than the possibly low transverse momentum of the jet stemming from the hard process. Therefore, the showered curve (solid blue line) practically follows the unshowered prediction (dashed blue line) for transverse momenta of more than approximately 8 GeV. In contrast, if the hard process scale is used, the shower radiates much more, thereby pushing more weight to higher transverse momenta. These differences are due to the presence of an emission stemming from the hard

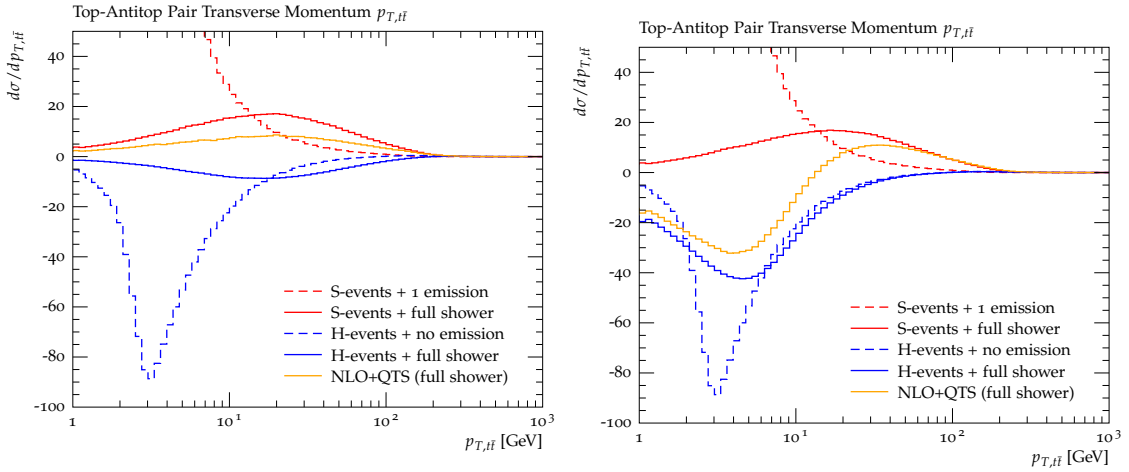

(a) Shower is started from the hard process scale $\mu_F = \mu_R = \mu_{\min_{t\bar{t}}\{m_T\}}$.

(b) Default shower start scale μ_{PS}.

Figure 7.14.: Comparison of the contributions of S- and H-events. For the hard process the TopMinMTScale $\mu_{\min_{t\bar{t}}\{m_T\}}$ is used. In the left panel the shower is started from the hard process scale whereas in the right panel the default shower start scale μ_{PS} is used. Depicted in both plots are the contributions of the S-events with either only one emission added by the parton shower (dashed red curve) or the full parton shower (solid red curve) and the H-events with either no parton shower emissions (dashed blue curve) or the full parton shower (solid blue curve). The predictions for the S-events with the full parton shower and the H-events with the full parton shower add up to the matched prediction (yellow curve).

process generation for the H-events. Since all jet constituents are massless, the emission's transverse mass is entirely due to its transverse momentum which may be soft. Therefore, the default shower start scale, which for the generation of shower emissions is calculated from unclustered configurations, takes values that are much smaller than those calculated by the TopMinMTScale, where the jet constituent from the H-events is not considered. The latter returns at least the square of the top mass whereas the default scale reaches down to much lower values. These low values for the default shower start scale restrict the parton shower to only do a few emissions which results in the observed behavior. In contrast, for the TopMinMTScale the shower is started at a substantially higher scale and can therefore radiate more. Similar results for the TopMassScale are shown in figure 7.15.

In conclusion, the correct working of the matching procedure when using the hard process scale as the parton shower start scale is established.

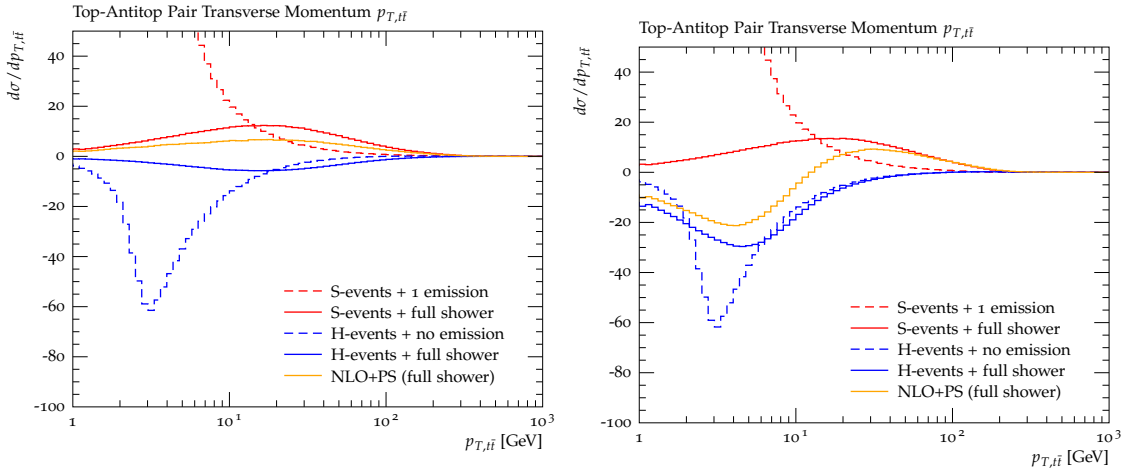

(a) Shower is started from the hard process scale $\mu_F = \mu_R = \mu_{m_{t\bar{t}}}$.

(b) Default shower start scale μ_{PS}.

Figure 7.15.: Comparison of the contributions of S- and H-events. For the hard process the TopMassScale $\mu_{m_{t\bar{t}}}$ is used. See figure 7.14 for a description of the depicted curves.

Chapter 8

Conclusion and Outlook

The goal of this thesis was to extend the automation of NLO calculations with massive partons in the general-purpose event generator Herwig++ to the case of hadron colliders and validate it using the example process $pp \to t\bar{t}$. In Herwig++/Matchbox the Catani-Seymour algorithm, which is based on the dipole picture of QCD, is used for the subtraction of IR singularities for processes with massless partons. A preliminary implementation of the subtraction algorithm for massive partons was done by Martin Stoll and validated for the process $e^+e^- \to b\bar{b}$ with massive b-quarks [3]. This, however, only makes use of a subset of all terms appearing in the algorithm, namely configurations where a final-state parton splits and recoils against a final-state spectator parton, and the insertion operator $\boldsymbol{I}$.

In this thesis, the massive version of the subtraction algorithm was used for proton-proton collisions for the first time. Not only the subtraction terms that appear in top quark pair production but all subtraction dipoles contributing in the presence of massive partons were individually investigated both at the source code level as well as in example processes. Some errors were found, corrected and, as a result, the desired approximation in the IR limit of the real-emission matrix elements by the subtraction terms could be established. The correct cancellation of infrared singularities between the virtual contribution and the integrated subtraction terms was demonstrated and the coefficients of the ϵ-poles from both contributions were found to agree on at least 10 decimal places. The implementation of the insertion operators $\boldsymbol{I}$, $\boldsymbol{P}$ and $\boldsymbol{K}$, which contain the integrated counterparts of the subtraction terms, was found to not consider complications arising from modifications in the implementation of the NLO calculations in Herwig++/Matchbox with respect to the form the unmodified Catani-Seymour algorithm is based on. After accounting for these modifications very good agreement with MCFM 6.7 was found for predictions for the total cross section and differential distributions. In all comparisons the statistical uncertainties were brought down such that agreement with MCFM was established on the level of 0.01% for the calculated total cross sections.

In order to enable the generation of meaningful statistics at reasonable time scales for NLO and parton shower calculations, the tool Herwig-Parallel was developed and the

analysis toolkit Rivet was modified to make possible running Herwig++ on computing clusters and combine the results and histogrammed distributions from the different jobs afterwards. Herwig-Parallel may possibly be included in future releases of Herwig++.

Having at hand the subtraction algorithm for massive partons, the second goal of this thesis was to validate the matching of the angular-ordered parton shower in Herwig++ for the process $pp \to t\bar{t}$. To this end the transverse momentum of the top quark pair was studied. This observable is very sensitive to the matching of fixed-order NLO and parton shower calculations because the region of high transverse momentum probes hard jet emissions which are described by the real-emission matrix elements while for low transverse momenta the resummation done by the parton shower is needed to obtain a sensible result. First of all, as shown in section 7.3 the total cross sections for fixed-order and showered runs agree both for LO and for NLO which was expected due to the unitarity of the parton shower. Secondly, the correct working of the matching could be found in the $p_{T,t\bar{t}}$-distribution when using the factorization and renormalization scale of the hard process as the start scale for the parton shower. As can be seen from figures 7.12 and 7.13 the matching results in a smooth interpolation between the real-emission matrix elements which are approached for high values of $p_{T,t\bar{t}}$ and the parton shower result for low transverse momenta. The matched prediction, however, differs slightly from the LO+PS curve for low transverse momenta because it includes the full virtual contribution of the NLO cross section which is only approximated by the parton shower. Since the total cross section is conserved when applying the parton shower to the fixed-order NLO calculation, the matched prediction rises above the fixed-order NLO and LO+PS curves for intermediate transverse momenta of around 100 GeV. This is no shortcoming of the matching procedure but a consequence of the NLO cross section being larger than the LO cross section. If the default shower start scale is used, the matched distribution of the transverse top quark pair momenta drops to negative values for small transverse momenta. This finding will make necessary further contemplation of the preferred default shower start scale.

In conclusion, the automation of NLO calculations in Herwig++ was extended to include processes with massive partons at hadron colliders and validated with the example process $pp \to t\bar{t}$. For the same process, the matching to the angular-ordered qtilde shower was validated and the correct working of the matching was found when the hard process scale is used as the shower start scale.

Bibliography

[1] S. Catani and M. Seymour, *The Dipole formalism for the calculation of QCD jet cross-sections at next-to-leading order*. Phys.Lett. **B378** (1996) 287–301, arXiv:hep-ph/9602277 [hep-ph].

[2] S. Catani and M. Seymour, *A General algorithm for calculating jet cross-sections in NLO QCD*. Nucl.Phys. **B485** (1997) 291–419, arXiv:hep-ph/9605323 [hep-ph].

[3] M. Stoll, *Parton Shower for Massive Fermions*. Diploma thesis, Karlsruhe Institute of Technology (KIT), 2012. http://www.itp.kit.edu/prep/diploma/PSFiles/Diplom_Stoll.pdf.

[4] R. K. Ellis, W. J. Stirling, and B. Webber, *QCD and collider physics*. Camb.Monogr.Part.Phys.Nucl.Phys.Cosmol. **8** (1996) 1–435.

[5] M. Böhm, A. Denner, and H. Joos, *Gauge Theories of the Strong and Electroweak Interaction*. Vieweg+Teubner Verlag, 3rd ed., 2001.

[6] M. E. Peskin and D. V. Schroeder, *An introduction to quantum field theory*. Addison-Wesley, 4th ed., 1997.

[7] T. Kinoshita, *Mass Singularities of Feynman Amplitudes*. Journal of Mathematical Physics **3** (1962) no. 4, 650–677. http://scitation.aip.org/content/aip/journal/jmp/3/4/10.1063/1.1724268.

[8] T. D. Lee and M. Nauenberg, *Degenerate Systems and Mass Singularities*. Phys. Rev. **133** 6B (1964) B1549–B1562. http://link.aps.org/doi/10.1103/PhysRev.133.B1549.

[9] G. P. Salam, *Towards Jetography*. Eur.Phys.J. **C67** (2010) 637–686, arXiv:0906.1833 [hep-ph].

[10] Z. Kunszt and D. E. Soper, *Calculation of jet cross sections in hadron collisions at order α_s^3*. Phys. Rev. D **46** 1 (1992) 192–221. http://link.aps.org/doi/10.1103/PhysRevD.46.192.

[11] S. Catani, S. Dittmaier, M. H. Seymour, and Z. Trócsányi, *The Dipole formalism for next-to-leading order QCD calculations with massive partons*. Nucl.Phys. **B627** (2002) 189–265, arXiv:hep-ph/0201036 [hep-ph].

[12] J. C. Collins, D. E. Soper, and G. F. Sterman, *Factorization of Hard Processes in QCD*. Adv.Ser.Direct.High Energy Phys. **5** (1988) 1–91, arXiv:hep-ph/0409313 [hep-ph].

[13] The CMS Collaboration, S. Chatrchyan *et al.*, *Measurement of jet multiplicity distributions in* $\mathrm{t\bar{t}}$ *production in pp collisions at* $\sqrt{s} = 7$ *TeV*. Eur.Phys.J. **C74** (2014) no. 8, 3014, arXiv:1404.3171 [hep-ex].

[14] S. Gieseke, *Simulation of jets at colliders*. Progress in Particle and Nuclear Physics **72** (2013) no. 0, 155 – 205. http://www.sciencedirect.com/science/article/pii/S014664101300029X.

[15] A. Buckley, J. Butterworth, S. Gieseke, D. Grellscheid, S. Hoche, *et al.*, *General-purpose event generators for LHC physics*. Phys.Rept. **504** (2011) 145–233, arXiv:1101.2599 [hep-ph].

[16] Y. L. Dokshitzer, *Calculation of the Structure Functions for Deep Inelastic Scattering and e+ e- Annihilation by Perturbation Theory in Quantum Chromodynamics.* Sov.Phys.JETP **46** (1977) 641–653.

[17] V. Gribov and L. Lipatov, *Deep inelastic e p scattering in perturbation theory.* Sov.J.Nucl.Phys. **15** (1972) 438–450.

[18] G. Altarelli and G. Parisi, *Asymptotic Freedom in Parton Language*. Nucl.Phys. **B126** (1977) 298.

[19] P. Skands, *Introduction to QCD*. arXiv:1207.2389 [hep-ph].

[20] S. Plätzer and M. Sjödahl, *The Sudakov Veto Algorithm Reloaded*. Eur.Phys.J.Plus **127** (2012) 26, arXiv:1108.6180 [hep-ph].

[21] T. Sjöstrand, S. Mrenna, and P. Z. Skands, *PYTHIA 6.4 Physics and Manual*. JHEP **0605** (2006) 026, arXiv:hep-ph/0603175 [hep-ph].

[22] S. Plätzer, *Parton Showers and Radiative Corrections in QCD*. PhD thesis, Karlsruhe Institute of Technology (KIT), 2010.

[23] S. Frixione and B. R. Webber, *Matching NLO QCD computations and parton shower simulations*. JHEP **0206** (2002) 029, arXiv:hep-ph/0204244 [hep-ph].

[24] S. Frixione, P. Nason, and B. R. Webber, *Matching NLO QCD and parton showers in heavy flavor production*. JHEP **0308** (2003) 007, arXiv:hep-ph/0305252 [hep-ph].

[25] S. Frixione and B. R. Webber, *The MC and NLO 3.4 Event Generator*. arXiv:0812.0770 [hep-ph].

[26] S. Frixione, Z. Kunszt, and A. Signer, *Three jet cross-sections to next-to-leading order*. Nucl.Phys. **B467** (1996) 399–442, arXiv:hep-ph/9512328 [hep-ph].

[27] S. Frixione, *A General approach to jet cross-sections in QCD*. Nucl.Phys. **B507** (1997) 295–314, arXiv:hep-ph/9706545 [hep-ph].

[28] S. Frixione, P. Nason, and C. Oleari, *Matching NLO QCD computations with Parton Shower simulations: the POWHEG method*. JHEP **0711** (2007) 070, arXiv:0709.2092 [hep-ph].

[29] http://rivet.hepforge.org/svn/contrib/aidamerge.

[30] http://geant4.web.cern.ch/geant4/.

[31] The ATLAS Collaboration, G. Aad *et al.*, *Observation of a new particle in the search for the Standard Model Higgs boson with the ATLAS detector at the LHC*. Phys.Lett. **B716** (2012) 1–29, arXiv:1207.7214 [hep-ex].

[32] The CMS Collaboration, S. Chatrchyan *et al.*, *Observation of a new boson at a mass of 125 GeV with the CMS experiment at the LHC*. Phys.Lett. **B716** (2012) 30–61, arXiv:1207.7235 [hep-ex].

[33] T. Binoth, F. Boudjema, G. Dissertori, A. Lazopoulos, A. Denner, *et al.*, *A Proposal for a standard interface between Monte Carlo tools and one-loop programs*. Comput.Phys.Commun. **181** (2010) 1612–1622, arXiv:1001.1307 [hep-ph].

[34] S. Alioli, S. Badger, J. Bellm, B. Biedermann, F. Boudjema, *et al.*, *Update of the Binoth Les Houches Accord for a standard interface between Monte Carlo tools and one-loop programs*. Comput.Phys.Commun. **185** (2014) 560–571, arXiv:1308.3462 [hep-ph].

[35] http://gosam.hepforge.org/.

[36] G. Cullen, H. van Deurzen, N. Greiner, G. Heinrich, G. Luisoni, *et al.*, *GOSAM-2.0: a tool for automated one-loop calculations within the Standard Model and beyond*. Eur.Phys.J. **C74** (2014) no. 8, 3001, arXiv:1404.7096 [hep-ph].

[37] G. Cullen, N. Greiner, G. Heinrich, G. Luisoni, P. Mastrolia, *et al.*, *Automated One-Loop Calculations with GoSam*. Eur.Phys.J. **C72** (2012) 1889, arXiv:1111.2034 [hep-ph].

[38] http://hjets.hepforge.org/.

[39] F. Campanario, T. M. Figy, S. Plätzer, and M. Sjödahl, *Electroweak Higgs Boson Plus Three Jet Production at Next-to-Leading-Order QCD*. Phys.Rev.Lett. **111** (2013) no. 21, 211802, arXiv:1308.2932 [hep-ph].

[40] https://launchpad.net/mg5amcnlo.

[41] F. Cascioli, J. Lindert, P. Maierhöfer, and S. Pozzorini, http://openloops.hepforge.org/.

[42] F. Cascioli, P. Maierhofer, and S. Pozzorini, *Scattering Amplitudes with Open Loops*. Phys.Rev.Lett. **108** (2012) 111601, arXiv:1111.5206 [hep-ph].

[43] G. Ossola, C. G. Papadopoulos, and R. Pittau, *CutTools: A Program implementing the OPP reduction method to compute one-loop amplitudes*. JHEP **0803** (2008) 042, arXiv:0711.3596 [hep-ph].

[44] A. van Hameren, *OneLOop: For the evaluation of one-loop scalar functions*. Comput.Phys.Commun. **182** (2011) 2427–2438, arXiv:1007.4716 [hep-ph].

[45] https://www.itp.kit.edu/~vbfnloweb/wiki/doku.php?id=team.

[46] http://www.hep.phy.cam.ac.uk/theory/webber/Herwig/.

[47] G. Corcella, I. Knowles, G. Marchesini, S. Moretti, K. Odagiri, *et al.*, *HERWIG 6: An Event generator for hadron emission reactions with interfering gluons (including supersymmetric processes)*. JHEP **0101** (2001) 010, arXiv:hep-ph/0011363 [hep-ph].

[48] G. Corcella, I. Knowles, G. Marchesini, S. Moretti, K. Odagiri, *et al.*, *HERWIG 6.5 release note*. arXiv:hep-ph/0210213 [hep-ph].

[49] S. Plätzer and S. Gieseke, *Dipole Showers and Automated NLO Matching in Herwig++*. Eur.Phys.J. **C72** (2012) 2187, arXiv:1109.6256 [hep-ph].

[50] The RIVET Project, http://rivet.hepforge.org/.

[51] J. Campbell, K. Ellis, and C. Williams, http://mcfm.fnal.gov/.

Appendix

A. The Catani-Seymour Algorithm

A.1. Massless Partons

The +-regularized Altarelli-Parisi splitting functions are given by

$$P^{qg}(x) = P^{\bar{q}g}(x) = C_F \frac{1+(1-x)^2}{x} \tag{8.1a}$$

$$P^{gq}(x) = P^{g\bar{q}}(x) = T_R\left[x^2+(1-x)^2\right] \tag{8.1b}$$

$$P^{qq}(x) = P^{\bar{q}\bar{q}}(x) = C_F\left(\frac{1+x^2}{1-x}\right)_+ \tag{8.1c}$$

$$\begin{aligned} P^{gg}(x) = 2C_A\Bigg[\left(\frac{1}{1-x}\right)_+ + \frac{1-x}{x} - 1 + x(1-x)\Bigg] \\ + \delta(1-x)\left(\frac{11}{6}C_A - \frac{2}{3}N_f T_R\right) \end{aligned} \tag{8.1d}$$

When written explicitly for all possible parton combinations the functions $\overline{K}^{ab}(x)$ that appear in the $\boldsymbol{K}$-operator read

$$\overline{K}^{qg}(x) = \overline{K}^{\bar{q}g}(x) = P^{qg}(x)\ln\frac{1-x}{x} + C_F x \tag{8.2a}$$

$$\overline{K}^{gq}(x) = \overline{K}^{g\bar{q}}(x) = P^{gq}(x)\ln\frac{1-x}{x} + T_R 2x(1-x) \tag{8.2b}$$

$$\begin{aligned} \overline{K}^{qq}(x) = \overline{K}^{\bar{q}\bar{q}}(x) = C_F\Bigg[\left(\frac{2}{1-x}\ln\frac{1-x}{x}\right)_+ - (1+x)\ln\frac{1-x}{x} + (1-x) \\ - \delta(1-x)(5-\pi^2)\Bigg] \end{aligned} \tag{8.2c}$$

$$\begin{aligned} \overline{K}^{gg}(x) = 2C_A\Bigg[\left(\frac{1}{1-x}\ln\frac{1-x}{x}\right)_+ + \left(\frac{1-x}{x} - 1 + x(1-x)\right)\ln\frac{1-x}{x}\Bigg] \\ - \delta(1-x)\left[\left(\frac{50}{9} - \pi^2\right)C_A - \frac{16}{9}T_R N_f\right] \end{aligned} \tag{8.2d}$$

$$\overline{K}^{q\bar{q}}(x) = \overline{K}^{\bar{q}q}(x) = 0 \tag{8.2e}$$

and

$$\tilde{K}^{aa'}(x) \;=\; P^{aa'}_{\mathrm{reg}}(x)\ln(1-x) + \delta^{aa'}\boldsymbol{T}^2_{a'}\left[\left(\frac{2}{1-x}\ln(1-x)\right)_+ - \frac{\pi^2}{3}\delta(1-x)\right] \tag{8.3}$$

where $P^{aa'}_{\rm reg}(x)$ denotes the regularized Altarelli-Parisi splitting functions

$$\begin{aligned} P^{ab}_{\rm reg}(x) &= P^{ab}(x) \qquad \text{for } a \neq b && (8.4)\\ P^{qq}_{\rm reg}(x) &= -C_F(1+x) && (8.5)\\ P^{gg}_{\rm reg}(x) &= 2C_A\left[\frac{1-x}{x} - 1 + x(1-x)\right] && (8.6) \end{aligned}$$

As denoted by the subscript F.S. the functions $K^{ab}_{\rm F.S.}(x)$ depend on the factorization scheme used for the parton distributions. In the commonly used $\overline{\rm MS}$-scheme they vanish

$$K^{ab}_{\overline{\rm MS}}(x) = 0 \tag{8.7}$$

while in the DIS-scheme they are given by

$$\begin{aligned} K^{qq}_{\rm DIS}(x) = K^{\bar{q}\bar{q}}_{\rm DIS}(x) &= C_F\left[\frac{1+x^2}{1-x}\left(\ln\frac{1-x}{x} - \frac{3}{4}\right) + \frac{1}{4}(9+5x)\right]_+ && (8.8)\\ &= -K^{qg}_{\rm DIS}(x) = -K^{\bar{q}g}_{\rm DIS}(x)\\ K^{gq}_{\rm DIS}(x) = K^{g\bar{q}}_{\rm DIS}(x) &= T_R\left[\left(x^2+(1-x)^2\right)\ln\frac{1-x}{x} + 8x(1-x) - 1\right] && (8.9)\\ K^{gg}_{\rm DIS}(x) &= -2N_f K^{gq}_{\rm DIS}(x) && (8.10)\\ K^{q\bar{q}}_{\rm DIS}(x) = K^{\bar{q}q}_{\rm DIS}(x) &= 0 && (8.11) \end{aligned}$$

The spin-averaged unregularized Altarelli-Parisi splitting functions in d dimensions are given by the expressions [2, eqs. (4.18)-(4.21)]

$$< \hat{P}_{qq}(z,\epsilon) > = C_F\left[\frac{1+z^2}{1-z} - \epsilon(1-z)\right] \tag{8.12a}$$

$$< \hat{P}_{qg}(z,\epsilon) > = C_F\left[\frac{1+(1-z)^2}{z} - \epsilon z\right] \tag{8.12b}$$

$$< \hat{P}_{gq}(z,\epsilon) > = T_R\left[1 - \frac{2z(1-z)}{1-\epsilon}\right] \tag{8.12c}$$

$$< \hat{P}_{gg}(z,\epsilon) > = 2C_A\left[\frac{z}{1-z} + \frac{1-z}{z} - z(1-z)\right] \tag{8.12d}$$

and the $\hat{P}'_{ab}$ are defined as in equation (8.43) of [2]:

$$< \hat{P}_{ab}(x,\epsilon) >=< \hat{P}_{ab}(x,\epsilon=0) > -\epsilon\hat{P}'_{ab}(x) + \mathcal{O}(\epsilon^2)\ . \tag{8.13}$$

A.2. Massive Partons

The non-singular part $\mathcal{V}_j^{(\mathrm{NS})}(s_{jk}, m_j, m_k, \{m_F\}, \kappa)$ is given by

$$\begin{aligned}
\mathcal{V}_q^{(\mathrm{NS})}(s_{jk}, m_j, m_k, \{m_F\}, \kappa) &= \frac{\gamma_q}{\boldsymbol{T}_q^2} \ln \frac{s_{jk}}{Q_{jk}^2} \\
&+ \frac{1}{v_{jk}} \left[\ln \rho^2 \ln(1+\rho^2) + 2\,\mathrm{Li}_2(\rho^2) - \mathrm{Li}_2(1-\rho_j^2) - \mathrm{Li}_2(1-\rho_k^2) - \frac{\pi^2}{6} \right] \\
&+ \ln \frac{Q_{jk}-m_k}{Q_{jk}} - 2 \ln \frac{(Q_{jk}-m_k)^2 - m_j^2}{Q_{jk}^2} - \frac{2m_j^2}{s_{jk}} \ln \frac{m_j}{Q_{jk}-m_k} \\
&- \frac{m_k}{Q_{jk}-m_k} + \frac{2m_k(2m_k - Q_{jk})}{s_{jk}} + \frac{\pi^2}{2} \qquad (8.14)
\end{aligned}$$

$$\begin{aligned}
&\mathcal{V}_q^{(\mathrm{NS})}(s_{jk}, m_j, m_k = 0, \{m_F\}, \kappa) \\
&\quad = \frac{\gamma_q}{\boldsymbol{T}_q^2} \ln \frac{s_{jk}}{Q_{jk}^2} + \frac{\pi^2}{6} - \mathrm{Li}_2\left(\frac{s_{jk}}{Q_{jk}^2}\right) - 2 \ln \frac{s_{jk}}{Q_{jk}^2} - \frac{m_j^2}{s_{jk}} \ln \frac{m_j^2}{Q_{jk}^2} \qquad (8.15)
\end{aligned}$$

$$\begin{aligned}
&\mathcal{V}_q^{(\mathrm{NS})}(s_{jk}, m_j = 0, m_k, \{m_F\}, \kappa) \qquad (8.16) \\
&\quad = \frac{\gamma_q}{\boldsymbol{T}_q^2} \left[\ln \frac{s_{jk}}{Q_{jk}^2} - 2 \ln \frac{Q_{jk}-m_k}{Q_{jk}} - \frac{2m_k}{Q_{jk}+m_k} \right] + \frac{\pi^2}{6} - \mathrm{Li}_2\left(\frac{s_{jk}}{Q_{jk}^2}\right)
\end{aligned}$$

$$\mathcal{V}_q^{(\mathrm{NS})}(s_{jk}, m_j = 0, m_k = 0, \{m_F\}, \kappa) = 0 \qquad (8.17)$$

$$\begin{aligned}
&\mathcal{V}_g^{(\mathrm{NS})}(s_{jk}, m_j = 0, m_k, \{m_F\}, \kappa) = \qquad (8.18) \\
&\quad = \frac{\gamma_g}{\boldsymbol{T}_g^2} \left[\ln \frac{s_{jk}}{Q_{jk}^2} - 2 \ln \frac{Q_{jk}-m_k}{Q_{jk}} - \frac{2m_k}{Q_{jk}+m_k} \right] + \frac{\pi^2}{6} - \mathrm{Li}_2\left(\frac{s_{jk}}{Q_{jk}^2}\right) \\
&\quad + \frac{4}{3}\frac{T_R}{C_A} \sum_{F=1}^{N_F^{jk}} \left[\ln \frac{Q_{jk}-m_k}{Q_{jk}} + \frac{m_k \rho_1^3}{Q_{jk}+m_k} + \ln \frac{1+\rho_1}{2} - \frac{\rho_1}{3}(3+\rho_1^2) - \frac{1}{2} \ln \frac{m_F^2}{Q_{jk}^2} \right] \\
&\quad + \frac{2}{3}\frac{T_R}{C_A} \sum_{F=1}^{N_F} \ln \frac{m_F^2}{Q_{\mathrm{aux}}^2} + \left(\kappa - \frac{2}{3}\right) \frac{m_k^2}{s_{jk}} \Bigg[\left(2\frac{T_R}{C_A} N_f - 1\right) \ln \frac{2m_k}{Q_{jk}+m_k} \\
&\qquad\qquad + 2\frac{T_R}{C_A} \sum_{F=1}^{N_F^{jk}} \left(\rho_2^3 \ln\left(\frac{\rho_2-\rho_1}{\rho_2+\rho_1}\right) - \ln\left(\frac{1-\rho_1}{1+\rho_1}\right) - \frac{8\rho_1 m_F^2}{s_{jk}} \right) \Bigg]
\end{aligned}$$

$$\begin{aligned}
&\mathcal{V}_g^{(\mathrm{NS})}(s_{jk}, m_j = 0, m_k = 0, \{m_F\}, \kappa) = \qquad (8.19) \\
&\quad = \frac{4}{3}\frac{T_R}{C_A} \sum_{F=1}^{N_F^{jk}} \left[\ln \frac{1+\rho_1}{2} - \frac{\rho_1}{3}(3+\rho_1^2) - \frac{1}{2} \ln \frac{m_F^2}{s_{jk}} \right] + \frac{2}{3}\frac{T_R}{C_A} \sum_{F=1}^{N_F} \ln \frac{m_F^2}{Q_{\mathrm{aux}}^2}
\end{aligned}$$

where N_F is the number of heavy flavors and N_F^{jk} the number of those heavy flavors for which $s_{jk} > 4m_F(m_F + m_k)$. ρ_1 and ρ_2 are given by

$$\rho_1 = \sqrt{1 - \frac{4m_F^2}{(Q_{jk}-m_k)^2}} \qquad \text{and} \qquad \rho_2 = \sqrt{1 - \frac{4m_F^2}{Q_{jk}^2 - m_k^2}} \qquad (8.20)$$

The functions $\mathcal{K}_j^{a,a'}$ are defined as

$$\mathcal{K}_q^{g,q}(x, s_{ja}, m_j) = 0 \tag{8.21}$$

$$\begin{aligned}\mathcal{K}_q^{q,q}(x, s_{ja}, m_j) &= 2\left[\left(\frac{\ln(1-x)}{1-x}\right)_+ - \frac{\ln(2-x)}{1-x}\right] + \left[J_{gQ}^a\left(x, \frac{m_j}{\sqrt{s_{ja}}}\right)\right]_+ \\ &+ 2\left(\frac{1}{1-x}\right)_+ \ln\frac{(2-x)s_{ja}}{(2-x)s_{ja}+m_j^2} - \frac{\gamma_q}{C_F}\delta(1-x) \\ &+ \delta(1-x)\left(\frac{m_j^2}{s_{ja}}\ln\frac{m_j^2}{s_{ja}+m_j^2} + \frac{1}{2}\frac{m_j^2}{s_{ja}+m_j^2}\right)\end{aligned} \tag{8.22}$$

$$\mathcal{K}_q^{q,g}(x, s_{ja}, m_j) = 2\frac{C_F}{C_A}\frac{m_j^2}{x s_{ja}}\ln\frac{m_j^2}{(1-x)s_{ja}+m_j^2} \tag{8.23}$$

$$\mathcal{K}_q^{g,g}(x, s_{ja}, m_j) = \mathcal{K}_q^{q,q}(x, s_{ja}, m_j) + \frac{C_A}{C_F}\mathcal{K}_q^{q,g}(x, s_{ja}, m_j) \tag{8.24}$$

$$\begin{aligned}\mathcal{K}_g^{a,a'}(x, s_{ja}, 0, \{m_F\}) &= -\delta^{aa'}\frac{\gamma_g}{C_A}\left[\left(\frac{1}{1-x}\right)_+ + \delta(1-x)\right] \\ &+ \delta^{aa'}\frac{T_R}{C_A}\sum_{F=1}^{N_F^{ja}}\left\{\left(\delta(1-x) - \delta(x_+ - x)\right)\left[\frac{2}{3}\left(\ln\frac{m_F^2}{s_{ja}} + \frac{5}{3}\right)\right.\right. \\ &- \left.\left. J_{Q\bar{Q}}^{a,\mathrm{NS}}\left(\frac{m_F}{\sqrt{s_{ja}}}\right)\right] + \left[J_{Q\bar{Q}}^a\left(x, \frac{m_F}{\sqrt{s_{ja}}}\right)\right]_{x_+} \\ &+ \delta(1-x)\frac{2}{3}\left(1 - \frac{4m_F^2}{s_{ja}}\right)^{3/2}\right\}\end{aligned} \tag{8.25}$$

where $x_+ = 1 - 4m_F^2/s_{ja}$ and N_F^{ja} is the number of flavors with $s_{ja} > 4m_F^2$.

B. Monte Carlo Uncertainty

As stated in equation (4.6) of section 4.1 the variance of the estimator of the Monte Carlo integral is given by

$$\mathrm{Var}[\sigma] = \frac{V^2}{N}\,\mathrm{Var}[g]\ . \tag{8.26}$$

Furthermore, it was stated that the variance of the function g can be estimated as

$$\delta_g^2 = \frac{1}{N-1}\sum_{i=1}^{N}(g_i - \bar{g})^2 \qquad \text{with} \qquad \bar{g} = \frac{1}{N}\sum_{i=1}^{N} g_i\ . \tag{8.27}$$

The reason for this is that when computing both the mean and the standard deviation of a data sample consisting of N data points the underlying 'true' expectation value $E[g] =: \mu_g$ is unknown.

$$\begin{aligned}E\left[\delta_g^2\right] &= E\left[\frac{1}{N-1}\sum_{i=1}^{N}(g_i - \bar{g})^2\right] = E\left[\frac{1}{N-1}\sum_{i=1}^{N}\left((g_i - \mu_g) - (\bar{g} - \mu_g)\right)^2\right] \\ &= E\left[\frac{1}{N-1}\sum_{i=1}^{N}(g_i - \mu_g)^2 - \frac{2}{N-1}(\bar{g} - \mu_g)\sum_{i=1}^{N}(g_i - \mu_g) + \frac{1}{N-1}\sum_{i=1}^{N}(\bar{g} - \mu_g)^2\right]\end{aligned} \tag{8.28}$$

Since

$$\sum_{i=1}^{N} (g_i - \mu_g) = N\bar{g} - N\mu_g \tag{8.29}$$

one obtains

$$\begin{aligned} E\left[\delta_g^2\right] &= E\left[\frac{1}{N-1}\sum_{i=1}^{N}(g_i-\bar{g})^2\right] = E\left[\frac{1}{N-1}\sum_{i=1}^{N}(g_i-\mu_g)^2 - \frac{N}{N-1}(\bar{g}-\mu_g)^2\right] \\ &= \frac{N}{N-1}\underbrace{E\left[\frac{1}{N}\sum_{i=1}^{N}(g_i-\mu_g)^2\right]}_{=\mathrm{Var}[g]} - \frac{N}{N-1}E\left[(\bar{g}-\mu_g)^2\right] \ . \end{aligned} \tag{8.30}$$

The second term gives

$$\begin{aligned} E\left[(\bar{g}-\mu_g)^2\right] &= E\left[\left(\frac{1}{N}\sum_{i=1}^{N} g_i - \mu_g\right)\left(\frac{1}{N}\sum_{j=1}^{N} g_j - \mu_g\right)\right] \\ &= E\left[\frac{1}{N^2}\sum_{i,j=1}^{N}(g_i-\mu_g)(g_j-\mu_g)\right] = \frac{1}{N^2}\sum_{i,j=1}^{N} E\left[(g_i-\mu_g)(g_j-\mu_g)\right] \\ &= \frac{1}{N^2}\sum_{i,j=1}^{N}\mathrm{Cov}[g_i,g_j] \end{aligned} \tag{8.31}$$

With $\mathrm{Cov}[g_i, g_i] = \mathrm{Var}[g_i] = \mathrm{Var}[g]$ and since the random numbers are uncorrelated and thus $\mathrm{Cov}[g_i, g_j] = 0$ for $i \neq j$

$$\frac{1}{N^2}\sum_{i,j=1}^{N}\mathrm{Cov}[g_i,g_j] = \frac{1}{N^2}N\,\mathrm{Var}[g] = \frac{1}{N}\mathrm{Var}[g] \ . \tag{8.32}$$

Thus, one obtains

$$\begin{aligned} E\left[\delta_g^2\right] &= \frac{N}{N-1}\mathrm{Var}[g] - \frac{N}{N-1}\cdot\frac{1}{N}\mathrm{Var}[g] \\ &= \left(\frac{N}{N-1} - \frac{1}{N-1}\right)\mathrm{Var}[g] = \mathrm{Var}[g] \end{aligned} \tag{8.33}$$

which demonstrates that the estimator of the standard deviation is unbiased.

The expression for the Monte Carlo uncertainty which is suited for continuous calculation during the integration is then given by

$$\delta = \frac{V}{\sqrt{N(N-1)}}\sqrt{\sum_{i=1}^{N}(g_i-\bar{g})^2} = \frac{V}{\sqrt{N(N-1)}}\sqrt{\sum_{i=1}^{N} g_i^2 - \frac{1}{N}\left(\sum_{i=1}^{N} g_i\right)^2} \ . \tag{8.34}$$

C. Derivation of the Combination Formulas

C.1. Combination of the Uncertainty of Total Cross Sections

Just as for the combination of total cross sections one can derive the expression for the combined statistical uncertainty. As stated in equation (4.8) the uncertainty of each run is given by

$$\delta^{(j)} = \frac{V}{\sqrt{N^{(j)}(N^{(j)}-1)}} \sqrt{\sum_{i_j=1}^{N_j} g_{i_j}^2 - \frac{1}{N^{(j)}} \left(\sum_{i_j=1}^{N^{(j)}} g_{i_j} \right)^2} \tag{8.35}$$

while the combined uncertainty is of the form

$$\delta = \frac{V}{\sqrt{N(N-1)}} \sqrt{\sum_{i=1}^{N} g_i^2 - \frac{1}{N} \left(\sum_{i=1}^{N} g_i \right)^2} \,. \tag{8.36}$$

By using

$$\frac{N^{(j)}(N^{(j)}-1){\delta^{(j)}}^2}{V^2} + \frac{1}{N^{(j)}} \left(\sum_{i_j=1}^{N^{(j)}} g_{i_j} \right)^2 = \sum_{i_j=1}^{N^{(j)}} g_{i_j}^2 \tag{8.37}$$

the combined uncertainty can be rewritten as

$$\begin{aligned} \frac{N(N-1)\delta^2}{V^2} &= \sum_{j=1}^{M} \sum_{i_j=1}^{N^{(j)}} g_{i_j}^2 - \frac{1}{N} \left(\sum_{j=1}^{M} \sum_{i_j=1}^{N^{(j)}} g_{i_j} \right)^2 \\ &= \sum_{j=1}^{M} \left[\frac{N^{(j)}(N^{(j)}-1){\delta^{(j)}}^2}{V^2} + \frac{1}{N^{(j)}} \left(\sum_{i_j=1}^{N^{(j)}} g_{i_j} \right)^2 \right] - \frac{1}{N} \left(\sum_{j=1}^{M} \sum_{i_j=1}^{N^{(j)}} g_{i_j} \right)^2 \\ &= \sum_{j=1}^{M} \left[\frac{N^{(j)}(N^{(j)}-1){\delta^{(j)}}^2}{V^2} + \frac{1}{N^{(j)}} \left(\frac{\sigma^{(j)} N^{(j)}}{V} \right)^2 \right] - \frac{1}{N} \left(\sum_{j=1}^{M} \frac{\sigma^{(j)} N^{(j)}}{V} \right)^2 . \end{aligned} \tag{8.38}$$

From this one obtains

$$\delta^2 = \frac{1}{N(N-1)} \left[\sum_{j=1}^{M} \left(N^{(j)} {\sigma^{(j)}}^2 + N^{(j)}(N^{(j)}-1){\delta^{(j)}}^2 \right) - \frac{1}{N} \left(\sum_{j=1}^{M} N^{(j)} \sigma^{(j)} \right)^2 \right] \tag{8.39}$$

and thus

$$\delta = \frac{1}{\sqrt{N(N-1)}} \sqrt{\sum_{j=1}^{M} \left(N^{(j)} {\sigma^{(j)}}^2 + N^{(j)}(N^{(j)}-1){\delta^{(j)}}^2 \right) - \frac{1}{N} \left(\sum_{j=1}^{M} N^{(j)} \sigma^{(j)} \right)^2} \tag{8.40}$$

as given in equation (4.27).

C.2. Combination of Histograms

Applying the formulas from section 4.2 to M parallel runs indexed by j the differential cross section and its error for each of the parallel runs are given by

$$\sigma_x^{(j)}(x_b) = \frac{d\sigma^{(j)}}{dx}(x_b) = \frac{V}{\Delta X} \frac{1}{N^{(j)}} G_{1,b}^{(j)} \tag{8.41a}$$

$$\delta_x^{(j)}(x_b) = \frac{V}{\Delta X \sqrt{N^{(j)}(N^{(j)}-1)}} \sqrt{G_{2,b}^{(j)} - \frac{1}{N^{(j)}} {G_{1,b}^{(j)}}^2} \tag{8.41b}$$

where $G_{1,b}^{(j)}$ and $G_{2,b}^{(j)}$ are the summed weights and squared weights in bin b for run j. From these expression one gets

$$G_{1,b}^{(j)} = \frac{N^{(j)}\Delta X}{V}\sigma_x^{(j)}(x_b) \tag{8.42a}$$

$$G_{2,b}^{(j)} = N^{(j)}(N^{(j)}-1)\left(\frac{\Delta X \delta_x^{(j)}(x_b)}{V}\right)^2 + \frac{1}{N^{(j)}}{G_{1,b}^{(j)}}^2 . \tag{8.42b}$$

With this the combined differential cross section can be calculated as

$$\begin{aligned}\sigma_x(x_b) &= \frac{V}{N\Delta X}G_{1,b} = \frac{V}{N\Delta X}\sum_{j=1}^{M} G_{1,b}^{(j)} \\ &= \frac{V}{N\Delta X}\sum_{j=1}^{M}\frac{N^{(j)}\Delta X}{V}\sigma_x^{(j)}(x_b) = \frac{1}{N}\sum_{j=1}^{M} N^{(j)}\sigma_x^{(j)}(x_b)\end{aligned} \tag{8.43}$$

and its error as

$$\begin{aligned}\delta_x(x_b) &= \frac{V}{\Delta X N(N-1)}\sqrt{G_{2,b} - \frac{1}{N}G_{1,b}^2} \\ &= \frac{V}{\Delta X N(N-1)}\sqrt{\sum_{j=1}^{M} G_{2,b}^{(j)} - \frac{1}{N}\left(\sum_{j=1}^{M} G_{1,b}^{(j)}\right)^2} \\ &= \frac{V}{\Delta X N(N-1)} \\ &\quad\times\sqrt{\sum_{j=1}^{M}\left[N^{(j)}(N^{(j)}-1)\left(\frac{\Delta X\delta_x^{(j)}(x_b)}{V}\right)^2 + \frac{1}{N^{(j)}}{G_{1,b}^{(j)}}^2\right] - \frac{1}{N}\left(\sum_{j=1}^{M} G_{1,b}^{(j)}\right)^2} \\ &= \frac{V}{\Delta X N(N-1)} \\ &\quad\times\left\{\sum_{j=1}^{M}\left[N^{(j)}(N^{(j)}-1)\left(\frac{\Delta X\delta_x^{(j)}(x_b)}{V}\right)^2 + \frac{1}{N^{(j)}}\left(\frac{N^{(j)}\Delta X}{V}\sigma_x^{(j)}(x_b)\right)^2\right]\right. \\ &\qquad\left. - \frac{1}{N}\left(\sum_{j=1}^{M}\frac{N^{(j)}\Delta X}{V}\sigma_x^{(j)}(x_b)\right)^2\right\}^{1/2} \\ &= \frac{1}{N(N-1)} \\ &\quad\times\sqrt{\sum_{j=1}^{M}\left[N^{(j)}(N^{(j)}-1){\delta_x^{(j)}}^2(x_b) + N^{(j)}{\sigma_x^{(j)}}^2(x_b)\right] - \frac{1}{N}\left(\sum_{j=1}^{M} N^{(j)}\sigma_x^{(j)}(x_b)\right)^2} .\end{aligned} \tag{8.44}$$

Thus, the combination of histograms can be expressed in the same way as in the case of the total cross sections:

$$\sigma_x(x_b) = \frac{1}{N}\sum_{j=1}^{M} N^{(j)}\sigma_x^{(j)}(x_b) \tag{8.45}$$

and

$$\delta_x(x_b) = \frac{1}{N(N-1)} \times \sqrt{\sum_{j=1}^{M}\left[N^{(j)}{\sigma_x^{(j)}}^2(x_b) + N^{(j)}(N^{(j)}-1){\delta_x^{(j)}}^2(x_b)\right] - \frac{1}{N}\left(\sum_{j=1}^{M} N^{(j)}\sigma_x^{(j)}(x_b)\right)^2}\,. \tag{8.46}$$

D. Fixed-Order Comparison

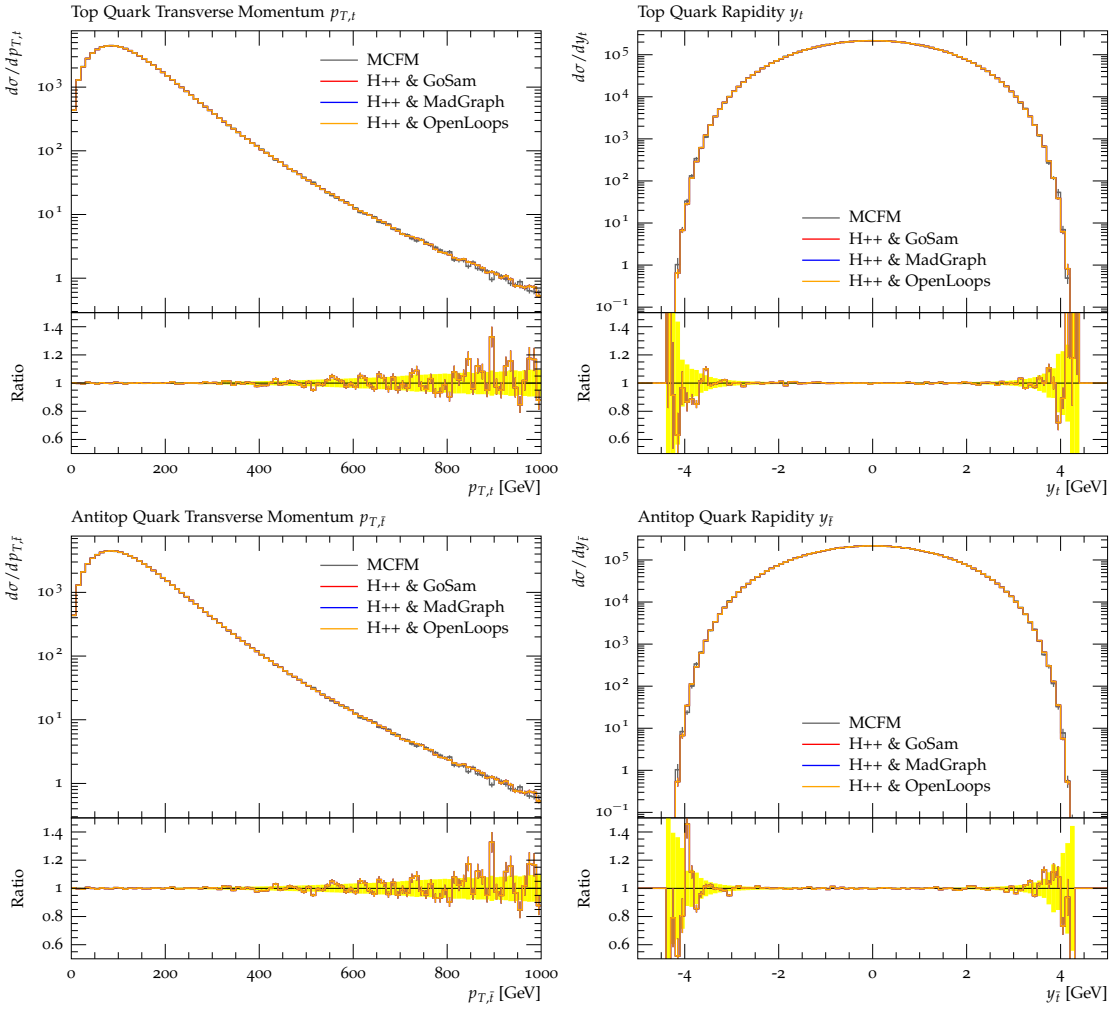

Figure D.1.: Fixed-order comparison of the transverse momentum and rapidity distributions of the top and the antitop quark for the process $pp \to t\bar{t}$ at LO for a center-of-mass energy of 14 TeV. The yellow error bands denote the statistical uncertainty for the results of MCFM.

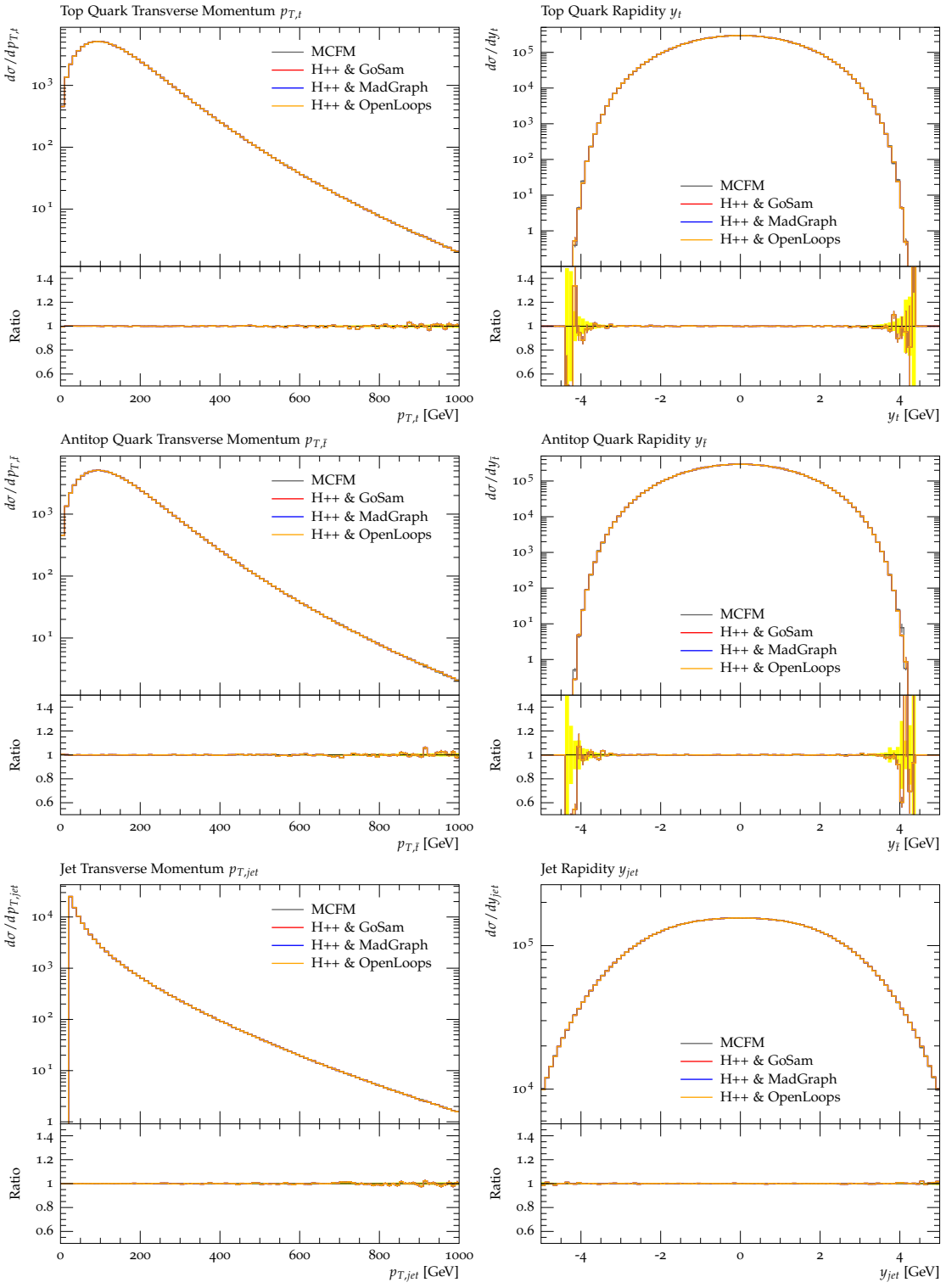

Figure D.2.: Fixed-order comparison of the transverse momentum and rapidity distributions of the top quark, the anti-top quark and the jet parton for the process $pp \to t\bar{t}j$ at LO for a center-of-mass energy of 14 TeV. The yellow error bands denote the statistical uncertainty for the results of MCFM.

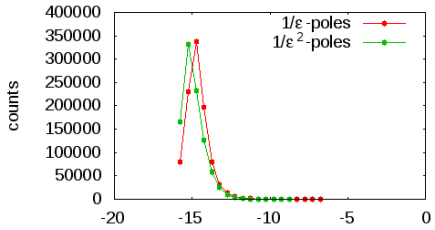

(a) pole cancellation in $gg \to t\bar{t}$

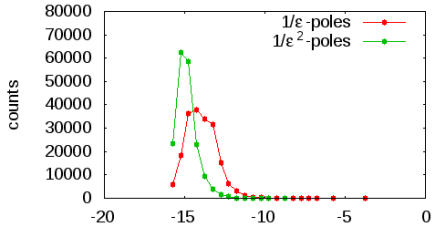

(b) pole cancellation in $u\bar{u} \to t\bar{t}$

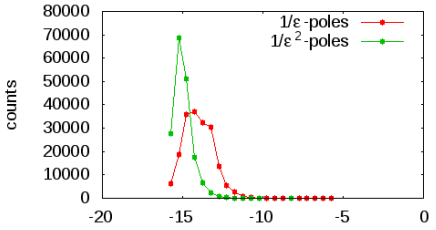

(c) pole cancellation in $\bar{u}u \to t\bar{t}$

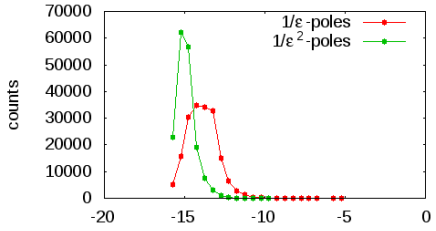

(d) pole cancellation in $d\bar{d} \to t\bar{t}$

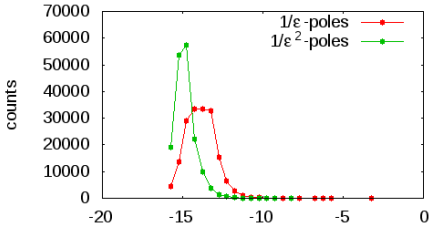

(e) pole cancellation in $\bar{d}d \to t\bar{t}$

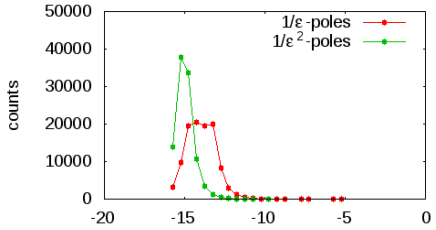

(f) pole cancellation in $s\bar{s} \to t\bar{t}$

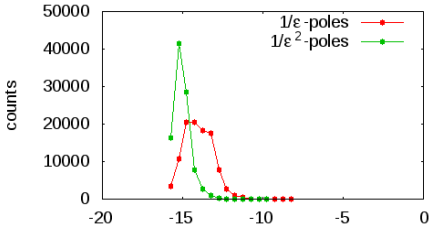

(g) pole cancellation in $\bar{s}s \to t\bar{t}$

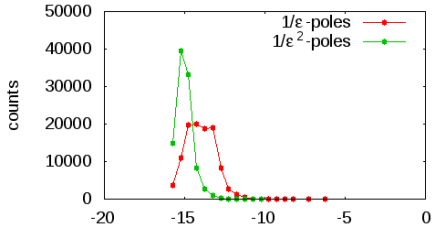

(h) pole cancellation in $c\bar{c} \to t\bar{t}$

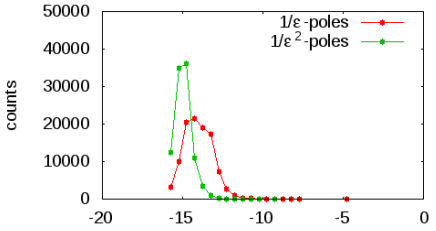

(i) pole cancellation in $\bar{c}c \to t\bar{t}$

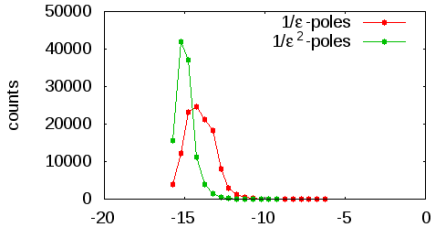

(j) pole cancellation in $b\bar{b} \to t\bar{t}$

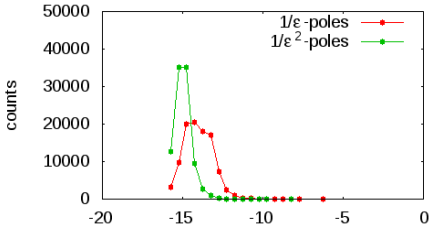

(k) pole cancellation in $\bar{b}b \to t\bar{t}$

Figure D.3.: Pole cancellation plots for the process $pp \to t\bar{t}$. The abscissas are not labeled for spacing reasons but show the number of canceled decimal places just like the plots in figure 7.9.

List of Figures